UNIVERSITY OF OKLAHOMA

GRADUATE COLLEGE

TOWARD A MORE CLARIFIED DETECTIVE QUANTUM EFFICIENCY METHODOLOGY: STUDY OF THE DQE THEORY AND APPLICATIONS

A DISSERTATION

SUBMITTED TO THE GRADUATE FACULTY

in partial fulfillment of the requirements for the

Degree of

DOCTOR OF PHILOSOPHY

By

DA ZHANG

Norman, Oklahoma

2009

TOWARD A MORE CLARIFIED DETECTIVE QUANTUM EFFICIENCY METHODOLOGY: STUDY OF THE DQE THEORY AND APPLICATIONS

A DISSERTATION APPROVED FOR THE
SCHOOL OF ELECTRICAL AND COMPUTER ENGINEERING

BY

Dr. Hong Liu, Chair

Dr. Susan Edwards

Dr. Patrick McCann

Dr. Edgar A. O'Rear III

Dr. Zhisheng Shi

This dissertation is dedicated to my grandparents, my parents and my fiancee Kelsey, whose never-ending love, encouragement, and support have provided me the confidence to pursue my dreams. Words cannot express my gratitude for being blessed with such a wonderful family.

Acknowledgements

I am incredibly grateful for the opportunity to work under the guidance of Dr. Hong Liu. It has been a fantastic learning experience to conduct research in this innovative and knowledge-rich environment, and in this leading research team in diagnostic x-ray imaging. Without Dr. Liu's guidance, advice, and support, my work would have been unachievable. Dr. Liu has been an amazing teacher, a great mentor, and a selfless supporter for my academic and professional development. I will be forever thankful to him for providing me with this excellent and incomparable opportunity.

I would also like to thank the other members of our research team for their help and encouragement: Dr. Yuhua Li, Dr. Fanbo Meng, Molly Wong, Xingwei Wang, Qiong Wang, Qirong Zhang, Yongshen Ni, Yiyang Zhou, Yuchen Qiu, Ben Steel and Mark Wood. Their exceptional dedication to Dr. Liu, to their research, and to other members of the team is admirable and inspiring. In addition, I am deeply grateful to Molly Wong for the smooth and pleasant teamwork, and for helping me tirelessly with my English writing.

Finally, I would like to express my gratitude to the other members of my committee, Dr. Susan Edwards, Dr. Patrick McCann, Dr. Edgar A. O'Rear III, and Dr. Zhisheng Shi for their unbelievable help, advice, and encouragement.

Contents

List of Tables

List of Figures

Abstract

Detective quantum efficiency (DQE) is widely accepted as the golden rule to objectively evaluate the performance of x-ray imaging systems. It provides a comprehensive characterization of an x-ray imaging system, because it combines several important image-quality-related measurements such as contrast, resolution, and noise, and because it measures the efficiency of the utilization of x-ray in the imaging process. Despite its importance, the current DQE methodology is imperfect in general agreement. The focus of this dissertation is to investigate the DQE methodology for digital x-ray imaging systems, in an effort to clarify some confusing aspects of the current DQE methodology. Through a detailed theoretical derivation of the DQE methodology for digital x-ray imaging, a more clarified understanding of the DQE theory is provided. Besides the re-visited DQE theory, techniques to determine the constituent parts of DQE, including the photon fluence, Modulation Transfer Function (MTF), and Noise Power Spectrum (NPS) are also discussed in this dissertation.

The dissertation is structured as follows. After a brief introduction of the current DQE theory in Chapter 1, the DQE theory for digital x-ray imaging systems is revisited in detail in Chapter 2, with experimental results for the demonstration purpose. In Chapter 3, DQE theory for the magnification radiography is provided, and the theory is supported by experimental results. In Chapter 4, the measurements of x-ray photon fluence and spectral composition are discussed in detail, and uncertainty analysis is conducted to investigate the impact of the calibration uncertainty on the two measurements. In Chapter 5, an innovative alignment procedure that was designed to reduce the error in the spectral measurements and imaging experiments is introduced. MTF measurement techniques are covered in Chapter 6, and NPS

measurement techniques are discussed in Chapter 7. As an example application of the DQE methodology, a study about the impact of additive noise on the imaging performance of a CCD based x-ray system is also reported in Chapter 7. In Chapter 8, a DQE analysis on an innovative dual detector x-ray imaging system is detailed, as another example application of DQE. Finally, a summary of this dissertation is provided in Chapter 9.

CHAPTER 1

Introduction

1.1 Background and Significance

The evaluation of an imaging system's performance and characteristics is of significant importance in x-ray imaging. Imaging performance can be evaluated through more subjective methods, such as Contrast Detail Analysis [1–4] and ACR (American College Radiology) mammography quality control process [4, 5], or through more objective approaches. Detective quantum efficiency (DQE) is widely accepted as the "golden rule" for the objective performance evaluation for x-ray based medical imaging systems. DQE measures the efficiency of the utilization of x-ray photons in the imaging process, and combines several important measurements of image quality, including contrast, resolution, and noise. This dissertation focuses on the DQE theory and methods for digital x-ray imaging systems. In order to clarify several confusing aspects of the current DQE methodology, the theory of DQE is re-derived based on digital x-ray imaging. Then several aspects of the DQE measurement, including the measurements of photon fluence, x-ray spectra, modulation transfer function, and noise power spectrum, are discussed in detail. Finally, two DQE measurements, each being an independently published study, were included as example applications of the DQE methodology.

1.1.1 Image quality related concepts

Image quality is a general concept which applies to all kinds of images, including medical images. From the perspective of objective evaluation, there are three principal

components of image quality: contrast, spatial resolution, and noise. Contrast is the difference of pixel values between closely adjacent areas of an image [6, 7]; the spatial resolution and noise will be introduced in the following sections in a more detailed manner.

Spatial resolution, spread functions and Modulation Transfer Function

Spatial resolution, sometimes simply referred as "resolution", describes the ability of an imaging system to precisely depict objects in the spatial dimensions of an image. One conceptual method to understand and determine the spatial resolution of an imaging system is to measure the system's output to an impulse input, such as a single point, or a narrow line, or just a sharp edge on certain direction. How the shape of the impulse input is preserved on the output image can provide a clue of how much blurring is introduced by the imaging system. The image produced from a single point input is called Point Spread Function (PSF); the cross section of the output to a line impulse input is called the Line Spread Function (LSF); and the cross section of the output to an edge input is called the Edge Spread Function (ESF) [6,8]. For example, Fig. 1.1 shows a line impulse input generated by collimating the x-ray beam with a slit camera, and Fig. 1.3 shows an illustration of the output for the line input.

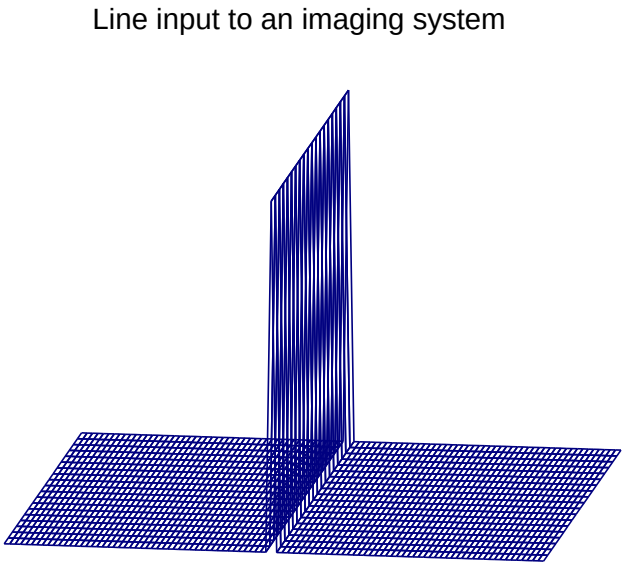

Figure 1.1: Illustration of a narrow line input to an imaging system

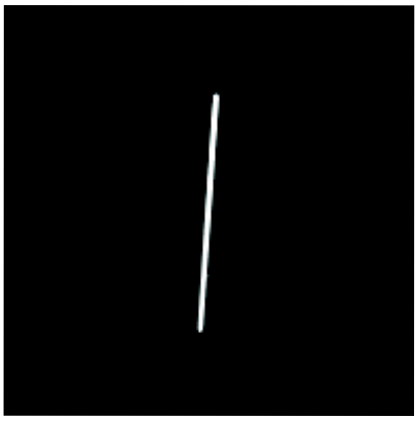

Figure 1.2: Output image of the line input to an imaging system

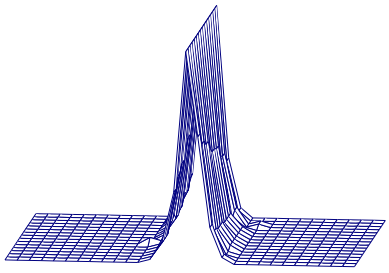

Figure 1.3: 3 dimensional illustration of the output of an imaging system to a narrow slit input

Modulation Transfer Function (MTF) is a relatively comprehensive description of the resolution properties of an imaging system [6], and it measures how much

modulation, which is the change of the amplitude of signals, can be transferred from the input end to the output end of an imaging system [8]. MTF is closely related the aforementioned LSF by the fact that MTF is the normalized modulus of the Fourier Transform of LSF [6, 8, 9]:

$$MTF(f) = \frac{|FT\{LSF(x)\}|}{FT\{LSF(x)\}|_{f=0}}, \tag{1.1}$$

where $FT\{\ \}$ denotes the Fourier Transform, $|\ \ |$ denotes the modulus operator. Fig. 1.4 and 1.5 demonstrated the LSF and MTF acquired from the slit image shown in Fig. 1.2 (data published in [10]).

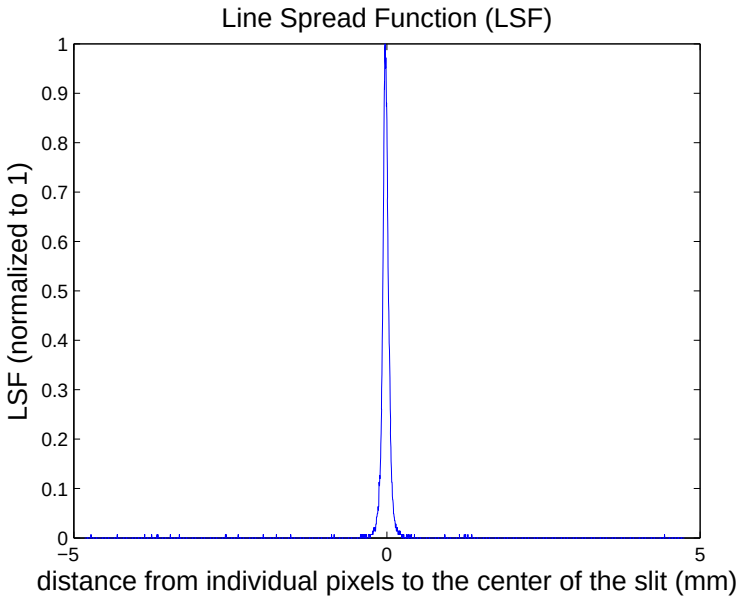

Figure 1.4: Line Spread Function from the slit image

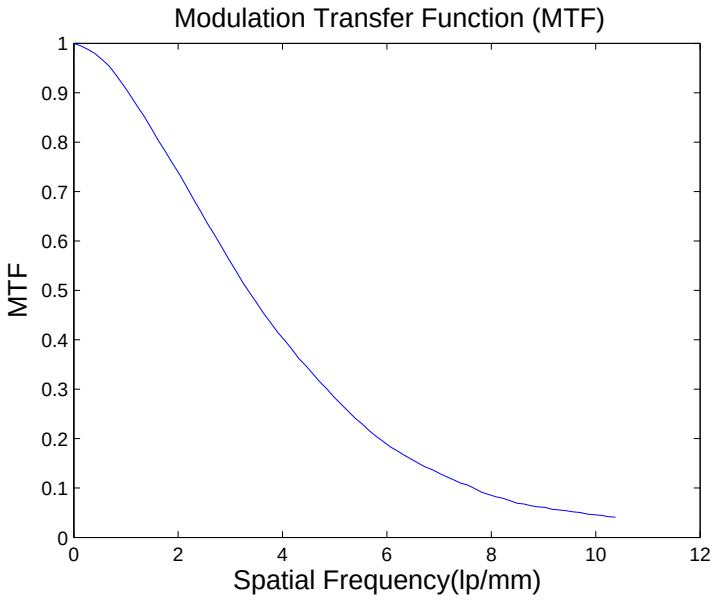

Figure 1.5: Modulation Transfer Function calculated from the LSF in Fig. 1.4

Noise and Noise Power Spectrum

Generally speaking, image noise is something undesirable but present in the images. For example, even if an image is taken with nothing in the beam–therefore a contrast-less and almost uniform image is acquired–the pixel values of the output image are still not exactly uniform, due to the stochastic nature of x-ray radiation and noise introduced by the imaging device. This type of images are used to assess the noise characteristics through, for example, the standard deviation of pixel values about their mean, or through Noise Power Spectrum (NPS) which represents the distribution of the power of noise in the spatial frequency domain [2, 3, 6, 8, 11–23].

The basic idea of Noise Power Spectrum (also called Wiener spectrum or power spectrum density function) is to test the subtle relationship between the noise at one point and the noise at other points, which is not obvious through direct observation. And it describes the power distribution of the noise in the frequency domain [2, 3, 6, 8, 11–23].

NPS is the Fourier Transform of the autocorrelation function of a wide-sense-

stationary (WSS) stochastic process. For a uniformly exposed image $p(x, y)$, the fluctuation of its pixel values ($\Delta p(x, y) = p(x, y) - \overline{p}$) around their mean $\overline{p}$ is typically considered as a 2-dimensional WSS stochastic process [8, 12, 24], and the 2D NPS is defined as the 2D Fourier Transform of the 2D autocorrelation function [8, 21–23, 25, 26]:

$$C(\xi, \eta) = E\{\Delta p(x, y)\Delta p(x + \xi, y + \eta)\}, \tag{1.2}$$

$$NPS(u, v) = F_{2D}\{C(\xi, \eta)\}, \tag{1.3}$$

where F_{2D} denotes the 2D Fourier Transform, $C(\xi, \eta)$ is the autocorrelation function and $E\{\ \}$ denotes the operation of ensemble averaging.

If the noise pattern of the images is isotropic, then 1D NPS could fully represent the noise characteristics, and it could be obtained by circularly averaging the 2D NPS [10–12, 27]:

$$NPS(f) = \frac{1}{N_f}\left(\sum_{f \le \sqrt{u^2+v^2} < f+\Delta f} NPS(u, v)\right), \tag{1.4}$$

where $NPS(u, v)$ and $NPS(f)$ are the 2D NPS and 1D NPS, respectively. N_f is the number of data points in $NPS(u, v)$ within the interval $f \le \sqrt{u^2 + v^2} < f + \Delta f$.

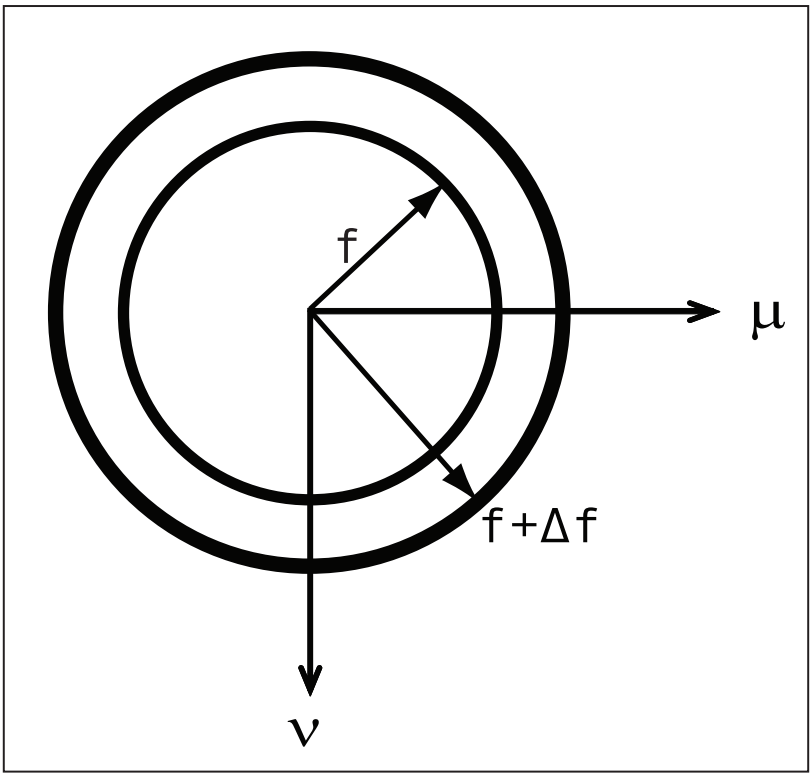

Figure 1.6: Illustration of the circular averaging algorithm used to obtain 1D NPS from 2D NPS

Fig. 1.7 and 1.8 demonstrated the 2D NPS and the corresponding 1D NPS (data published in [11]).

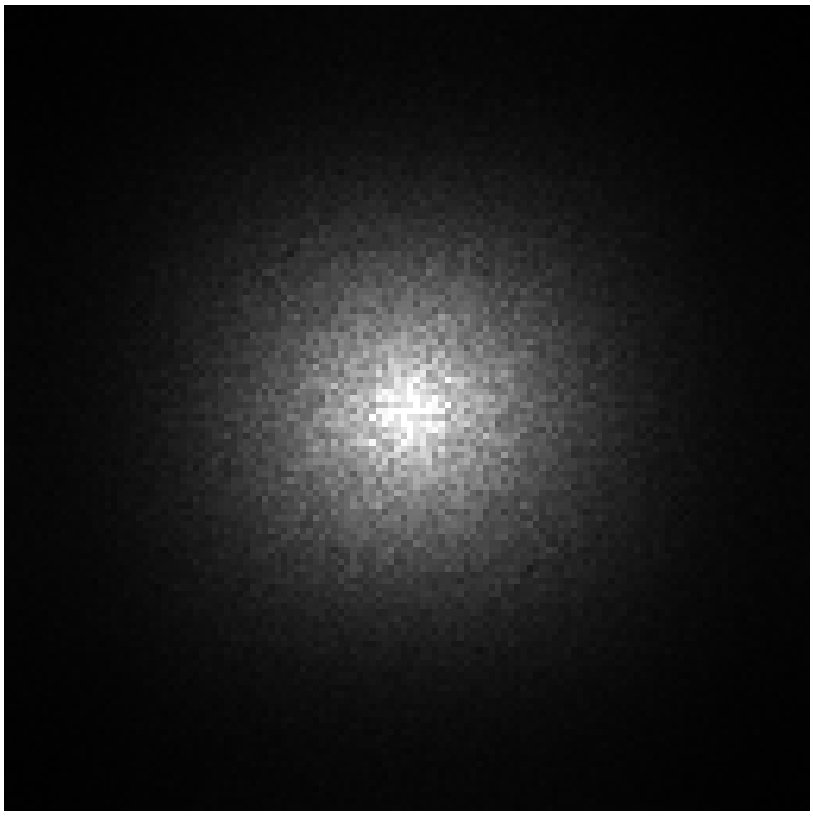

Figure 1.7: 2D NPS obtained with a CCD based x-ray imaging system at 26KV, 0.3mA, 6s

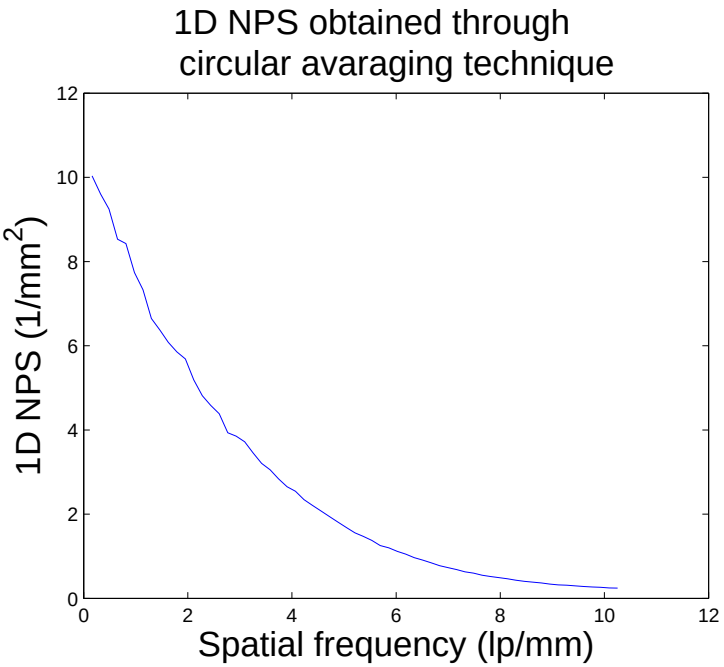

Figure 1.8: 1D NPS obtained from the 2D NPS in Fig. 1.7 through the circular averaging technique

Incident exposure, x-ray quantum noise, and input signal to noise ratio

X-ray counting statistics obey the Poisson distribution [6–8], which means if the average number of photons received per unit area equals Φ, the probability that a unit area receives x photons is [8]:

$$P(X = x) = \Phi^x \frac{e^{-\Phi}}{x!}, \tag{1.5}$$

where X is the random variable representing the number of photons received per unit area.

From the property of Poisson distribution, the variance of the random variable X equals to its mean:

$$std\{X\}^2 = Var\{X\} = E\{X\} = q. \tag{1.6}$$

Therefore, for the incident x-ray field with Φ as the mean number of photons per pixel, the (per area) input SNR (signal to noise ratio) is [6, 8]:

$$SNR_{in} = \frac{E\{X\}}{std\{X\}} = \Phi/\sqrt{\Phi} = \sqrt{\Phi}, \tag{1.7}$$

1.1.2 General system performance and Detective Quantum Efficiency

In the above sections, the image quality related concepts such as contrast, spatial resolution and noise are briefly introduced, in an effort to provide a flavor of this research topic and to pave the way for the following discussion on system performance evaluation and Detective Quantum Efficiency.

By increasing the x-ray dose within the working range of an imaging system, and therefore increasing the input SNR and output SNR, better image qualities could be achieved [3, 6, 7]. However, x-ray radiation is potentially harmful to patient safety. And there is a tradeoff between image quality and patient radiation dose: it is desirable to reduce the radiation dose to a patient to a minimal level (As Low As Reasonable Achievable), while still having good image quality. Thus, how much portion of the total incident x-ray radiation is utilized to form images is a critical question for evaluating and assessing the performance of x-ray imaging systems.

Detective quantum efficiency (DQE), which is widely accepted as the golden rule for quantitatively evaluating the performance of x-ray imaging systems, integrates the concept of SNR, contrast, noise and spatial resolution closely. And it is an excellent description of the dose efficiency of an x-ray imaging system.

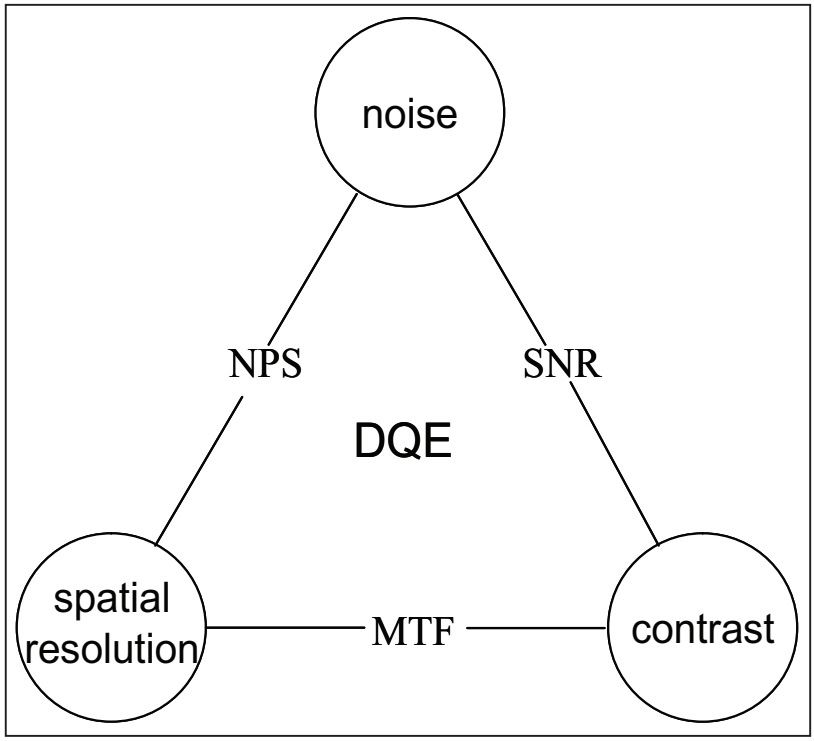

Figure 1.9: Image-quality-related concepts integrated by DQE.

In conceptual terms, DQE is expressed as the SNR transfer of an imaging system, as a function of the spatial frequencies [2, 3, 8, 15, 17–19, 28–32]:

$$DQE(f) = \frac{SNR_{out}^2}{SNR_{in}^2}, \tag{1.8}$$

$$DQE(f) = \frac{S(0)^2 \cdot MTF(f)^2}{NPS(f) \cdot \Phi}, \tag{1.9}$$

where SNR_{in} and SNR_{out} are the input and the output signal-to-noise ratios of the x-ray imaging system, respectively. $MTF(f)$ is the modulation transfer function and $NPS(f)$ is the noise power spectrum. $S(0)$ is the large area signal, and it is the average pixel value of the output images when the detector is irradiated by a uniform beam, which are also the images used to calculate NPS. Φ is the incident number of quanta per unit area, and it equals to the square of the input signal to noise ratio

SNR_{in}^2 according to the Poisson distribution of x-ray photons (Eq. (1.7)).

From Eq. (1.7), (1.8) and (1.9), the output SNR, often referred as NEQ (Noise Equivalent Number of Quanta), is calculated as [2, 3, 8, 15, 17–19, 28–32]:

$$SNR_{out}^2(f) = \frac{S(0)^2 \cdot MTF(f)^2}{NPS(f)} = NEQ(f). \tag{1.10}$$

Fig. 1.10 demonstrated a DQE curve obtained at 26 KV, 0.3 mA, and 3s for a CCD based x-ray imaging system (data published in [27]).

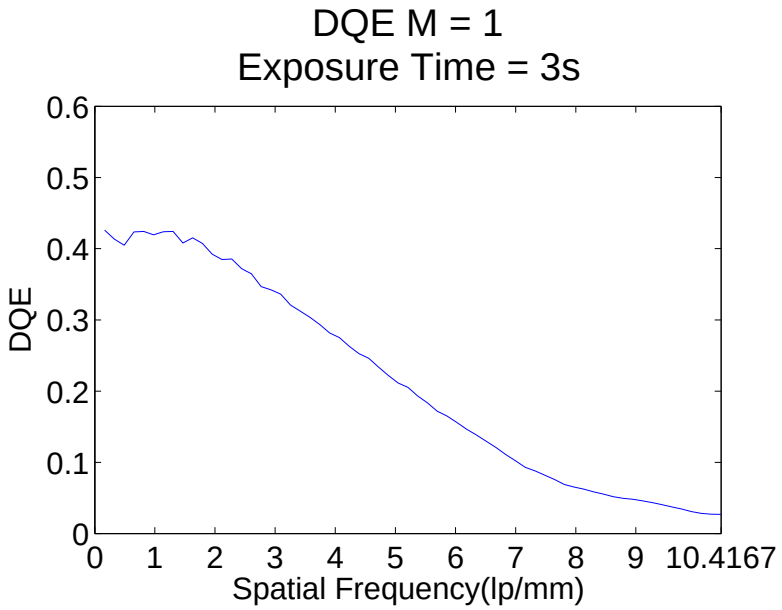

Figure 1.10: DQE curve obtained at 26 KV, 0.3 mA, 3s for a CCD based x-ray imaging system.

1.1.3 Imperfections of the DQE methodology

From Section 1.1.2, one can see that DQE well combines the contrast, spatial resolution, noise characteristic, input dose level, and SNR. Therefore DQE provides a comprehensive objective system evaluation. However, this methodology is not perfect in general agreement, and a lot of research efforts need to be made in order to make the DQE methodology more clinically applicable.

There are several confusing aspects in the current DQE formula, and they are discussed in detail in the following sections. These confusing aspects cause some difficulties in the understanding of the DQE concept and in the interpretation of the DQE results.

Spectral SNR^2_{out} but scalar SNR^2_{in}

From Eq. (1.10), one can observe easily that in the current DQE methodology the output SNR^2_{out} is a spectrum, which provides information of the imaging process in a more micro-scale manner. However, from Eq. (1.7) and the derivation of Φ as the input SNR^2, it is obvious that Φ is a scalar, and a more macro-scale measurement. This inconsistency in the forms of SNR^2_{out} and SNR^2_{in} causes confusion in the understanding of the DQE concept.

Confusing physical model for the DQE measurement

One could be easily confused by the signal and noise defined in the SNR^2_{out}, by observing the form of SNR^2_{out} and the typical methodology to obtain $NPS(f)$, $S(0)$ and $MTF(f)$.

At the output end, $NPS(f)$ and $S(0)$ were both obtained using a series of uniformly exposed images [2, 3, 8, 12, 15, 17–19, 28–32]: $S(0)$ is the mean pixel value of the images; $NPS(f)$ is the noise power spectrum of the images as sample functions of a 2D stochastic process (refer to Section 1.1.1). In this physical scenario utilized to obtain $NPS(f)$ and $S(0)$, the signal is the mean pixel value, and the noise is the fluctuation of the pixel values around their mean. It is straightforward and in fact a standard to represent the noise in frequency domain by NPS [8, 21–23, 25, 26, 33]. However, the way to represent the signal in SNR^2_{out} in this physical scenario is confusing: The signal is represented by $S(0)^2MTF(f)^2$, but what $S(0)^2MTF(f)^2$ really means is the system's response to an impulse signal as the input in the spatial domain,

which results in a flat spectrum that is further modulated by the MTF of the system in the frequency domain. So the input signal in this formula should be an impulse instead of the flat signal, whose frequency-domain representation is a Dirac Delta function which has a peak at zero frequency and zero values elsewhere [9]. Thus, the fact that the frequency domain signal $(S(0)^2 MTF(f)^2)$ is from an impulse input while the frequency domain noise is from a flat input causes inconsistency in the DQE concept.

Fig. 1.11 illustrates a 1D impulse signal and its Fourier transform, and Fig.1.12 illustrates a 1D flat signal and its Fourier transform.

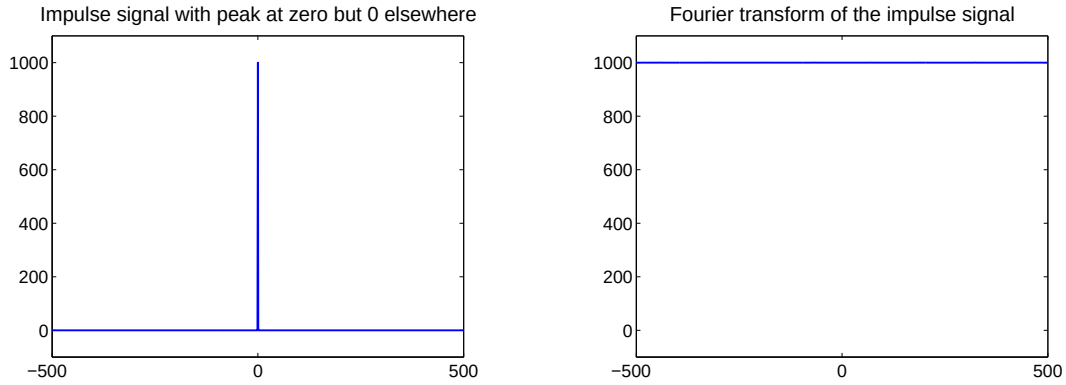

(a) Impulse signal (b) Fourier transform of the impulse signal

Figure 1.11: Illustration of the impulse signal and its Fourier transform

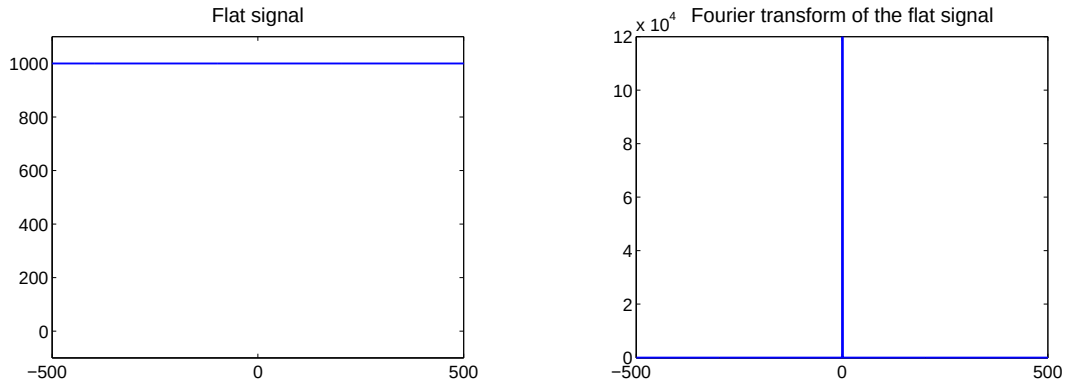

(a) Flat signal (b) Fourier transform of the flat signal

Figure 1.12: Illustration of the flat signal and its Fourier transform

Unit of Φ not intuitive

For digital imaging systems the basic imaging units are pixels (photon receptors), so it's intuitive to define the macro-scale input signal as the mean number of photons per pixel and the macro-scale input noise as the fluctuation (standard deviation) of the number of photons per pixel. By such definition, $\Phi/\sqrt{\Phi}$ is a unit-less quantity, which is more consistent with the concept of SNR. However, the current quantity Φ is the number of incident quanta per unit area, and it has a unit of $1/mm^2$, which is not intuitive and inconsistent with the concept of SNR.

1.2 Overview of the dissertation

This dissertation focuses on the DQE theory and method for digital x-ray imaging systems. After the brief introduction of the current DQE theory and method in this chapter, the theory of DQE is re-derived based on digital x-ray imaging in Chapter 2. Experimental results to support the newly derived DQE theory are also provided in Chapter 2. Then in the following several chapters, different aspects of the DQE measurements, including DQE under magnification, the measurements of photon fluence, x-ray spectra, noise power spectrum, and modulation transfer function, are detailed respectively. Finally, two DQE based imaging system characterization studies were included in Chapter 7 and Chapter 8, as example applications of the DQE methodology.

CHAPTER 2

Theory of DQE based on digital x-ray imaging systems

2.1 Chapter introduction

Detective Quantum Efficiency (DQE) is well accepted as the "golden rule" for the objective evaluation of the performance of x-ray imaging systems, and it is considered an excellent description of dose efficiency [8, 16, 34, 35]. Although DQE has been adopted for digital imaging systems, its original derivation and assumptions are based on a continuous and analogue foundation. It is worth revisiting the DQE theory for the digital systems via the theories of digital signal processing and discrete stochastic processes, in an effort to clarify some confusions and errors in the current DQE methodology.

In this chapter, the theory of detective quantum efficiency for linear digital x-ray imaging systems was derived based on 2D DTFT and presented in detail to clarify some confusing aspects of the DQE methodology for digital imaging systems. The imaging system is considered as a black box with input signal spectrum and noise spectrum at the input end, and output signal spectrum and noise spectrum at the output end. By applying the theory of power spectrum density analysis for linear systems, DQE could be expressed as the ratio between the input signal-to-noise spectrum and the output signal-to-noise spectrum. The assumptions and conditions employed in this derivation were emphasized, and several methodological suggestions were made in an effort to guide the implementation of the DQE measurements. An experimental measurement of DQE for a CCD based x-ray system is also presented to further illustrate the methodology in practice.

2.2 Derivation of the DQE theory based on digital x-ray imaging systems

2.2.1 Definition of signal and noise

A classic experimental scenario was chosen for the derivation of DQE [8]: for each of the repeated exposures the input of the imaging system is a beam that is uniform over the entire imaging area, and the output is the resultant uniform image. The mean number of photons per pixel of the uniform exposure is denoted by q, and the mean output pixel value is designated by p. From the imaging point of view, the signal in the input exposures is the mean number of photons per pixel (q), which corresponds to the output signal–the mean pixel value (p) on the output images; the input noise is the fluctuations in the photon number arriving at individual pixels, which contributes to the output noise–the fluctuations in the output pixel values. Due to the stochastic nature of input and output of the system, it is preferable to use a mathematical treatment based on the theory of stochastic processes for analyzing the imaging performance.

2.2.2 The input and output as random processes

For each uniform exposure, the number of incident photons at the individual pixels (photon receptors) forms a finite-size portion of a member function of a 2D discrete random process that is theoretically defined on an infinitely large domain (denoted by $Q(i,j)$, and (i,j) is the pixel index). When taking multiple exposures under the same imaging condition, multiple member functions of the 2D random process are obtained [8, 21–23, 25, 26]. The process $Q(i,j)$ is assumed as wide-sense stationary (WSS) in order to allow the noise power spectrum (NPS) analysis to be applied [8,21–23,25,26]. For each of the uniform exposure, the output of the system is a uniform image which is again a finite-size portion of a member function of another WSS 2D random process

$P(i,j)$ that is also theoretically defined on infinitely large domain, if the imaging system is assumed to be linear and shift-invariant (stationary) [7, 23, 26, 33, 34].

2.2.3 Input noise power spectrum

.

NPS (also referred as power spectrum density function) of a 2D discrete wide-sense stationary random process is defined as the 2D DTFT (Discrete Time Fourier Transform) [36] of its autocorrelation function of the process [22,23,26]. Without loss of generality, in practice it is customary to work in term of the fluctuation process, i.e., the fluctuation about the mean, which can be easily verified as a WSS process with zero mean, instead of $Q(i,j)$ itself [8, 22, 23, 26, 29, 33, 37]:

$$\Delta Q(i,j) = Q(i,j) - q. \tag{2.1}$$

The autocorrelation function of the zero-mean WSS random process $\Delta Q(i,j)$ is defined as [23, 26]:

$$R_{\Delta Q}(m,n) = E\{\Delta Q(i,j)\Delta Q(i+m, j+n)\}; \tag{2.2}$$

and the NPS for this 2D discrete zero mean WSS process is defined as [23, 26]:

$$\begin{aligned} N_q(u,v) &= \mathcal{D}\{R_{\Delta Q}(m,n)\} \\ &= \sum_{m=-\infty}^{\infty}\sum_{n=-\infty}^{\infty} e^{-j2\pi(um+vn)} R_{\Delta Q}(m,n), \end{aligned} \tag{2.3}$$

where $\mathcal{D}\{\}$ stands for the 2D Discrete Time Fourier Transform (DTFT); $E\{\}$ denotes mathematical expectation; $R_{\Delta Q}(m,n)$ is the autocorrelation function for the input fluctuation process; $N_q(u,v)$ is the NPS for the input fluctuation processes $\Delta Q(i,j)$. (u,v) are the continuous normalized frequencies, and $u, v \in [-\frac{1}{2}, \frac{1}{2}]$.

The numbers of input quanta at each point on the detector plane of an x-ray imaging system can be considered as statistically uncorrelated Poisson random variables [34, 37, 38]. The incident photon numbers at individual pixels, as the sums of uncorrelated random numbers, are also uncorrelated Poisson random variables [26]. As a result, fluctuation of the incident number of photons at individual pixels $\Delta Q(i,j)$ forms a zero-mean white noise process [26], and its autocorrelation function $R_{\Delta Q}(m,n)$ is given by:

$$\begin{aligned} R_{\Delta Q}[m,n] &= E\{\Delta Q(i,j)\Delta Q(i+m,j+n)\} \\ &= \begin{cases} Var\{\Delta Q(i,j)\} = q & \text{for } m=n=0, \\ 0 & \text{otherwise,} \end{cases} \end{aligned} \tag{2.4}$$

where q is the mean number of quanta received per pixel, and according to the Poisson statistics of the incident quanta, it equals to the variance of $Q(i,j)$ and the variance of $\Delta Q(i,j)$.

By Eq. (2.3), it is easy to verify that the NPS of $\Delta Q(i,j)$ is a flat spectrum:

$$\begin{aligned} N_q(u,v) &= \sum_{m=-\infty}^{\infty}\sum_{n=-\infty}^{\infty} e^{-j2\pi(um+vn)} R_{\Delta Q}(m,n) \\ &= \sum_{n,m=0} e^{-j2\pi(um+vn)} R_{\Delta Q}(m,n) \\ &= q. \end{aligned} \tag{2.5}$$

2.2.4 Output noise power spectrum

Based on the assumption of WSS process discussed in section 2.2.2 the output fluctuation process

$$\Delta P(i,j) = P(i,j) - p \tag{2.6}$$

can be treated similarly as in the above section, and p is the mean of the WSS process $P(i,j)$. Again, the NPS of the fluctuation process is calculated in order to represent the noise distribution over spatial frequencies. The autocorrelation function and NPS for the output fluctuation process $\Delta P(i,j)$ are:

$$R_{\Delta P}(m,n) = E\{\Delta P(i,j)\Delta P(i+m,j+n)\}, \tag{2.7}$$

$$N_p(u,v) = \mathcal{D}\{R_{\Delta P}(m,n)\}, \tag{2.8}$$

where $R_{\Delta P}$ and N_p are the autocorrelation function and the NPS of the output fluctuation processes $\Delta P(i,j)$, respectively.

2.2.5 DQE as the comparison of the input and output NPS

Shaw first proposed the approach of NEQ (Noise Equivalent Number of Quanta) and DQE to compare the input and output NPS level, as an evaluation of the performance of imaging processes [8,29,37]. And the basic idea is to convert the output NPS back to the input end of the system via NEQ based on the theory of the propagation of WSS random process through linear systems, and to compare NEQ with the input NPS [8,16,29,34,37]. Following a similar strategy, the NPS of the input fluctuation process can be converted to the output end of the imaging system, and be compared with the NPS of the total output fluctuation. For a practical detector, the total fluctuation in the output image can only be partially attributed to the input fluctuation, i.e., the quantum noise. Therefore the ratio between the converted input NPS (N_q') and the NPS of the total output fluctuation (N_p) is always less than one for real imaging systems. Thus this ratio represents how much noise is introduced by the imaging system into the final output images, and how well the signal-to-noise characteristics of the input are preserved by the imaging system.

For a linear shift-invariant imaging system, the NPS of the resultant output ran-

dom process for a WSS input process is the multiplication of the input NPS and the squared modulus of the transfer function of the linear system [23, 26]:

$$N'_q(u,v) = N_q(u,v)|H(u,v)|^2 \tag{2.9}$$

where $H(u,v)$ is the transfer function of the linear imaging system; $N'_q(u,v)$ is the NPS resulted from only the input fluctuation process that propagates through the imaging system.

$H(u,v)$ for a linear imaging system is actually the OTF of the system, and its modulus equals to the multiplication of the digital gain and the 2D Modulation Transfer Function (MTF) [16, 34, 37]:

$$|H(u,v)| = G \cdot MTF_{2D}(u,v), \tag{2.10}$$

where G is the digital gain of the linear imaging system, and it equals to the slope of the characteristic curve of the system; $MTF_{2D}(u,v)$ is the 2D modulation transfer function, and it equals to the normalized DTFT of the point spread function of the imaging system:

$$H(u,v) = DTFT\{PSF(i,j)\}; \tag{2.11}$$

$$MTF_{2D}(u,v) = \frac{|H(u,v)|}{|H(0,0)|} = \frac{|H(u,v)|}{G}, \tag{2.12}$$

where $PSF(i,j)$ is the point spread function, and it is the output of the imaging system to a point input with magnitude of 1, according to the classic digital system Fourier analysis [36]. For a linear digital imaging system, the digital gain G is constant over the entire linear range and MTF is normalized to 1 at $(0,0)$.

From Eq. (2.5), (2.9), and (2.10), we have:

$$N'_q(u,v) = qG^2 MTF_{2D}(u,v)^2 \tag{2.13}$$

Then we have DQE as the ratio between N'_q and N_p:

$$\begin{aligned} DQE(u,v) &= \frac{N'_q(u,v)}{N_p(u,v)} \\ &= \frac{qG^2MTF^2_{2D}(u,v)}{N_p(u,v)} \\ &= \frac{q(\frac{p}{q})^2MTF^2_{2D}(u,v)}{N_p(u,v)} \\ &= \frac{p^2MTF^2_{2D}(u,v)}{N_p(u,v)\cdot q}, \end{aligned} \tag{2.14}$$

where p is the mean pixel value of the output image that corresponds to the average number of photons per pixel q; u, v are the continuous normalized spatial frequencies, and $u, v \in [-\frac{1}{2}, \frac{1}{2}]$.

It is often more convenient to express NPS and MTF in 1D rather than 2D domain [8, 12, 16, 34, 39], generally as $MTF(f) = MTF_{2D}(u,v)|_{u\ or\ v=0}$ and $NPS(f) = N_p(u,v)|_{u\ or\ v=0}$. And the 1D formula for DQE is:

$$DQE(f) = \frac{p^2MTF^2(f)}{NPS(f)\cdot q}, \tag{2.15}$$

where f is the 1D normalized spatial frequency, and $f \in [-\frac{1}{2}, \frac{1}{2}]$.

2.3 Discussion on the DQE theory for digital x-ray imaging systems

2.3.1 The physical meaning of the DQE spectrum

From Section 2.2.5 it can be seen that DQE is actually the ratio between the deduced version of the input NPS and the output NPS, as a function of spatial frequencies. As stated in Section 2.2.1, the input and output signals are constant values over the spatial indices. The input signal power spectrum (power spectrum density function

of the signal) $S_q(u,v)$ is thus an impulse function:

$$S_q(u,v) = \mathcal{D}\{E\{q * q\}\} = q^2\delta(u,v), \tag{2.16}$$

where q is the mean number of photons per pixel, and

$$\delta(u,v) = \begin{cases} 1 & u = v = 0 \\ 0 & otherwise. \end{cases} \tag{2.17}$$

Similarly, the output signal power spectrum (power spectrum density function of the signal) $S_p(u,v)$ is also an impulse function:

$$S_p(u,v) = p^2\delta(u,v), \tag{2.18}$$

where p is the mean output pixel value.

Following the same relationship described by Eq. (2.9), the input signal power spectrum deduced from the input to the output ($S'_q(u,v)$) is equal to the output signal power spectrum:

$$\begin{aligned} S'_q(u,v) &= S_q(u,v)|H(u,v)|^2 \\ &= q^2\delta(u,v) \cdot G^2 MTF_{2D}(u,v) \\ &= q^2\delta(u,v) \cdot G^2 \\ &= p^2\delta(u,v) \\ &= S_p(u,v). \end{aligned} \tag{2.19}$$

Therefore, the DQE in Eq. (2.14) can be re-written as the ratio between the output SNR spectrum and the input SNR spectrum, which are both defined in the sense of

power spectrum density functions:

$$\begin{aligned} DQE(u,v) &= \frac{N_q'(u,v)}{N_p(u,v)} \\ &= \frac{1/N_p(u,v)}{1/N_q'(u,v)} \\ &= \frac{S_p(u,v)/N_p(u,v)}{S_q'(u,v)/N_q'(u,v)} \\ &= \frac{SNR_{out}(u,v)}{SNR_{in}(u,v)}. \end{aligned} \tag{2.20}$$

It needs to be pointed out that although in Eq. (2.14) and (2.15) q can be interpreted as the large scale SNR_{in}^2 because of the Poisson statistics of incident photons, such interpretation can be easily misleading since q is in fact the incident NPS, which happens to be constant as the result of the uncorrelation property of the incident photons at individual pixels.

2.3.2 DTFT to DFT and the normalized frequency

In this derivation, the input and output of the digital imaging system are discrete random processes, and hence the index (i,j) for $Q(i,j)$, $P(i,j)$ are dimensionless. As a result of sampling and DTFT, we have $u,v,f \in [-\frac{1}{2},\frac{1}{2}]$ in Eq. (2.3), (2.14), and (2.15), as they have been normalized to the sampling frequency F_s ($F_s = 1/\Delta x$) [36]. Δx is the sampling interval (pixel pitch) of the imaging device. When interpreting the MTF, NPS and DQE in terms of the non-normalized analogue spatial frequencies, the normalized spatial frequencies u,v,f should be mapped linearly from $[-0.5,0.5]$ to $[-F_{Nyquist},F_{Nyquist}]$ ($F_{Nyquist} = 1/(2\Delta x)$) [36].

In practice, Digital Fourier Transform (DFT) and its fast algorithm FFT are widely used in the situations where DTFT is applicable [36, 40]. The relationship between DFT/FFT and DTFT for an N-by-N array $x(i,j)$ is that the N-by-N-point DFT is the samples of the DTFT of $x(i,j)$ at N-by-N evenly spaced frequency points

over $u, v, f \in [-\frac{1}{2}, \frac{1}{2}]$, and the sampling interval ($1/N$ in normalized spatial frequencies and $1/(\Delta x \cdot N)$ in analogue spatial frequencies) partially determines frequency resolution of the calculated spectra [36].

2.3.3 Relationship with the widely accepted DQE formula

By comparing Eq. (2.14) and Eq. (2.15) with the widely accepted DQE formula [16, 31, 34, 35], one can easily figure out that they share the same form:

$$DQE(f) = \frac{LAS^2 \cdot MTF(f)^2}{NPS(f) \cdot N}, \tag{2.21}$$

where LAS stands for the large area signal, which is the mean output pixel value; N is the number of photons per unit area; $MTF(f)$ and $NPS(f)$ are functions of the 1D physical continuous spatial frequency. As compared to (u, v), the physical spatial frequency is not normalized by the sampling frequency F_s ($F_s = 1/\Delta x$), and often takes the unit of line-pair per mm (lp/mm).

However, it needs to be pointed out that the q in Eq. (2.14) is the average number of incident photons "per pixel" rather than "per unit area" as N is defined in the widely accepted formula (Eq. (2.21)) . The relationship between q and N is:

$$q = N \cdot \Delta x^2, \tag{2.22}$$

where Δx^2 denotes the pixel area of the detector.

One also has to note that if the periodogram estimator [22, 23, 33] is employed to determine the output NPS $N_p(u, v)$, there is no Δx^2 (Δx^2 denotes the pixel size of the detector) in the output NPS formula (refer to Eq. (2.24)) in this derivation, and the resultant NPS is dimensionless (dimensionless value, dimensionless frequency). This

is different from the formula used in [12, 16, 31, 34, 35]:

$$\frac{\Delta x^2}{MN}|\mathcal{D}\{\Delta P(i,j)\}|^2. \tag{2.23}$$

This difference is due to the fact that the derivation in this study is based on discrete domain, while the formula used in [16, 34] is based on continuous domain. The result of these differences in q and output NPS $N_p(u,v)$ actually makes Eq. (2.15) exactly the same as the widely accepted DQE formula, since $q/\Delta x^2 =$ *number of photon per unit area*.

2.3.4 Frequency resolution in the estimation of NPS

As mentioned in Section 2.2.2, the input and output are finite-size portions of the member functions of two 2D discrete random processes which are defined theoretically on infinitely large spatial domain. Therefore, there exists an intrinsic cutting window that cuts out the finite-size portion by multiplying itself against the member functions. The estimation of NPS based on limited amount of data is a very important application in the field of stochastic signal processing, and extensive research efforts have been dedicated to this topic (a relatively comprehensive list of literatures can be found in [22]). In this study, we try to only provide enough information to support our analysis. In practice, by assuming ergodicity of the random process [8, 22, 23, 26, 29, 33, 34, 37], the NPS for the output images is often estimated using periodograms [8, 11, 12, 22, 23, 26, 29, 33, 34, 37]. For a discrete 2D WSS random process, the periodogram estimator for the output NPS is [23, 26, 33]:

$$\widehat{N_p}(u,v) = \frac{1}{MN}|\mathcal{D}\{\Delta P(i,j)\}|^2, \tag{2.24}$$

where M and N are the number of pixels on the two dimensions of the fluctuation image $\Delta P(i,j)$; $u, v \in [-\frac{1}{2}, \frac{1}{2}]$ are the normalized continuous spatial frequencies.

The periodogram estimator $\widehat{N_p}$ is often referred as an asymptotically unbiased estimator [8, 22, 23, 26, 29, 33], which means when the dimensions of the fluctuation image are infinitely large, the ensemble average of the periodogram estimator ($\widehat{N_p}(u,v)$) converges to the true NPS $N_p(u,v)$:

$$\lim_{M,N\to\infty} E\{\widehat{N_p}(u,v)\} = N_p(u,v). \tag{2.25}$$

Although the mean of $\widehat{N_p}(u,v)$ converges to the true output NPS as the size of the image data used in the periodogram estimator increases, the variance of the estimator does not reduce as the size increases. Moreover, it remains relatively large: for example, for a zero-mean white Gaussian sequence, the relative standard deviation of its periodogram estimator is 100% [23]. Therefore, ensemble averaging of the estimator $\widehat{N_p}(u,v)$ is necessary to reduce the variance and to improve the quality of the NPS measurements [12, 23].

A common practice to reduce the variance of the periodogram results is: firstly, partition a fluctuation image into multiple sub-images, and secondly, average the periodograms calculated from the sub-images to obtain the mean periodogram [12, 16, 22, 23]. For a given amount of image data, there is a trade-off between the variance level of the periodogram estimators and the severeness of the "spectral leakage" problem [12, 22, 23, 26, 33]: reducing the size of the sub-images can provide more periodograms to be averaged, and hence can reduce the variance by a factor of the number of sub-images; but the reduced size of the sub-images can also cause smaller window to be multiplied to the true image for cutting out the sub-images, which is equivalent to convolving the actual spectra with the a wider blurring filter (DTFT of the cutting window) in the frequency domain. This causes the resultant spectra to be blurred more severely [36].

The severeness of the frequency leakage is determined by the size and the shape of

the cutting window [12,36], and the sampling rate of the discrete spectra is determined by the number of points used in the DFT calculation. Therefore, the frequency resolution of NPS is determined by both the frequency leakage and the frequency sampling, and improving the frequency resolution requires the improvement from both directions. The effects of different size and shape of the cutting window on the estimation of NPS have already been discussed in [12], and in this report we will discuss the other aspect of the problem: improvement in the frequency sampling rate of in the NPS estimation.

If an $N \times N$ rectangular window is used in the periodogram estimation, which simply cuts the sub-images of $N \times N$ pixels out of the original image, the main lobe width of the window's DTFT is $2/N$ in normalized spatial frequency ($2/(\Delta x \cdot N)$ in analogue spatial frequency) on both dimensions [36]. The size of the cutting window determines the intrinsic frequency resolving power of the periodogram. This means two closely spaced peaks in the true NPS can be clearly resolved if the difference in their frequencies larger than approximately half of the main lobe width ($1/N$ in normalized spatial frequency, and $1/(\Delta x \cdot N)$ in analogue spatial frequency). If the $N \times N$ data points are directly utilized in the DFT calculation, an $N \times N$ matrix of samples is used to represent the windowed periodogram with a frequency interval of $1/N$ in normalized spatial frequency ($2/(\Delta x \cdot N)$ in analogue spatial frequency). If, for example, a peak in this case is about $2/N$ (in analogue spatial frequency) wide in one dimension, only 2 peak lines are used to present it, which certainly loses its shape. In order to improve the frequency sampling rate, the size of DFT can be increased using the "zero-padding" technique.

The basic idea of "zero padding" is to append zero-valued points to the original data array, in order to get denser sampling of the resultant DTFT without changing its values [33, 36, 40]. For an N-by-N array $x(i, j)$, a new M-by-M ($M > N$) array

$x_p(i,j)$ is formed by adding $M^2 - N^2$ zero-valued data points:

$$x_p(i,j) = \begin{cases} x(i,j) & 0 \le i,j \le N-1, \\ 0 & N \le i,j \le M-1, \end{cases} \tag{2.26}$$

then the M-by-M point FFT can be calculated for $x_p(i,j)$ $(0 \le i \le M-1, 0 \le i \le M-1)$. The benefit of this zero padding is that it increases the number of sample points of the DFT results but does not change the value of the spectra [33, 36, 40]. A more detailed example will be provided in Section 2.4.

2.3.5 Practical suggestions for the implementation of DQE methodology

Along the derivation of the DQE concept and formulae, several assumptions are made and need to be taken as prerequisite conditions on which the DQE methodology could be correctly implemented:

- The assumption on the WSS property for both input and output noise;
- The assumption on the ergodicity of the output noise process on which the periodogram estimator is based;
- The assumption on the system as linear and shift-invariant based on which the Fourier transform based linear system analysis is valid;
- The assumption that the incident photons are statistically uncorrelated Poisson random variables, from which the flat input NPS is derived;
- An easily ignored assumption: the input exposures and output images are assumed as the member functions of the respective input and output random processes, which has an underlying assumption that the imaging conditions for the exposures are repeatable.

Based on the assumptions and the discussion in Section 2.2 and 2.3, attentions should be paid on several aspects of the DQE implementation:

- If there is any non-uniform object/filtration in the beam, the distance between the object/filter and the detector needs to be large enough to satisfy the assumption of statistically uncorrelated incident photons.
- If there are trends or artifacts in the output images, flat-fielding or other anti-trend/anti-artifact procedures need to be applied before the calculation of output NPS.
- Repeatability of tube output needs to be justified for DQE measurements.
- Make sure the detector works in its linear range during the exposures.
- In NPS calculation using periodograms, ensemble averaging of the periodograms is necessary to reduce the variance of the estimation; the periodogram estimator is more biased if the number of pixels involved in the formation of periodogram is small; window masking techniques may improve the quality of the NPS measurements by relieving the "spectral leakage" problem [12, 22, 23, 26, 33].

2.4 Experimental results based on the newly derived DQE theory

The measurement of DQE for a digital x-ray imaging system (MX-20, Faxitron X-Ray Corporation, Wheeling, IL) is presented here as an example of the above discussion on the DQE analysis. The system employs an x-ray source with a tungsten target and a 0.25mm-thick Beryllium window. The detector used in this system is based on two abutted 1024px-by-1024px CCD arrays (KAF-1001E, Eastman-Kodak, New York) and a Min-R scintillating screen (Eastman-Kodak, Rochester, NY), and the effective pixel pitch is 48 μm. The SID of the system is 57.2 cm. During the DQE

measurements, the x-ray system was operated at 26 kVp and 0.3 mA, without any additional filtration.

1D MTF of this imaging system was measured based on the slit method [39], with the help of a 10 μm wide slit camera (IIE GmbH, Aachen, Germany). As the CCD detector demonstrates the property of circular symmetry [10–12], the 2D MTF was calculated by fitting the data points that is of a distance r from the origin on the 2D MTF with the data points r away from the origin on the 1D MTF:

$$MTF_{2D}(u,v) = MTF_{1D}(\sqrt{u^2+v^2}) \tag{2.27}$$

The incident number of photons per pixel q was determined through the measurement of exposure level and the incident spectrum used in the NPS measurement [10, 41]. The exposure level of the incident x-ray during each shot of the NPS measurements was measured with a calibrated ion chamber (Radcal 1015 system with 10X5-6M chamber, Radcal Corp., CA), and the average exposure of 10 repeatedly measurements at 26 kV, 0.3 mA, 3 s, was determined as 346.6 mR.

The incident spectrum was determined through the use of an x-ray spectrometer (Amptek Inc., MA). In order to ensure accurate alignment for the spectral measurements, the alignment of the spectrometer with the x-ray source was performed according to a previous study [42]. Photon fluence per exposure (number of photons per mm^2 per mR, denoted by $\frac{\Phi}{X}$) was first calculated from the spectral measurements [32,43] as approximately 8982.9 $(mm^2 \cdot mR)^{-1}$. Then this number is multiplied by the exposure level (in mR, denoted by X) and the area of the pixel ($\Delta x^2 = 0.048^2 mm^2$) to obtain

q (photon/pixel):

$$\begin{aligned} q &= \frac{\Phi}{X} \cdot X \cdot \Delta x^2 \\ &= 8982.9(mm^2 \cdot mR)^{-1} \cdot 346.6mR \cdot (0.048)^2 mm^2 \\ &= 7173.4 \end{aligned} \tag{2.28}$$

2D and 1D NPS was measured through 200 repeated exposures of 26 kVp, 0.3 mA, 3 s, and without any added filtration. This exposure technique was within the detector's linear response range, and resulted in a mean output pixel value of 1888.0 out of the detector's full dynamic range ([0, 4095]). The central region of interest (ROI) of 512×512 pixels from the left CCD array was selected to avoid the non-uniformities near the boundaries of the detector. The ROIs were corrected to remove any background trend and fixed pattern noise by flat fielding [44], and then partitioned into sub-images for the aforementioned periodogram estimation of NPS according to Eq. (2.24), and the mean periodogram was calculated by averaging the resultant periodograms.

In order to demonstrate the improvement of spatial frequency resolution from zero-padding used in the estimation of NPS (as mentioned in Section 2.3.4), periodograms from sub-image of 64×64 pixels were calculated with different level of zero-padding to obtain FFT of 64×64, 128×128, 256×256 and 512×512 points, and are presented in Fig. 2.1, 2.2, 2.3, and 2.4. One-dimensional NPS on both the horizontal and vertical axes of the 2D NPS were also plotted in Fig. 2.5, 2.6, 2.7, and 2.8, in an effort to present the NPS data in a more detailed manner.

To compare the differences in the estimation of NPS introduced by partitioning the region of interest into sub-image of different sizes, periodograms from sub-images of 64×64, 128×128, 256×256, and 512×512 pixels were calculated using the same FFT size of 512×512 points, in an effort to provide a common frequency resolution

among the resultant spectra. The one-dimensional NPS on both the horizontal and vertical axes of the 2D NPS were plotted in Fig. 2.9, 2.10, 2.11, and 2.12.

The 2D DQE were calculated by combining the 2D NPS, 2D MTF, q, and mean output pixel values p. 2D DQE obtained using different FFT sizes (64×64, 128×128, 256×256 and 512×512 points) and the same 64px-by-64px sub-images were compared in Fig. 2.13, 2.14, 2.15, and 2.16 to show the improvement in the frequency resolution. Similar to 1D NPS curves, the 1D DQE obtained on both the horizontal and vertical axes of the 2D DQE were presented in Fig. 2.17, 2.18, 2.19,and 2.20 to show the data in a more detailed manner. DQE obtained with a constant FFT size of 512×512 but different sub-image sizes of 64×64, 128×128, 256×256 and 512×512 pixels were also calculated, and the 1D DQE curves were compared in Fig. 2.21, 2.22, 2.23, and 2.24 to show the difference caused by the various sizes of sub-images, based on a common frequency resolution among the resultant spectra.

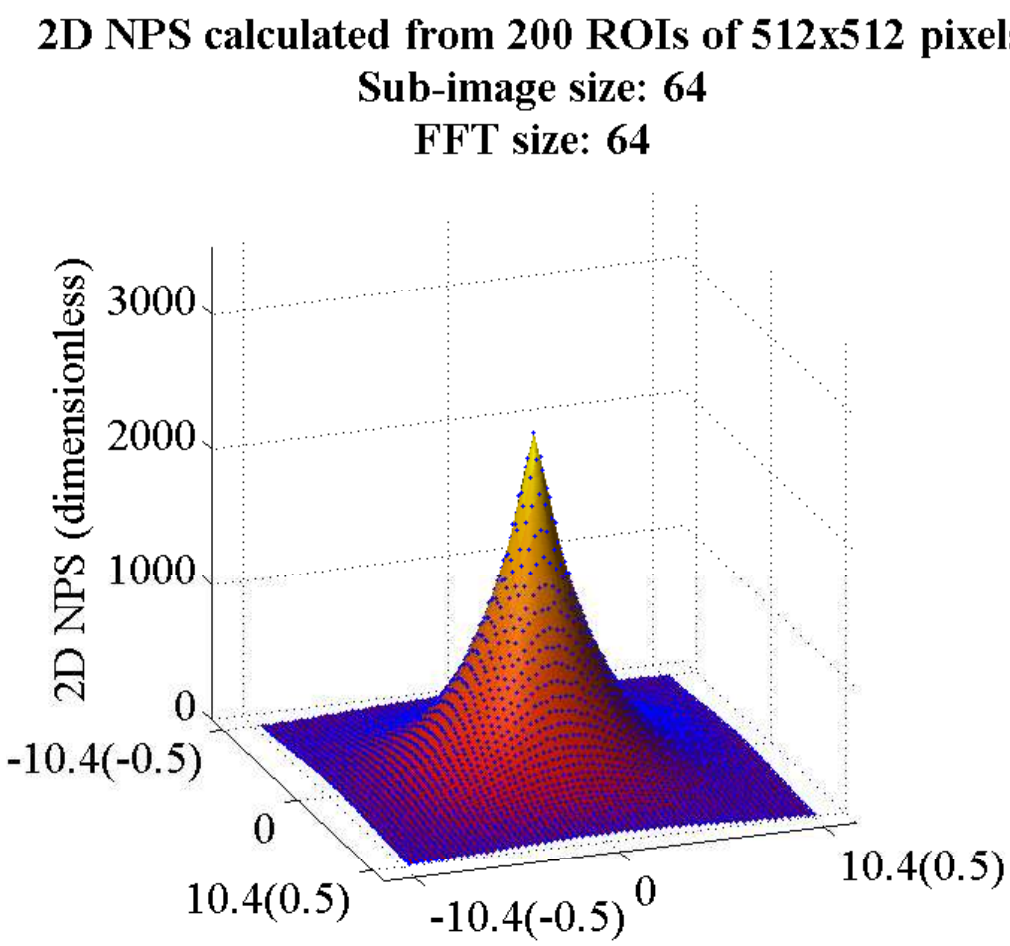

Figure 2.1: 2D NPS obtained with 64px-by-64px sub-images and FFT size of 64x64 (zero-padding not applied)

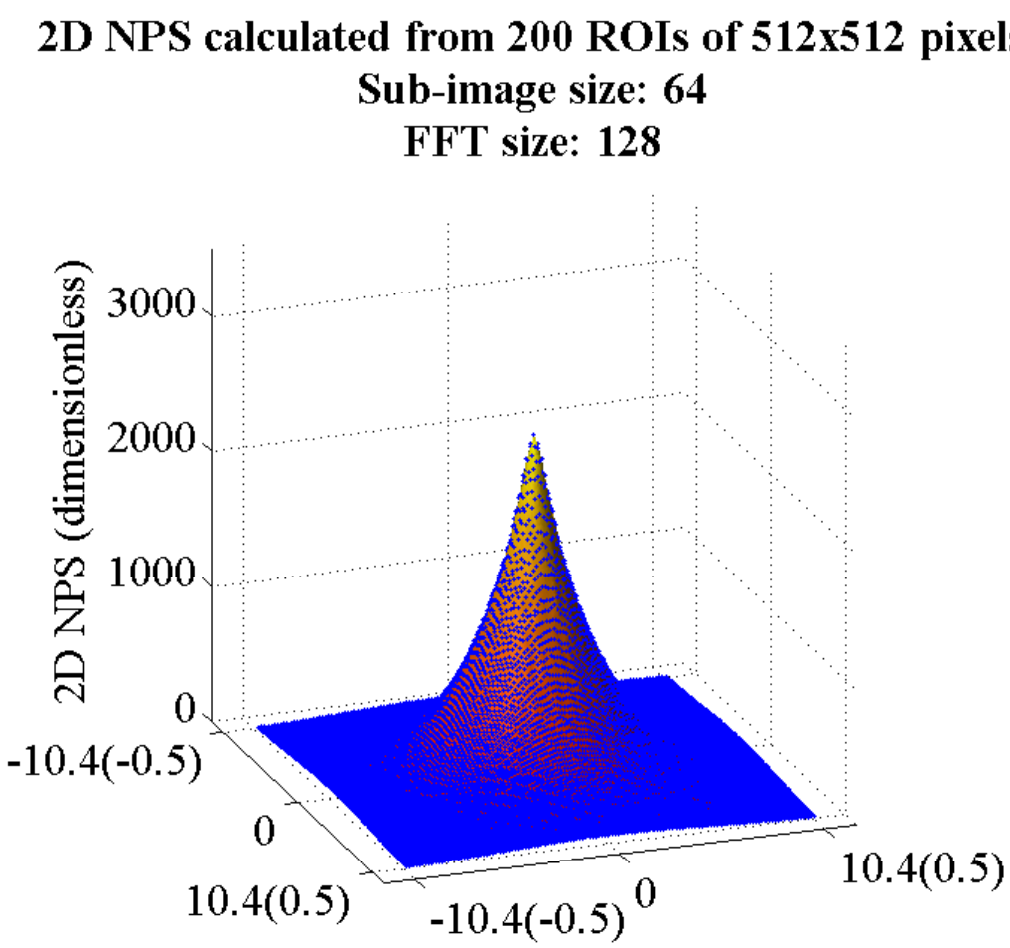

Figure 2.2: 2D NPS obtained with 64px-by-64px sub-images and FFT size of 128x128 (x4 zero-padding applied)

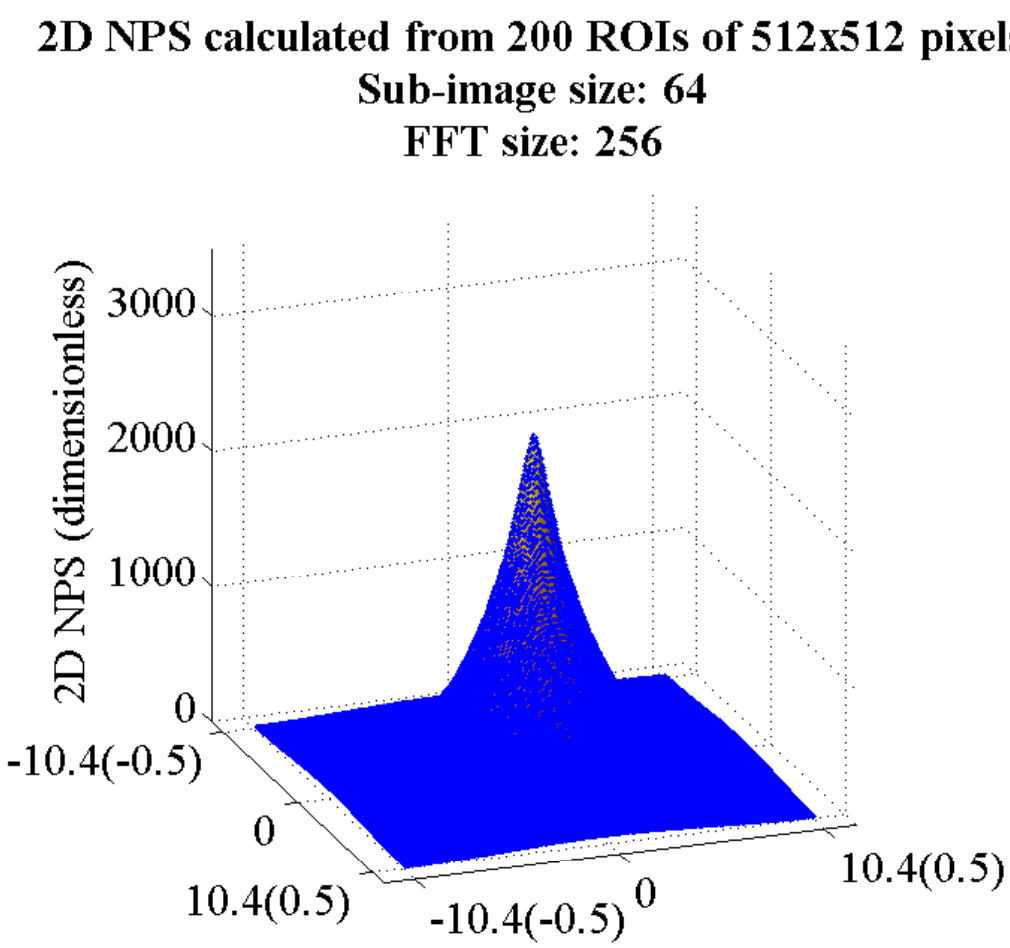

Figure 2.3: 2D NPS obtained with 64px-by-64px sub-images and FFT size of 256x256 (x16 zero-padding applied)

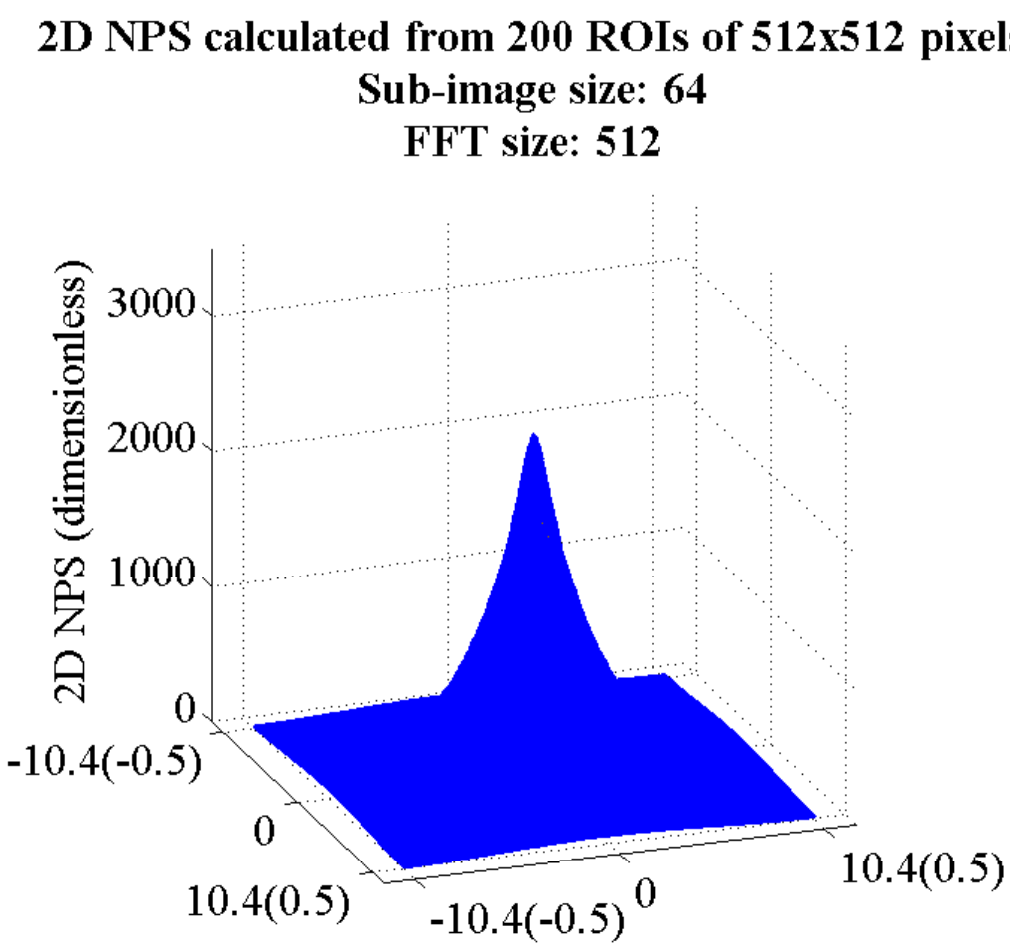

Figure 2.4: 2D NPS obtained with 64px-by-64px sub-images and FFT size of 512x512 (x64 zero-padding applied)

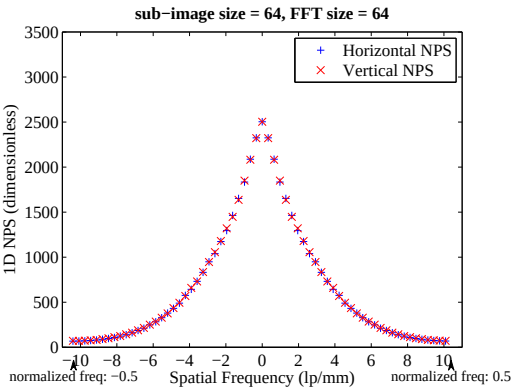

Figure 2.5: 1D NPS obtained with 64px-by-64px sub-images and FFT size of 64x64 (zero-padding not applied)

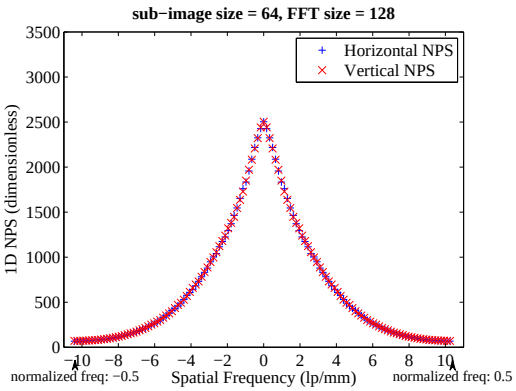

Figure 2.6: 1D NPS obtained with 64px-by-64px sub-images and FFT size of 128x128 (x4 zero-padding applied)

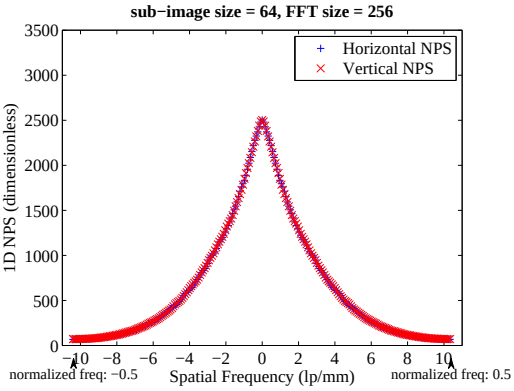

Figure 2.7: 1D NPS obtained with 64px-by-64px sub-images and FFT size of 256x256 (x16 zero-padding applied)

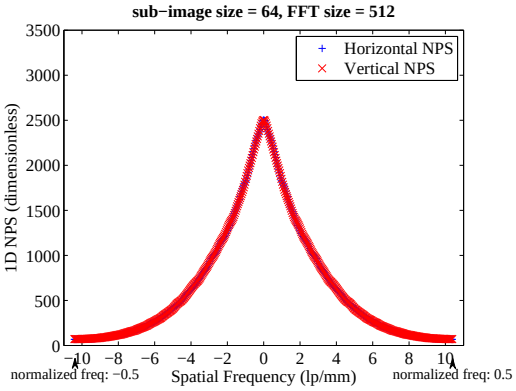

Figure 2.8: 1D NPS obtained with 64px-by-64px sub-images and FFT size of 512x512 (x64 zero-padding applied)

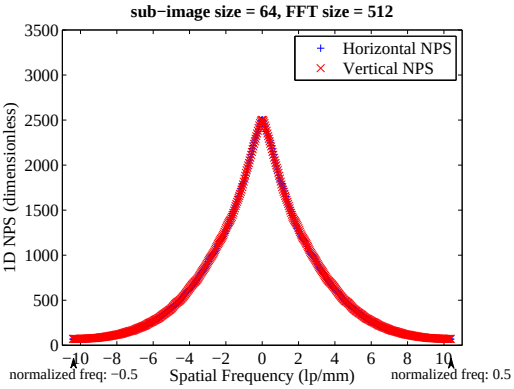

Figure 2.9: 1D NPS obtained with 64px-by-64px sub-images and FFT size of 512x512 (x64 zero-padding applied)

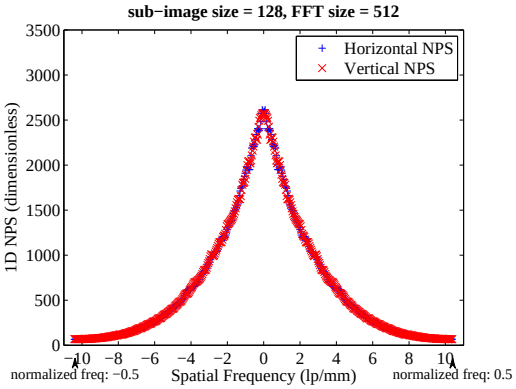

Figure 2.10: 1D NPS obtained with 128px-by-128px sub-images and FFT size of 512x512 (x16 zero-padding applied)

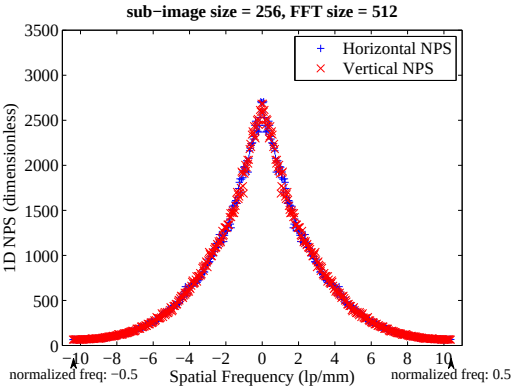

Figure 2.11: 1D NPS obtained with 256px-by-256px sub-images and FFT size of 512x512 (x4 zero-padding applied)

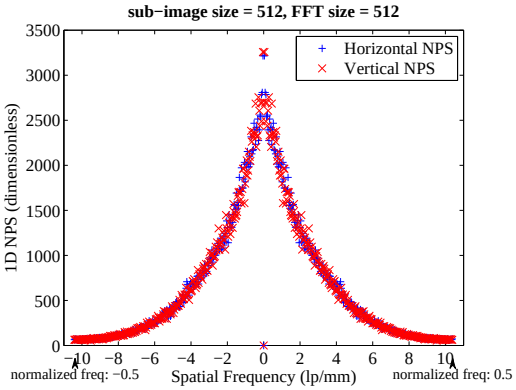

Figure 2.12: 1D NPS obtained with 512px-by-512px sub-images and FFT size of 512x512 (zero-padding not applied)

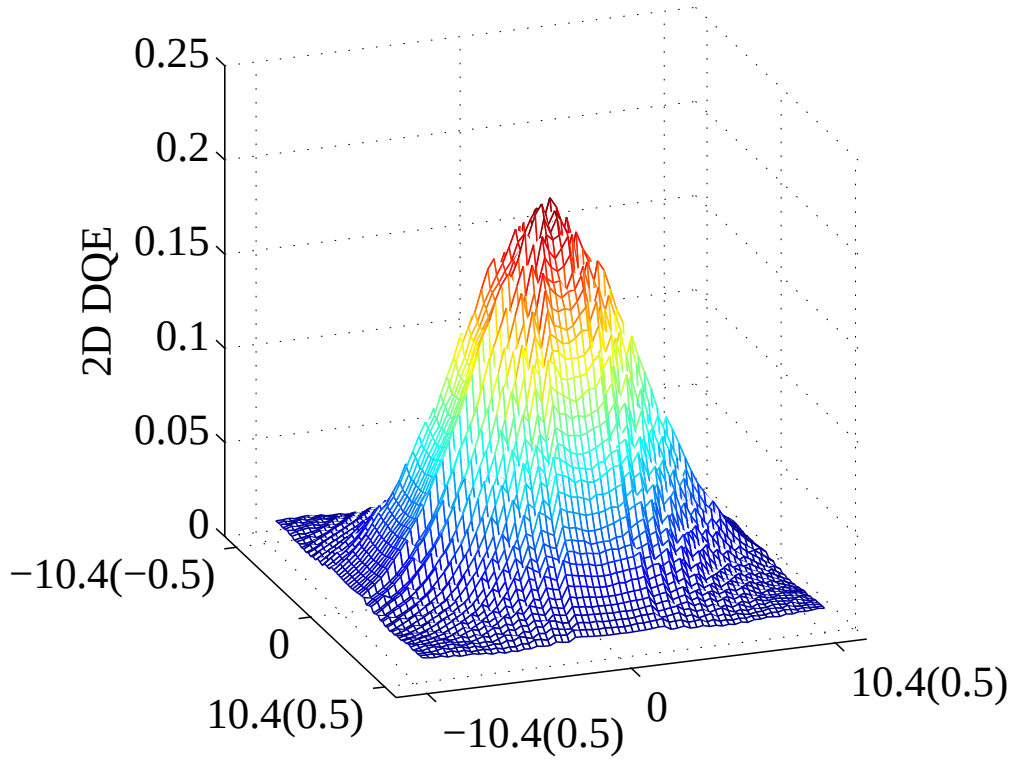

Figure 2.13: 2D DQE obtained with 64px-by-64px sub-images and FFT size of 64x64 (zero-padding not applied)

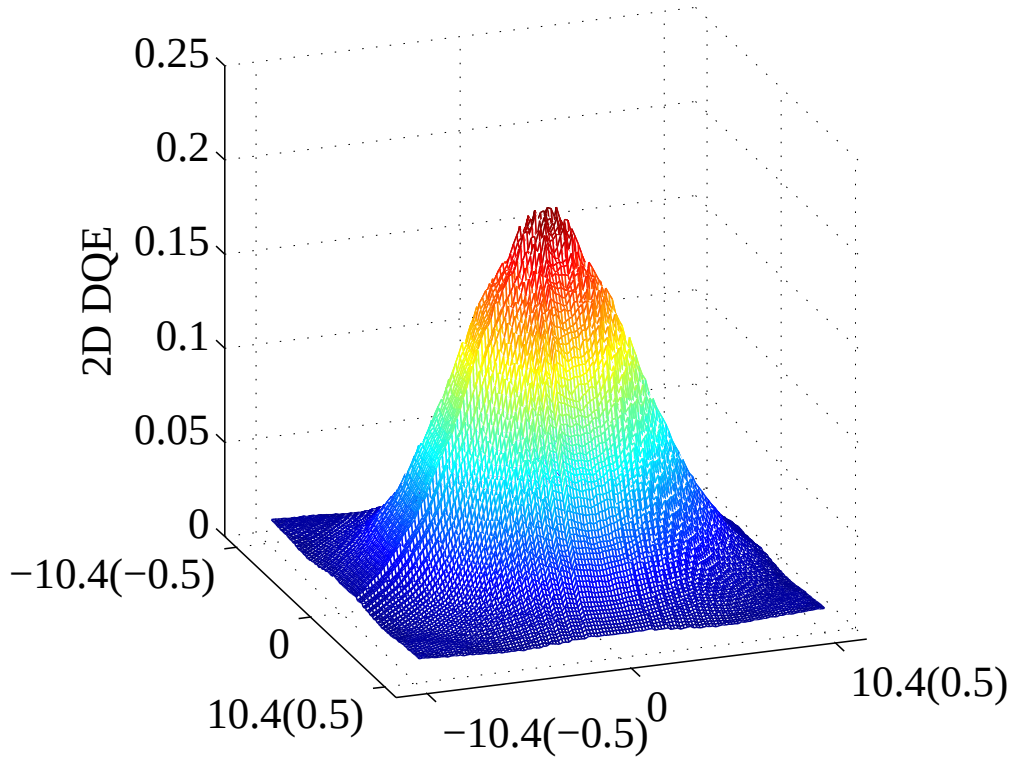

Figure 2.14: 2D DQE obtained with 64px-by-64px sub-images and FFT size of 128x128 (x4 zero-padding applied)

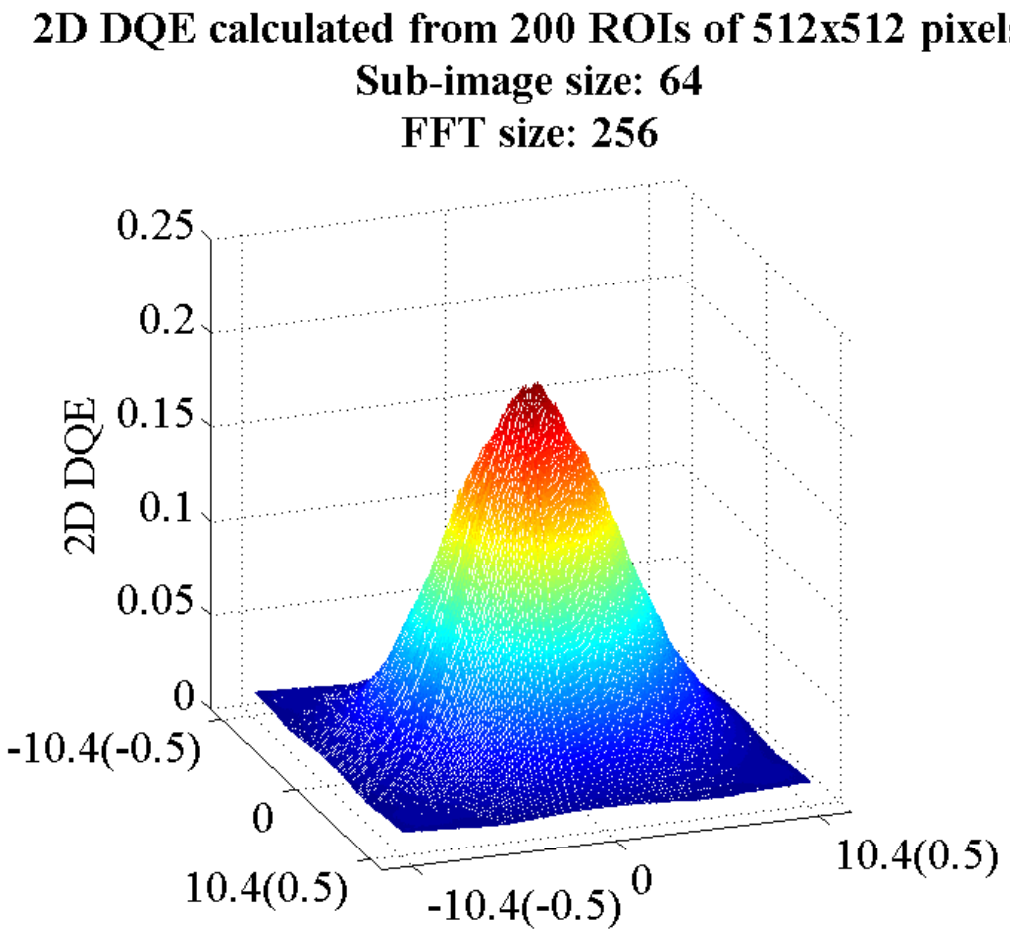

Figure 2.15: 2D DQE obtained with 64px-by-64px sub-images and FFT size of 256x256 (x16 zero-padding applied)

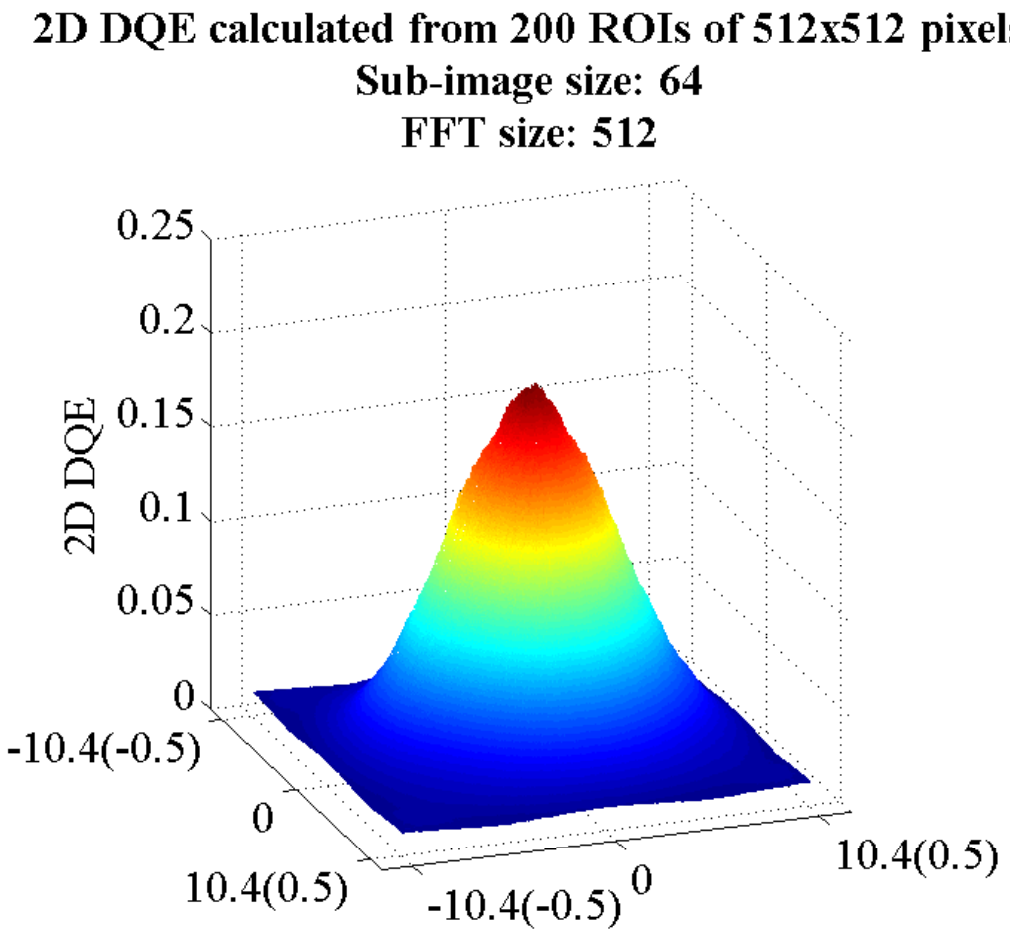

Figure 2.16: 2D DQE obtained with 64px-by-64px sub-images and FFT size of 512x512 (x64 zero-padding applied)

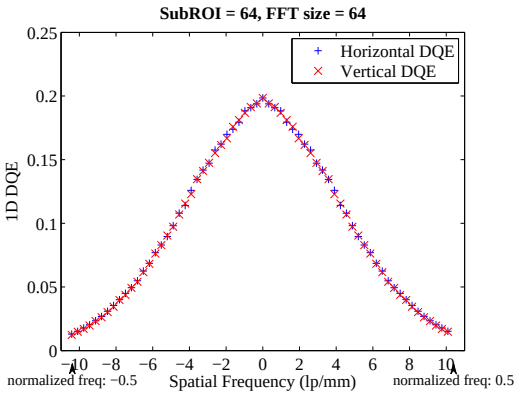

Figure 2.17: 1D DQE obtained with 64px-by-64px sub-images and FFT size of 64x64 (zero-padding not applied)

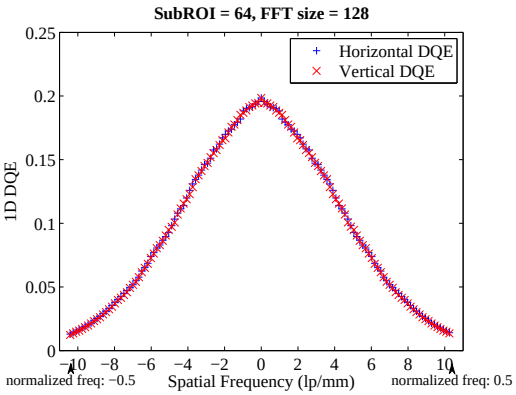

Figure 2.18: 1D DQE obtained with 64px-by-64px sub-images and FFT size of 128x128 (x4 zero-padding applied)

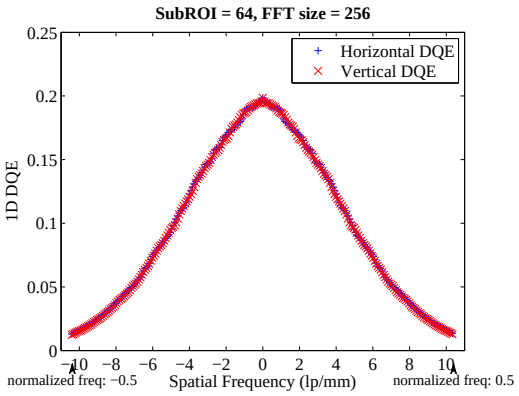

Figure 2.19: 1D DQE obtained with 64px-by-64px sub-images and FFT size of 256x256 (x16 zero-padding applied)

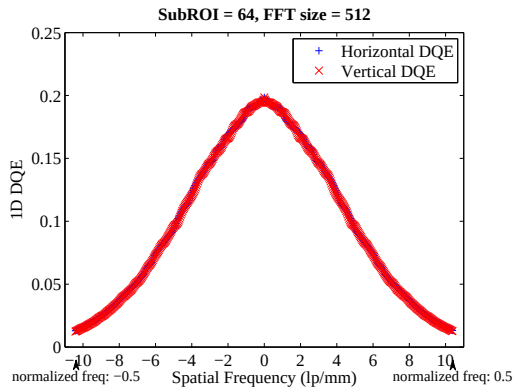

Figure 2.20: 1D DQE obtained with 64px-by-64px sub-images and FFT size of 256x256 (x64 zero-padding applied)

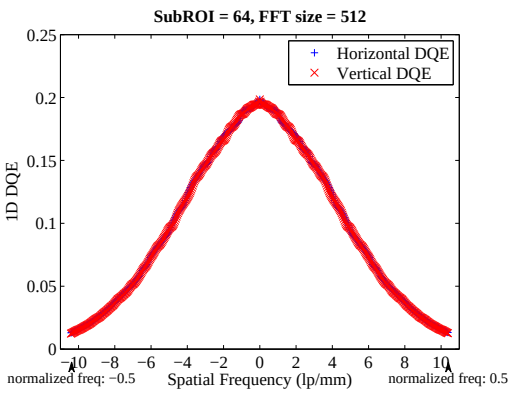

Figure 2.21: 1D DQE obtained with 64px-by-64px sub-images and FFT size of 512x512 (x64 zero-padding applied)

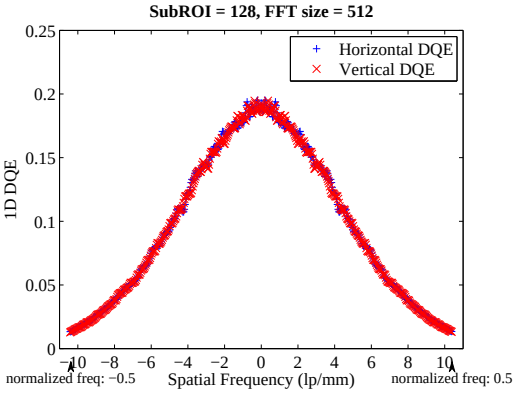

Figure 2.22: 1D DQE obtained with 128px-by-128px sub-images and FFT size of 512x512 (x16 zero-padding applied)

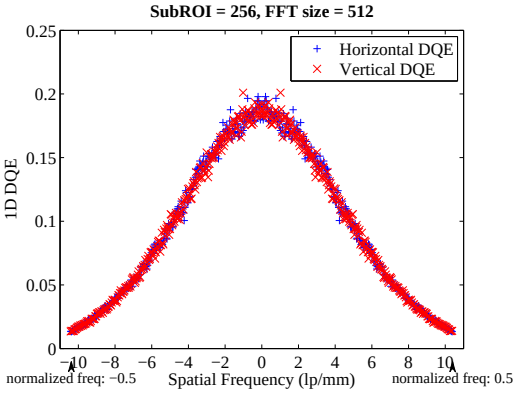

Figure 2.23: 1D DQE obtained with 256px-by-256px sub-images and FFT size of 512x512 (x4 zero-padding applied)

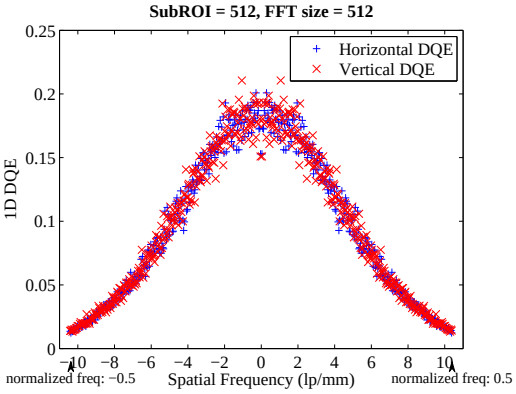

Figure 2.24: 1D DQE obtained with 512px-by-512px sub-images and FFT size of 512x512 (zero-padding not applied)

In the 2D NPS and 2D DQE figures, the x and y axes denotes the frequencies on both horizontal and vertical axes. The analogue spatial frequencies range in $[-1/(2 \cdot \Delta x)), 1/(2 \cdot \Delta x))]$ ([-10.4, 10.4] lp/mm for $\Delta x = 0.048mm$ in this study), and the corresponding normalized spatial frequencies range in [-0.5, 0.5]. For an FFT size

of M-by-M in the calculation of periodograms, the smallest frequency interval of the spectra in the sense of analogue spatial frequency is determined as $1/(\Delta x \cdot M)$, and are 0.3255 lp/mm, 0.1628 lp/mm, 0.0814 lp/mm, and 0.0407 lp/mm for the FFT sizes of 64×64, 128×128, 256×256, and 512×512 points, respectively. In the sense of normalized spatial frequency which ranges in [-0.5, 0.5], the frequency intervals are determined as $1/M$ for an M-by-M FFT, and are 1/64, 1/128, 1/256, and 1/512 for the FFT sizes of 64×64, 128×128, 256×256, and 512×512 points, respectively.

As can be seen in Fig. 2.1, 2.2, 2.3, and 2.4, the sampling rate increases with increased FFT size, as a result of zero-padding. The same improvement can be also seen in Fig. 2.5, 2.6, 2.7, and 2.8. As stated in Section 2.3.4, the shape of the NPS curves was not changed when using zero-padding, but the frequency resolution was improved significantly.

When sub-images of different sizes were used in the NPS estimation, the total number of individually obtained periodograms averaged to obtain the final output NPS varied. For the sub-images of 64x64 pixels, 128x128 pixels, 256x256 pixels, and 512x512 pixels, the total number of periodograms used in the averaging were 12800 ($200 \times (512/64)^2$), 3200, 800, and 200, respectively. This difference resulted in different smoothness of the respective NPS curves, as can be seen in Fig. 2.9, Fig. 2.10, Fig. 2.11, and Fig. 2.12. By comparing these figures, it is fairly easy to tell that the NPS resulted from sub-images of different sizes share a common shape. So if the NPS is smooth in its nature, it is more preferable to use a smaller sub-image size with zero-padding to obtain smoother spectra with high frequency resolution as well as small statistical variance in the spectra.

Since DQE curves were based on NPS, similar results of the improvement of frequency resolution from zero-padding and the different smoothness caused by different sub-image sizes can be observed in Fig. 2.13 $\sim$ 2.24.

2.5 Chapter conclusion

In this chapter the DQE formulae were re-derived with the help of DTFT and the discrete random process theory. This is different from the classic approach which treats the imaging process on an infinitely large continuous imaging plane and uses continuous Fourier Transform as the fundamental mathematical tool for the derivation.

By using DTFT, the discrete nature of the incident photon numbers, the output pixel values, and the discrete pixel index were fully utilized. In fact, it is due to the discreteness in both pixel index and input/output values that the imaging system is called "digital". One of the advantages of using DTFT is that now the well established FFT-based computational tools can be naturally adopted for the DQE calculation. Furthermore, the problems such as the finite size of images vs. the infinitely large imaging plane, and the justification of using zero padding to improve the frequency resolution of MTF and NPS can be understood and explained more easily using this derivation.

The derivation was presented in a way that some confusing aspects of the DQE methodology for digital imaging systems are clarified. The imaging system is confined to the image detection system, and the input and output are specified clearly, in order to clarify the physical meaning of the DQE measuring process. At the end of the derivation, it is shown that DQE should be interpreted as the ratio between the converted output NPS resulted from the input fluctuation (N_q') and the NPS of the total output fluctuation (N_p), or as the ratio between the output SNR and the input SNR, which are defined from the perspective of power spectrum density functions.

Based on the re-derived DQE theory, the effect of estimating NPS using limited amount of image data was analyzed. The frequency resolution was affected by both the cutting window used in the NPS calculation and the number of points of used

by DFT. An example experiment of DQE was provided to illustrate the application of the DQE method and the use of "zero-padding". At the end, the assumptions and conditions employed in this derivation of the DQE theory were summarized, and several methodological suggestions were made in an effort to guide the implementation of the DQE measurements.

CHAPTER 3

DQE in magnification imaging

3.1 Chapter introduction

Geometric magnification has been widely used in x-ray imaging to provide more spatial details. Much work has been done to study the effects of geometric magnification on image quality in angiography and mammography [45–47]. In the previous chapters the DQE theory for digital imaging systems is introduced, and in this chapter, the DQE methodology in magnification radiography will be discussed. The impact of geometric magnifications on DQE under constant SIDs is firstly investigated using the widely accepted DQE theory that is based on the continuous basis, and then is studied using the DQE theory for digital x-ray imaging introduced in Chapter 2. At the end of this chapter, experimental measurements are provided as a demonstration.

3.2 Derivation of DQE in magnification radiography with constant SID based on the widely accepted DQE theory

3.2.1 DQE at unity magnification

As discussed at the end of Section 2.3.3, the widely accepted 1D DQE formula (at unit magnification) can be calculated as

$$DQE(f) = \frac{LAS^2 \cdot MTF(f)^2}{NPS(f) \cdot \Phi}, \tag{3.1}$$

where LAS is the mean pixel value of the output image that corresponds to the average number of photons per unit area Φ. MTF(f) and NPS(f) are the modulation transfer function and noise power spectrum, respectively.

3.2.2 DQE with Geometric Magnification Imaging

In magnification imaging with constant SID, we can imagine a virtual detector plane located just underneath the object plane (Fig. 3.1). Then the effect of magnification can be seen as the shrinking of pixel pitch from the actual detector plane to the virtual detector plane, which means the effective pixel size reduces from Δx_o to $\Delta x_o/M$, where "o" is for the original, actual detector plane and "m" is for the virtual detector plane from the magnification. Similarly, the size of the imaging field of the virtual detector is M times smaller on each dimension than that of the actual detector.

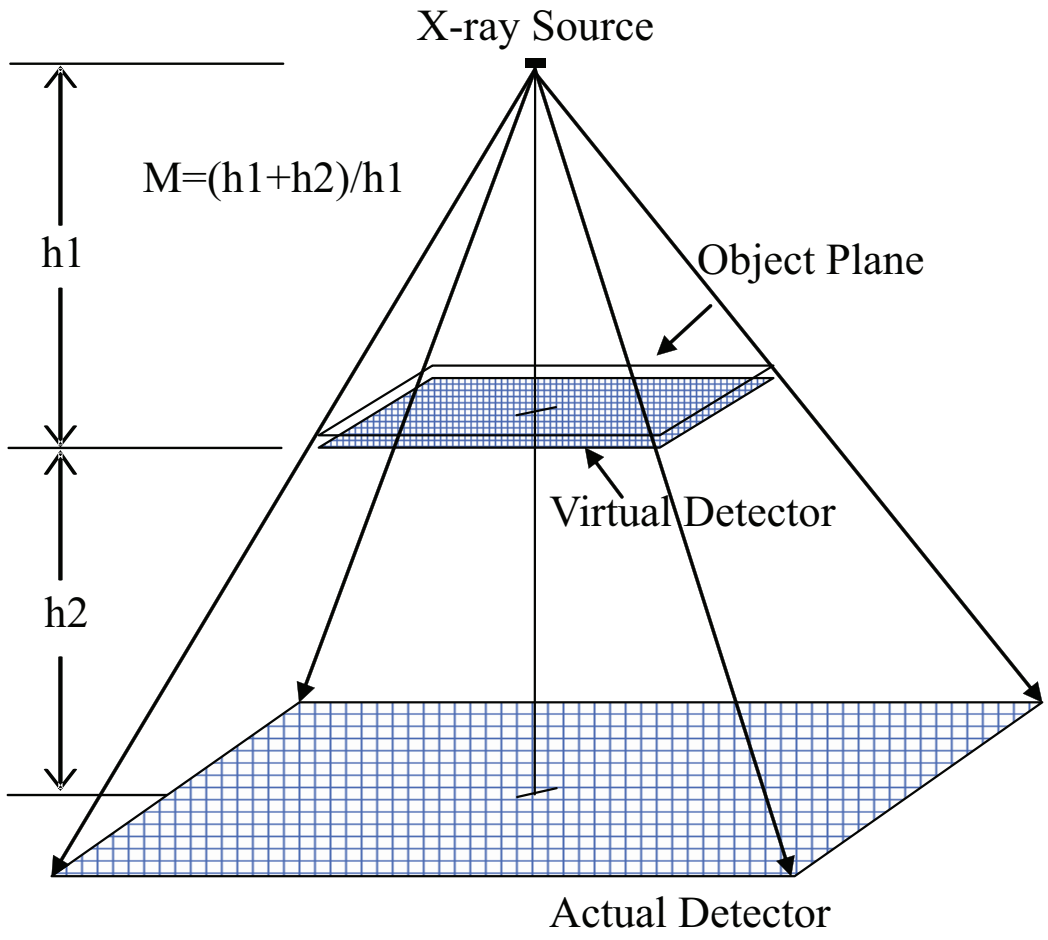

Figure 3.1: Schematic of the imaging system under magnification with constant SID. The virtual detector plane is closely underneath the object plane. Magnification factor M = (h1+h2)/h1.

In the following part of this section, the relation of each quantity in the DQE formula in magnification imaging with their counterparts at regular imaging with unit magnification (Eq. (3.1)) is derived.

LAS under magnification

LAS is the large area signal which is calculated by averaging the pixel values of the image of a uniform beam:

$$LAS = \frac{1}{N_x N_y} \sum_{i=1}^{N_x} \sum_{j=1}^{N_y} \mathrm{I(i,j)}, \tag{3.2}$$

where N_x and N_y are the number of pixels in each dimension of the detector, and $I(i,j)$ is the image intensity at pixel (i,j).

If we keep the distance from the source to the actual detector (Fig 3.1) constant and change the magnification by moving the object plane, the solid angle subtended by each pixel is also constant. That is, the number of quanta intercepted remains unchanged. Therefore, the average pixel intensity of the virtual detector is independent of the magnification:

$$LAS_o^2 = LAS_m^2 = \left(\frac{1}{N_x N_y} \sum_{i=1}^{N_x} \sum_{j=1}^{N_y} \mathrm{I(i,j)} \right)^2, \tag{3.3}$$

where LAS_o is the large area signal of the actual detector, LAS_m is the large area signal of the virtual detector, and $I(i,j)$ is the image intensity (pixel value) at index (i,j) for both cases.

Φ under magnification

Φ in Eq. (3.1) is the mean number of incident photons per unit area, i.e., the photon fluence. Under the same x-ray exposure and with the same SID, the photon fluence at the virtual detector is M^2 times of that at the actual detector based on the inverse square law (Fig. 3.1):

$$\Phi_m = M^2 \cdot \Phi_o, \tag{3.4}$$

where Φ_o and Φ_m are the photon fluences at the actual detector and at the virtual detector respectively, and M is the magnification factor.

MTF under magnification

MTF(f) is affected by magnification primarily in the following two manners. The Since the Nyquist frequency is determined by the pixel pitch of an imaging system [48], when the actual detector is projected onto the virtual detector plane, the pixel pitch is reduced. Thus the Nyquist frequency of the virtual detector will be higher than that of the actual detector and is related to the latter as:

$$f'_{Nyquist} = \frac{1}{2 \cdot \Delta x_m} = \frac{1}{2 \cdot \frac{1}{M}\Delta x_o} = M \cdot f_{Nyquist}. \tag{3.5}$$

The other effect would be that a change in the source-to-object distance (SOD) would change the geometric unsharpness caused by the finite focal spot size. As demonstrated in literature [49, 50], the MTF of the entire imaging chain under magnification can be given by:

$$\mathrm{MTF_{total}(f')} = \mathrm{MTF_{focal}(f'\frac{M-1}{M})} \cdot \mathrm{MTF_{det}(\frac{f'}{M})}, \tag{3.6}$$

where $MTF_{total}(f')$ is the MTF of the entire imaging chain, MTF_{focal} is the MTF of the focal spot, MTF_{det} is the MTF of the detection system, M is the magnification factor, and f' is the spatial frequency of the virtual detector.

If the focal spot size of the x-ray source is small enough and the SOD is large enough, the geometric unsharpness can be neglected and therefore $MTF_{focal}(f) = 1$. Eq. (3.6) can then be reduced to:

$$\mathrm{MTF_m(f')} = \mathrm{MTF_o(\frac{f'}{M})}. \tag{3.7}$$

NPS(f) under magnification

The 2-D discrete $NPS(m,n)$ at unity magnification can be calculated from the following formula [12]:

$$\mathrm{NPS(m,n)} = \lim_{\mathrm{N_x}\Delta x, N_y \Delta x \to \infty} \frac{\Delta \mathrm{x} \cdot \Delta \mathrm{x}}{\mathrm{N_x} N_y} \left| DFT[I(i,j)] \right|^2, \tag{3.8}$$

where N_x and N_y are the number of pixels in the region of interest of the noise only image, Δx is the pixel pitch, $I(i,j)$ is the image intensity of the noise only image, and (m,n) is the index of the result of DFT (2D Discrete Fourier Transform).

The pixel pitch of the virtual detector is $1/M$ of the pixel pitch of the actual detector. If the exposure and the SID are the same, the NPS under a given magnification is $1/M^2$ of the NPS under unity magnification:

$$\begin{aligned} & NPS_m(m,n) \\ &= \lim_{\mathrm{N_x}\Delta x_m, N_y \Delta x_m \to \infty} \frac{\Delta \mathrm{x_m} \cdot \Delta \mathrm{x_m}}{N_\mathrm{x} N_y} \left| DFT[I(i,j)] \right|^2 \\ &= \lim_{\mathrm{N_x}\Delta x_m, N_y \Delta x_m \to \infty} \frac{\frac{\Delta \mathrm{x_o}}{M} \cdot \frac{\Delta \mathrm{x_o}}{M}}{N_\mathrm{x} N_y} \left| DFT[I(i,j)] \right|^2 \\ &= \tfrac{1}{M^2} \cdot NPS_o(m,n). \end{aligned} \tag{3.9}$$

Practically, the 2-D discrete $NPS(m,n)$ is a function of the index (m,n), and is needs to be mapped into $NPS(u,v)$, which is a function of spatial frequency based on the following formulas:

$$\begin{aligned} & u = m \cdot \Delta f = m \cdot \tfrac{1}{N_x \Delta x} = \tfrac{m}{N_x/2} \cdot \tfrac{1}{2\Delta x} = \tfrac{m}{N_x/2} \cdot f_{Nyquist}, \\ & v = \tfrac{n}{N_y/2} \cdot f_{Nyquist}, \end{aligned} \tag{3.10}$$

where Δf is the frequency interval in the sampled spatial frequency domain, $f_{Nyquist}$ is the Nyquist frequency mentioned in Eq. (3.5), and N_x and N_y are the number of pixels in the region of interest of the detector.

From Eq. (3.5) and (3.10), it can be derived that:

$$\begin{cases} u_m = M \cdot u_o \\ v_m = M \cdot v_o \end{cases} \tag{3.11}$$

Then the relationship between the NPS with and without magnification can be expressed as:

$$NPS_m(u,v) = \frac{1}{M^2} \cdot NPS_o(u/M, v/M). \tag{3.12}$$

Since we calculate the 1-D $NPS(f)$ using the 2-D $NPS(u,v)$ data along a certain direction (horizontal, vertical or circular) [12], this relationship between the NPS with and without magnification still holds for the 1D NPS:

$$NPS_m(f) = \frac{1}{M^2} \cdot NPS_o(f/M). \tag{3.13}$$

DQE(f) under magnification

Based on Eq. (3.3), (3.4), (3.7), and (3.13), and with constant SID, the relationship between the DQE under magnification and the DQE under unity magnification is derived under the assumption that the x-ray source is an ideal point source:

$$\begin{aligned} & DQE_m(f) \\ &= \frac{LAS_m^2 \cdot MTF_m(f)^2}{NPS_m(f) \cdot \Phi_m} \\ &= \frac{LAS_o^2 \cdot MTF_o(f/M)^2}{\frac{1}{M^2} NPS_o(f/M) \cdot M^2 \cdot \Phi_o} \\ &= DQE_o(f/M). \end{aligned} \tag{3.14}$$

In practice, considering the influence of the finite focal spot size on MTF at magnification, the $MTF_m(f)$ measured under magnification should be used in the

DQE under magnification:

$$\begin{aligned} & DQE_m(f) \\ &= \frac{LAS_m^2 \cdot MTF_m(f)^2}{NPS_m(f) \cdot \Phi_m} \\ &= \frac{LAS_o^2}{\frac{1}{M^2} NPS_o(f/M) \cdot \Phi_m} \cdot MTF_m(f)^2, \end{aligned} \tag{3.15}$$

where f is the spatial frequency ranging from 0 to $f'_{Nyquist} = M \cdot f_{Nyquist}$ as mentioned in Eq. (3.5), $MTF_m(f)$ is the MTF obtained directly under magnification using the reduced pixel pitch, and Φ_m is the input photon fluence measured at the object plane. It should also be noted that Φ_m in Eq. (3.15) can be replaced by $M^2 \cdot \Phi_o$ according to Eq. (3.4).

3.2.3 Derivation of DQE in magnification radiography based on the revisited DQE theory for digital x-ray imaging systems

Based on the DQE theory for digital x-ray imaging systems detailed in Chapter 2, the above analysis about DQE measurements under magnification can be derived more easily and clearly. As discussed in Section 2.2.1 and 2.3.3, q in the DQE for digital imaging systems is defined as the average number of photons received per pixel, instead of per unit area. Also, according to Eq. (2.24), the calculation of NPS is independent of the pixel size Δx. Further, as discussed in Section 2.3.2, the frequencies (u, v, f) used in Eq. (2.14) and (2.15) are normalized frequencies whose values are independent of the pixel size Δx.

As discussed in Section 3.2.2, by imagining the virtual detector plane located just underneath the object plane (Fig. 3.1), the effect of magnification can be seen as the shrinking of pixel pitch from the actual detector plane to the virtual detector plane, which means the pixel reduces from the original size Δx_o to a smaller size $\Delta x_m = \Delta x_o / M$. Therefore, for magnification imaging with constant SID, q does not change, as the solid angle subtended by each pixel is constant. If a point source

is assumed, MTF and NPS as the functions of the normalized frequencies, remains unchanged. As already discussed previously in Section 3.2.2, LAS also remain the same when magnification is applied under the same SID. As the values of the four constituting parts of DQE remain unchanged, the value of DQE for digital x-ray imaging system, as a function of the normalized frequencies, remain unchanged.

The major effect of the magnification is that the effective pixel size reduces from the original value Δx_o to a smaller value $\Delta x_o/M$. As discussed in Section 2.3.2, the normalized frequencies are calculated by normalizing the analogue spatial frequency to the sampling frequency ($F_s = 2F_{Nyquist}1/\Delta x$). And the effective sampling frequency are increased by a factor of M times as the effective pixel sizes are reduced to $1/M$ of the actual pixel size Δx, as stated in Eq. (3.11). Therefore, when interpreting the MTF, NPS and DQE spectra for their physical meanings, the analogue spatial frequencies corresponding to the continuous normalized spatial frequencies (u, v) range from $-F_{m,Nyquist}$ to $F_{m,Nyquist}$ ($F_{m,Nyquist} = 1/(2\Delta x_m) = M \cdot 1/(2\Delta x_m) = M \cdot F_{o,Nyquist}$), which is equivalent to the conclusion in Eq. (3.14).

3.3 Experimental results based on the theory of DQE at magnification

The system used in this study is an x-ray specimen radiography system (MX-20, Faxitron X-Ray Corporation, Illinois). A tungsten target is used in the x-ray tube which emits x-ray beam that then passes through a 0.25 mm beryllium window. The x-ray system was operated at 0.3 mA, 26 kVp constantly in this research. The source-to-object distance (SOD) can be adjusted by placing the object on different shelf positions, but the SID is fixed as 572 mm. The detector in this system consists of two CCD arrays abutted together (KAF-1001E, Eastman-Kodak, New York). Each CCD had a 24.5 mm x 24.5 mm photoactive area with 1024x1024 pixels; therefore

the pixel pitch was 24 μm. An optical fiber taper was used to couple the CCDs to a Min-R scintillating screen (Eastman-Kodak, New York).

The DQE measurement was taken under 26 kVp, 0.3 mA, and 3s of exposure time. In the measurement of MTF, a 10 μm wide slit camera (IIE GmbH, Aachen, Germany) was used to collimate the x-ray beam into a line input in order to obtain Line Spread Functions [39]. NPS was measured by analyzing the images from a series of uniform incident radiation [12]. DQE was calculated by Eq. (3.15), in which the $MTF_m(f)$ obtained under magnification was used instead of $MTF_o(f)$ obtained under unity magnification. Then the index of the DQE dataset was re-mapped into the expanded spatial frequency by:

$$f' = n \cdot \Delta f' = \frac{n}{(N/2)} \cdot f'_{Nyquist} = \frac{n}{(N/2)} \cdot (M \cdot f_{Nyquist}), \tag{3.16}$$

where n is the index of data, N is the number of data points in the DQE dataset, Δx_m is the pixel pitch of the virtual detector, $f'_{Nyquist}$ is the Nyquist frequency calculated from the pixel pitch of the virtual detector, and $f_{Nyquist}$ is the Nyquist frequency calculated from the pixel pitch of the actual detector.

The MTF curves shown in Fig. 3.2 and 3.3 were acquired at 26 kVp, 0.3 mA, and 3s of exposure time, with magnifications ranging from 1X to 5X. The slit camera method [39] was adopted in the measurement of the MTF, and a $10 - \mu m$ wide slit camera (IIE GmbH, Aachen, Germany) was employed in the measurement.

It can be seen from Fig. 3.2 and 3.3 that the difference in MTF values at M = 4 and M = 5 is small. This could be due to the fact that the width of the slit camera used in this research was $10 - \mu m$, which is still rather wide to form the line input for the magnification imaging, and due to the increased geometric unsharpness introduced by the finite focal spot size and large magnification.

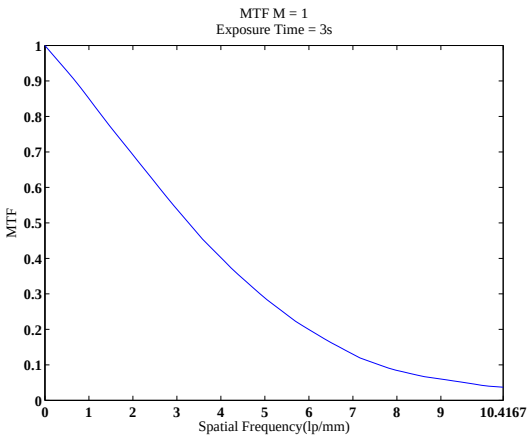

(a) M=1

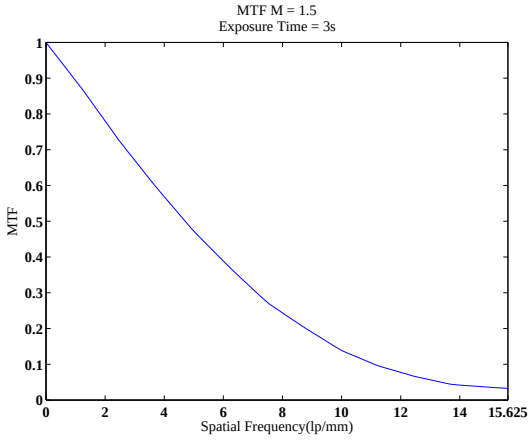

(b) M=1.5

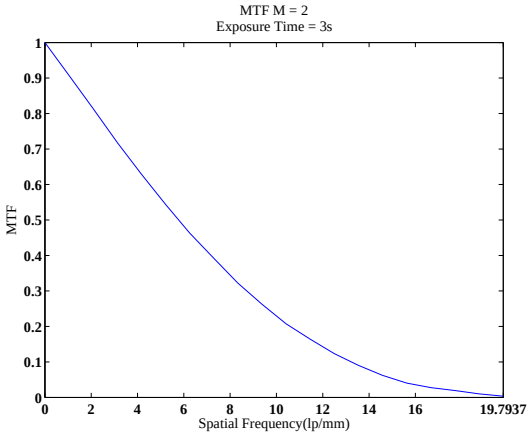

(c) M=2

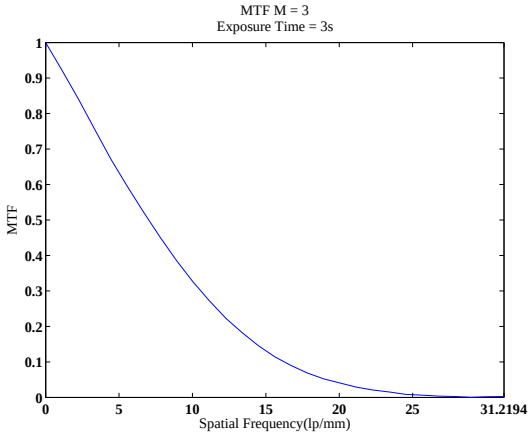

(d) M=3

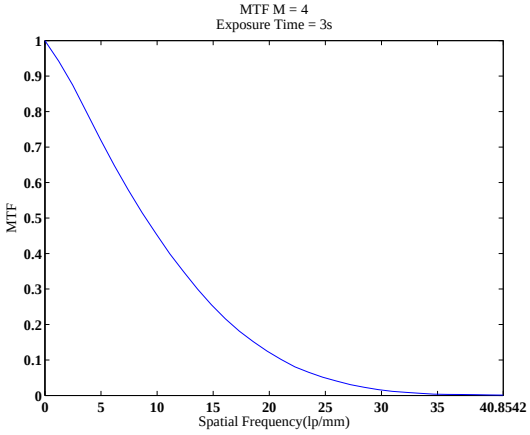

(e) M=4

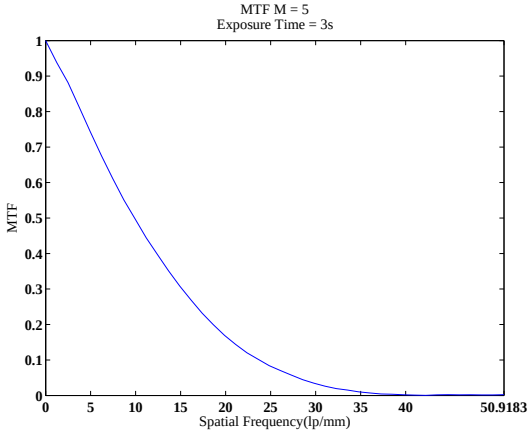

(f) M=5

Figure 3.2: MTF measured at 26 kVp, 0.3 mA, and 3s of exposure time, with magnifications of 1, 1.5, 2, 3, 4, and 5; each MTF curve was presented as an individual plot.

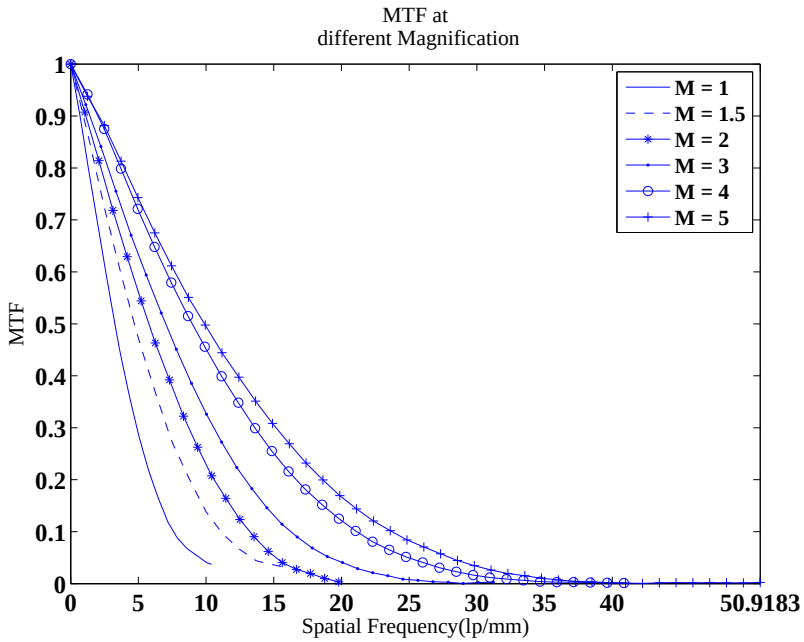

Figure 3.3: MTF measured at 26 kVp, 0.3 mA, and 3s of exposure time, with magnifications of 1, 1.5, 2, 3, 4, and 5; all MTF curves were plotted together to compare.

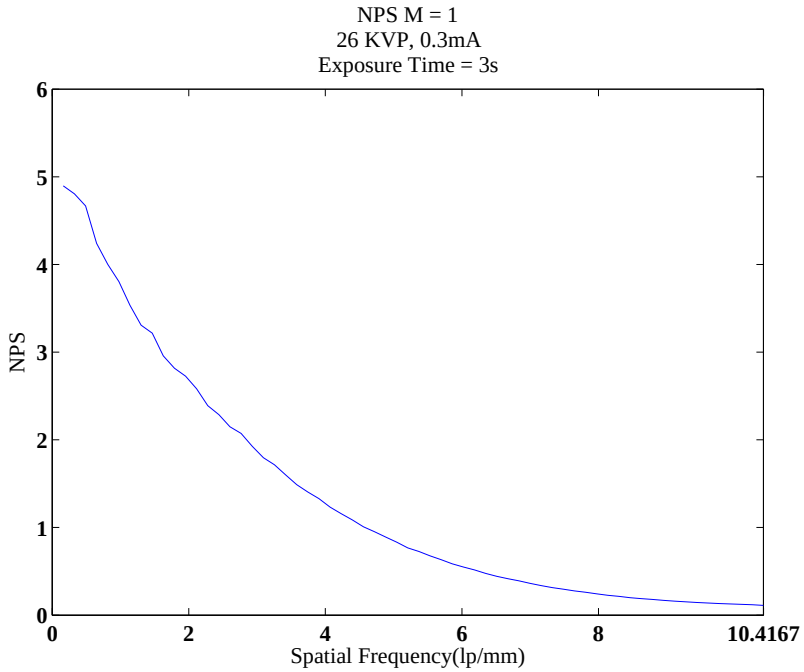

Figure 3.4: NPS used in the calculation of DQE in this study: measured at 26kVp, 0.3 mA, 3s of exposure time, M=1.

The NPS was measured by the analysis of a series of images of uniform incident radiation [12] at M = 1, 26 kVp, 0.3 mA and exposure time = 3s. The resulting curve is shown in Fig. 3.4.

The DQE curves shown in Fig. 3.5 and 3.6 were obtained according to Eq. (3.15), with the dataset of MTF and NPS (illustrated in Fig. 3.2, 3.3, and 3.4, as well as with the input signal to noise ratio N, which was calculated by multiplying the input exposure at the perspective object plane and the photon fluence per mR, which was measured as 8.7128*103 photon/(mm2*mR) in this study, following the method and procedures in [32, 51, 52].

It should be noticed that the values of the DQE at zero frequency theoretically should be equal because MTF at zero frequency is normalized to 1 and the other quantities in Eq. (3.15) are the same even under different magnifications (Fig. 3.5 and 3.6). However, it can be observed that there is some variation in the DQE at zero frequency, which is due to measurement error in the exposure level at different magnification.

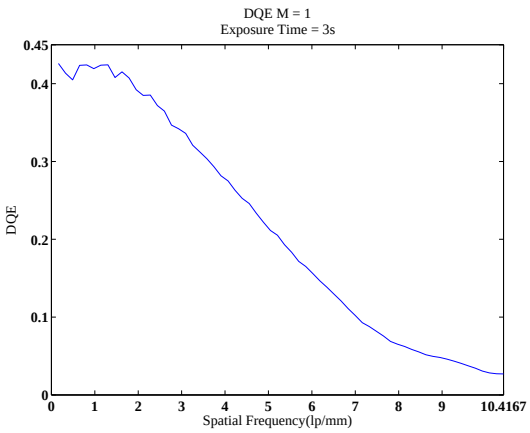

(a) M=1

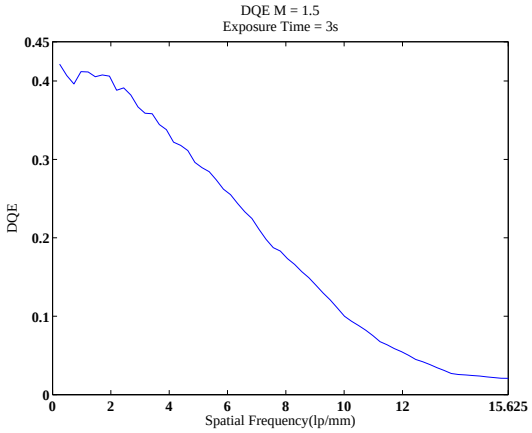

(b) M=1.5

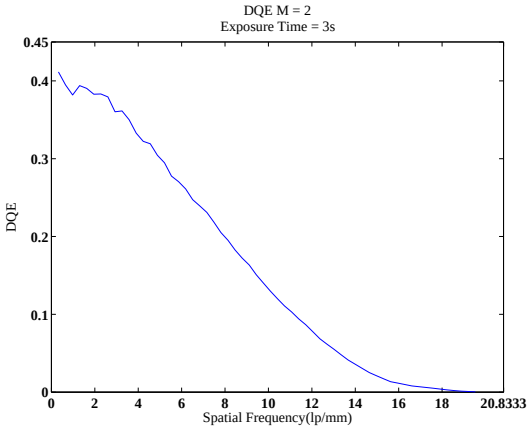

(c) M=2

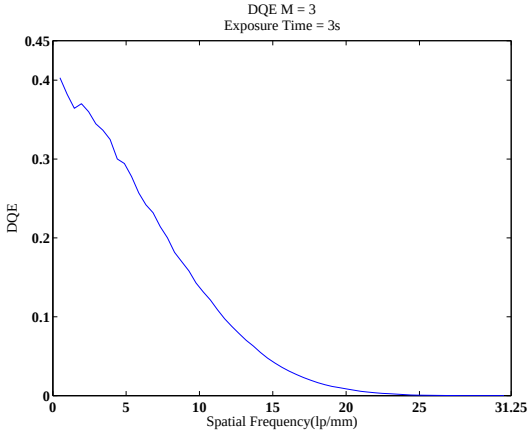

(d) M=3

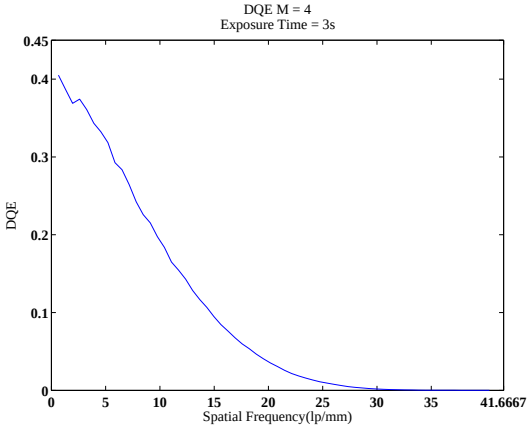

(e) M=4

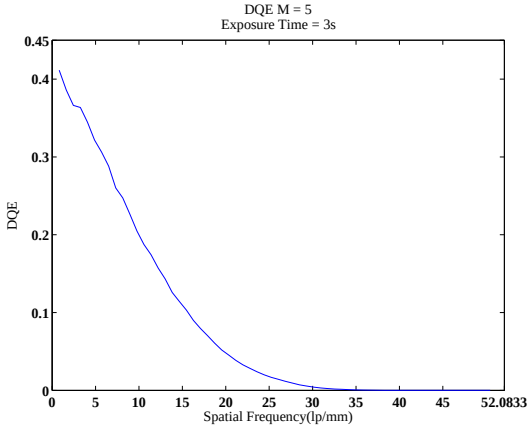

(f) M=5

Figure 3.5: DQE measured at 26 kVp, 0.3 mA, and 3s of exposure time, with magnifications of 1, 1.5, 2, 3, 4, and 5; each DQE curve was presented as an individual plot.

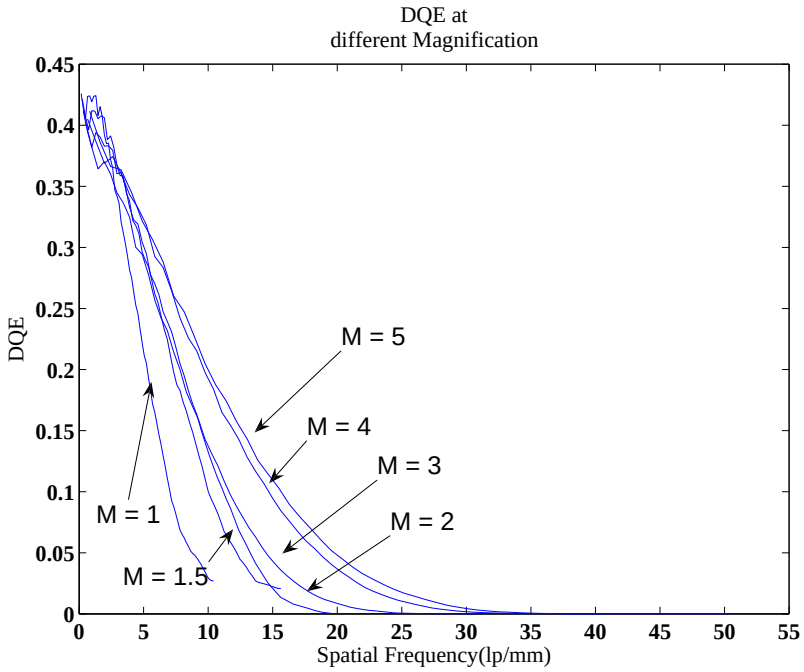

Figure 3.6: DQE measured at 26 kVp, 0.3 mA, and 3s of exposure time, with magnifications of 1, 1.5, 2, 3, 4, and 5; all DQE curves were plotted together to compare and contrast.

3.4 Chapter Conclusion

In this chapter, the DQE method in magnification x-ray imaging was investigated. The derivation was first conducted based on the traditional, widely accepted DQE theory, and then verified by the DQE theory for digital imaging systems introduced in Chapter 2.

From the traditional DQE point of view, theoretical analysis and experimental results indicate that the low frequency DQE values under different geometric magnifications are equal under the same x-ray exposure and the same source-to-detector distance. At a given magnification M and with constant SID, the input x-ray photon fluence is increased by M^2 times due to the inverse square law; and the noise power spectrum is reduced by M^2 times due to the reduction of the effective pixel size of

the detectors. From the point of DQE for digital x-ray imaging system, the number of photons per pixel q and LAS are unchanged when magnification is introduced; MTF, NPS, and DQE are functions of the normalized spatial frequencies and therefore their values are not affected by the reduction of the effective pixel size introduced by magnification. Therefore, as compared to the unity magnification case, the variation in the $DQE(f)$ curve under geometric magnification is primarily affected by the MTF curves and the increased effective sampling frequency. At the end, DQE under magnification of X1, X1.5, X2, X3, X4 and X5 under a constant SID were measured according to the theory introduced in this chapter. Part of the content in this chapter was published in [27].

CHAPTER 4

Determination of the x-ray photon fluence

4.1 Chapter introduction

As introduced in Chapter 2 and 3, the photon fluence plays an important role in the determination of DQE. Besides their applications in DQE, the measurements of the spectral composition and the photon fluence of incident x-ray beam is also of significant importance in many areas of diagnostic radiography, such as control of beam quality and study of patient dose [32, 51–57].

The photon fluence is defined as the number of x-ray photons received per unit area on a plane of interest, and in our approach the photon fluence is estimated experimentally through the measurement of incident x-ray spectral composition and the exposure level at the plane of interest. X-ray spectral composition in diagnostic radiography depends upon the tube potential, the target material, the generator waveform, and the total filtration in the x-ray beam [6]. The methods to determine the x-ray spectral composition include spectral modeling based on the exposure techniques and beam filtration [51, 55, 58], as well as direct spectroscopic measurements using various detectors, including High Purity Germanium (HPGe) detectors [54, 59–61], CdZnTe detectors [60, 61] and CdTe detectors [62, 63]. As compared to spectral modeling, the direct spectroscopic approach is able to offer better sensitivity to changes in experimental conditions, as well as better flexibility of the experiments as the measurements are not merely restricted to the standard exposure conditions.

In this chapter, the theory behind the estimation of photon fluence through the measurements of spectral composition and exposure levels is discussed first. Then the

uncertainty in the photon fluence from the energy calibration process, which converts the channel numbers in the raw spectral data into the energy levels, is investigated. To demonstrate the methods reported in this chapter, the photon fluence of a 40 kV, 0.5mA, 25μm-Rh filtered beam from a Mo-target tube at the SID of 183 cm (6 ft) was calculated with different energy calibrations. To obtain multiple channel-energy pairs for the calibration, we applied a new technique that utilizes the peaks in the secondary fluorescent x-ray from different filters placed in the primary beam. Six characteristic peaks, including Cu $K_{\alpha 1}$, Cu $K_{\beta 1}$, Pb $L_{\alpha 1}$, Pb $L_{\beta 1}$, Mo $K_{\alpha 1}$, and Mo $K_{\beta 1}$, were used in the comparison.

4.2 Determining photon fluence of an x-ray exposure from its spectrum and exposure level

Photon fluence (Φ) of the incident x-ray can be determined from the corresponding exposure level and spectral composition. In order to illustrate this method, the derivation of the calculation of Φ is first presented. It is helpful to list the definitions and units of several physical quantities that are involved in the derivation [64]:

- Photon fluence: $\Phi = \frac{Photon\ Number}{Area}(1/cm^2)$.
- Energy fluence: $\Psi = \Phi \cdot E = \frac{Photon\ Number}{Area} \cdot \frac{Energy}{Photon}$ (unit: kev/cm^2), for monochromatic x-ray photon
- Exposure: amount of electrical charge (ΔQ) produced by the ionizing electromagnetic radiation per unit mass of air (Δm), $X = \frac{\Delta Q}{\Delta m}$ (unit: milliroentgen, $1mR = 2.58 \times 10^{-7} C/kg$)
- Absorbed dose: the energy (ΔE) deposited by ionizing radiation per unit mass of material (Δm), $D = \frac{\Delta E}{\Delta m}$ (unit: keV/g)

The absorbed dose in air (D) resulting from an x-ray with exposure level (X) can be calculated as the energy needed to release the amount of electrons that forms X:

$$\begin{aligned} D &= \frac{X \cdot 2.58 \times 10^{-7}\,(C/kg)}{1.6 \times 10^{-19}\,(C/e)} \times 34(eV/e) \\ &= 5.4825 \times 10^{13} X\,(eV/kg) \\ &= 5.4825 \times 10^{7} X\,(keV/g). \end{aligned} \tag{4.1}$$

In the above equation, $X \cdot 2.58 \times 10^{-7}$ is the amount of charge per unit mass of air that corresponds to the exposure level X (in mR); $1.6 \times 10^{-19}\,C/e$ is the amount of charge of 1 electron; $34eV$ is the average energy needed to release 1 electron from air [64].

With a polychromatic x-ray beam, the total absorbed dose in air is the sum of the absorbed dose at each energy level of the radiation:

$$D = \sum_{E} D(E) \tag{4.2}$$

The absorbed dose in air at a certain energy level of the radiation equals to the product of the mass energy absorption coefficient (MEAC) of air $\left(\frac{\mu_{en}}{\rho}\right)_E$ and the energy fluence at that energy level $\Psi(E)$ [64]:

$$\begin{aligned} D(E) &= \left(\frac{\mu_{en}}{\rho}\right)_E \cdot \Psi(E) \\ &= \left(\frac{\mu_{en}}{\rho}\right)_E \cdot \Phi(E) \cdot E \end{aligned} \tag{4.3}$$

From Eq. (4.1), (4.2), and (4.3), the exposure X can be calculated as a function of the MEAC of air $\left(\frac{\mu_{en}}{\rho}\right)_E$, the energy level E, and the photon fluence at each energy level $\Phi(E)$:

$$\sum_{E} \left(\frac{\mu_{en}}{\rho}\right)_E \cdot \Phi(E) \cdot E = 5.4825 \times 10^{7} X, \tag{4.4}$$

and

$$X = \frac{\sum\limits_{E} \left(\frac{\mu_{en}}{\rho}\right)_E \cdot \Phi(E) \cdot E}{5.4825 \times 10^7}, \tag{4.5}$$

where the units of measurement are as follows: mR for X, cm^2/g for $\left(\frac{\mu_{en}}{\rho}\right)_E$, keV for E, and $1/cm^2$ for $\Phi(E)$.

Similar to the absorbed dose in air, the total photon fluence Φ is the sum of the photon fluence at each energy level of the radiation:

$$\Phi = \sum_{E} \Phi(E). \tag{4.6}$$

From Eq. (4.5) and (4.6), the photon fluence per unit exposure (F) can then be calculated as follows:

$$\begin{aligned}
F &= \frac{\Phi}{X} \\
&= \frac{\sum\limits_{E} \Phi(E)}{X} \\
&= \frac{\sum\limits_{E} \Phi(E)}{\frac{\sum\limits_{E} \left(\frac{\mu_{en}}{\rho}\right)_E \cdot \Phi(E) \cdot E}{5.4825 \times 10^7}} \\
&= \frac{5.4825 \times 10^7}{\sum\limits_{E} \left(\frac{\mu_{en}}{\rho}\right)_E \cdot [\Phi(E) / \sum\limits_{E} \Phi(E)] \cdot E} \\
&= \frac{5.4825 \times 10^7}{\sum\limits_{E} \left(\frac{\mu_{en}}{\rho}\right)_E \cdot \Phi_N(E) \cdot E} \, (1/(cm^2 \cdot mR)) \\
&= \frac{5.4825 \times 10^5}{\sum\limits_{E} \left(\frac{\mu_{en}}{\rho}\right)_E \cdot \Phi_N(E) \cdot E} \, (1/(mm^2 \cdot mR)),
\end{aligned} \tag{4.7}$$

where the unit of measurement for X is mR; for $\left(\frac{\mu_{en}}{\rho}\right)_E$ is cm^2/g; for E is keV, and for $\Phi(E)$ is $1/cm^2$. Since the spectrum of the incident x-ray is measured as the counts of photons at different energy channels, $\Phi_N(E) = \Phi(E) / \sum\limits_{E} \Phi(E)$ is the measured spectrum normalized by the total number of photons.

Now that the photon fluence per unit exposure has been determined, the photon fluence can simply be calculated as follows:

$$\Phi = F \cdot X, \tag{4.8}$$

where the units of measurement are as follows: mR for X, $(1/(cm^2 \cdot mR))$ or $(1/(mm^2 \cdot mR))$ for F, and either $1/cm^2$ or $1/mm^2$ for Φ, depending on the unit of F.

4.3 Energy calibration process and its uncertainty

In spectroscopic measurements, a spectrometer groups the counts of the detected x-ray photons into many channels, and generates the spectral data as the number of photons for each channel. Since the raw data of x-ray spectra are the photon counts at each channel, energy calibration is needed to convert the channel numbers into the energy levels to generate more analyzable data. Typically, a linear relationship between the channel numbers and the energy levels is expected [62,65], and the energy calibration requires at least two pairs of corresponding channel numbers and energy values (keV) to establish the linear relationship [65]. Since the linear relationship is estimated based on a limited number of channel-energy pairs, the estimation itself includes uncertainty. One illustration of this uncertainty is that a regression line determined from a set of channel-energy pairs can differ from the regression line determined from another set of channel-energy pairs: as can be seen in Fig. 4.1, the regression line determined from the lower, the middle, and the upper 2 channel-energy pairs are all different from the regression line determined from all 6 channel-energy pairs.

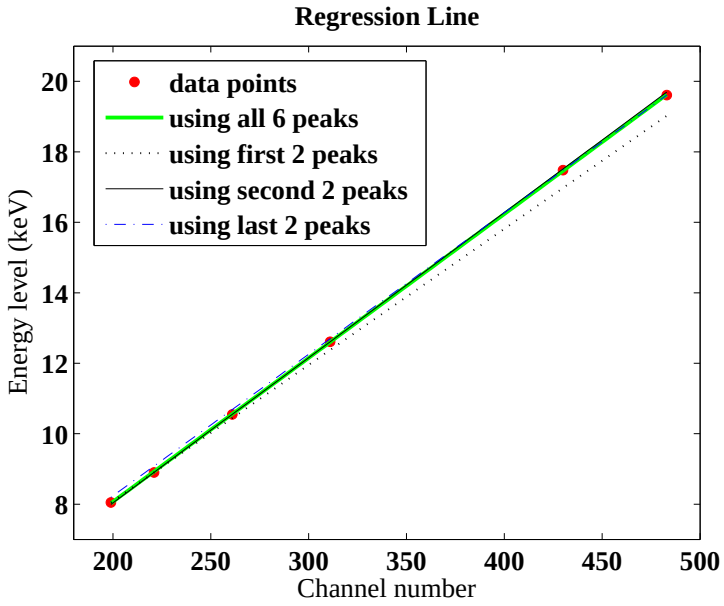

Figure 4.1: Illustration of the uncertainty in the regression line.

The calibration includes two steps: firstly, to determine the linear relationship between the channel numbers and the photon energy levels based on linear regression [65,66], and secondly, to convert the channel numbers into energy levels or vise versa.

The regression line representing the linear relationship between the channel numbers and the energy levels has the following form:

$$C = B_0 + B_1 E, \tag{4.9}$$

where E is the energy level and C denotes the channel number.

The reason for choosing E as the abscissa is that linear regression analysis assumes that there is no uncertainty in the independent variable [65], which is a good approximate in x-ray spectroscopy because the energy of characteristic peaks are known. Following the "simple linear model" of linear regression [66] (also known as "normal regression" [67]), if a set of paired data (e_1, c_1), (e_2, c_2), ..., and (e_n, c_n) are used in the linear regression, e_i are considered as constants and c_i as values of the corresponding independent random variables C_i. The "simple linear model" assumes that

the conditional density of C_i for each fixed e_i is normal and has the same variance (σ^2). Therefore the maximum likelihood estimator (MLE) for the regression line is as follows [66, 67]:

$$\hat{B}_1 = \frac{n\sum_{i=1}^{n} e_i c_i - \left(\sum_{i=1}^{n} e_i\right)\left(\sum_{i=1}^{n} c_i\right)}{n\left(\sum_{i=1}^{n} e_i^2\right) - \left(\sum_{i=1}^{n} e_i\right)^2}, \tag{4.10}$$

$$\hat{B}_0 = \bar{c} - \hat{B}_1 \bar{e}, \tag{4.11}$$

where $\bar{B}_0$ and $\bar{B}_1$ are the MLE estimators for B_0 and B_1 in Eq. (4.9); $\bar{e}$ and $\bar{c}$ are the mean of e_i and c_i values from all the data points used in the above calculation.

The variance of the estimators $\hat{B}_0$ and $\hat{B}_1$ can be estimated as [66]:

$$\widehat{Var}(\hat{B}_1) = \frac{S^2}{\sum_{i=1}^{n} (e_i - \bar{x})^2}, \tag{4.12}$$

$$\widehat{Var}(\hat{B}_0) = S^2 \left[\frac{1}{n} + \frac{\bar{x}^2}{\sum_{i=1}^{n} (e_i - \bar{x})^2}\right], \tag{4.13}$$

where

$$S^2 = \frac{1}{n-2}\sum_{i=1}^{n} (c_i - \hat{B}_0 - \hat{B}_1 e_i)^2 \tag{4.14}$$

is the unbiased estimator for the variance (σ^2) of the random variables C_i.

With a finite number (n) of data points used to estimate B_0 and B_1, the two estimators $\hat{B}_0$ and $\hat{B}_1$ follows a Student's t distribution with a degree of freedom of $n-2$ [66], and the 95% confidence intervals (c.i.) of B_0 and B_1 are

$$95\%\ c.i.\ of\ B_1 = \left[\hat{B}_1 - t_{0.025,n-2} \cdot \sqrt{\widehat{Var}(\hat{B}_1)}, \hat{B}_1 + t_{0.025,n-2} \cdot \sqrt{\widehat{Var}(\hat{B}_1)}\right], \tag{4.15}$$

and

$$95\%\ c.i.\ of\ B_0 = \left[\hat{B}_0 - t_{0.025,n-2} \cdot \sqrt{\widehat{Var}(\hat{B}_0)}, \hat{B}_0 + t_{0.025,n-2} \cdot \sqrt{\widehat{Var}(\hat{B}_0)}\right], \quad (4.16)$$

where $t_{0.025,n-2}$ is the upper percentile of Student's t distribution with $n-2$ degrees of freedom.

After the regression line is determined, the second step of calibration can be conducted. The typical procedure of energy calibration is to convert the channel numbers in the raw spectral data into energy levels, which could produce more interpretable spectral results. However, from the uncertainty analysis point of view, if the spectra have both uncertainty in its x-values (the energy) and its y-values (spectral readings), it will very difficult to derive the uncertainty propagated from the spectral measurement to the following calculations such as photon fluence. To solve this difficulty, we left the spectrum measured in its raw form: the numbers of photons at each channel ($\Phi(C)$), rather than converting the channel numbers in the raw spectra into energy levels. Instead, we convert the MEAC of air used in Eq. (4.7) from a known, deterministic function of energy levels ($f(E) = \left(\frac{\mu_{en}}{\rho}\right)_E$) into a function of the channel numbers $g(C)$, which contains uncertainty in its abscissa due to the energy-to-channel conversion:

$$g(C) = f(E) = f(\frac{C}{B_1} - \frac{B_0}{B_1}), \quad (4.17)$$

where $f(E)$ and $g(C)$ represent the MEAC of air as the function of energy E and channel number C, respectively.

With the normalized spectra directly measured as the function of channel numbers $\Phi_N(C) = \Phi(C) / \sum_C \Phi(C)$, and the energy levels E converted to channel numbers as

$E = \frac{C}{B_1} - \frac{B_0}{B_1}$, F can be determined based on the channel numbers C ($C = 1, 2, ..., k$):

$$\begin{aligned} F &= \frac{5.4825 \times 10^5}{\sum_{C=1}^{k} g(C) \cdot \Phi_N(C) \cdot (\frac{C}{B_1} - \frac{B_0}{B_1})} \\ &= \frac{B_1 \cdot 5.4825 \times 10^5}{\sum_{C=1}^{k} g(C) \cdot \Phi_N(C) \cdot (C - B_0)} \, (1/(mm^2 \cdot mR)), \end{aligned} \tag{4.18}$$

where k is the number of channels in the measured spectrum.

According to the propagation of uncertainty theory specified by ISO [68] and ANSI/ASME [69], for each channel number $C = 1, ..., k$, the uncertainty of $g(C)$ propagated from the calibration process is:

$$\widehat{Var}(g(C)) = \left(\frac{\partial g(C)}{\partial B_1}\right)^2 \widehat{Var}(B_1) + \left(\frac{\partial g(C)}{\partial B_0}\right)^2 \widehat{Var}(B_0), \tag{4.19}$$

$$\begin{aligned} \frac{\partial g(C)}{\partial B_1} &= \frac{df(E)}{dE} \cdot \frac{\partial E}{\partial B_1} \\ &= \frac{df(E)}{dE} \cdot \frac{-E}{B_1}, \end{aligned} \tag{4.20}$$

$$\begin{aligned} \frac{\partial g(C)}{\partial B_0} &= \frac{df(E)}{dE} \cdot \frac{\partial E}{\partial B_0} \\ &= \frac{df(E)}{dE} \cdot \frac{-1}{B_1}, \end{aligned} \tag{4.21}$$

where for each channel $C = 1, ..., k$, E is its corresponding energy level; $\frac{df(E)}{dE}$ can be estimated as the slope of the MEAC curve ($f(E)$) of air at the energy E.

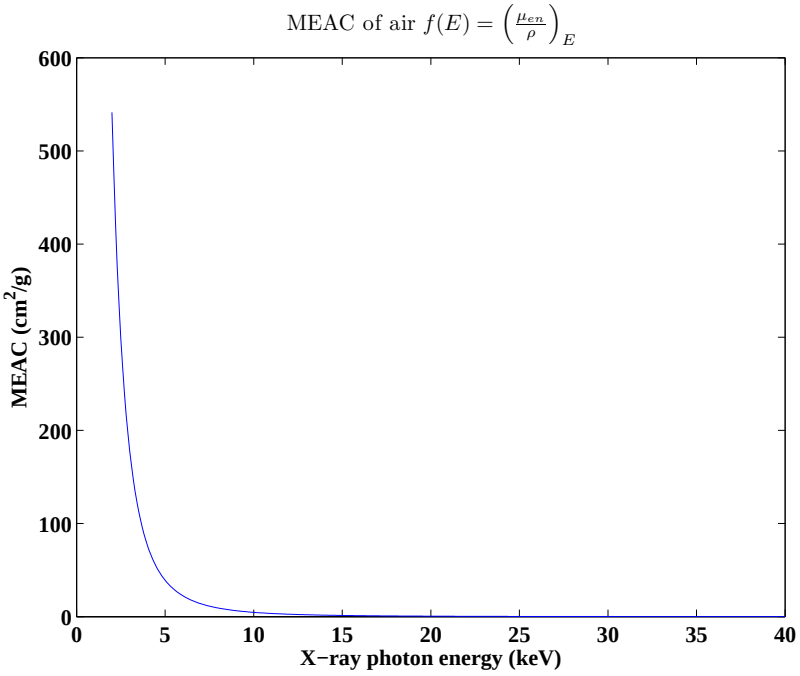

Figure 4.2: Mass Energy Absorption Coefficients (MEAC) of air.

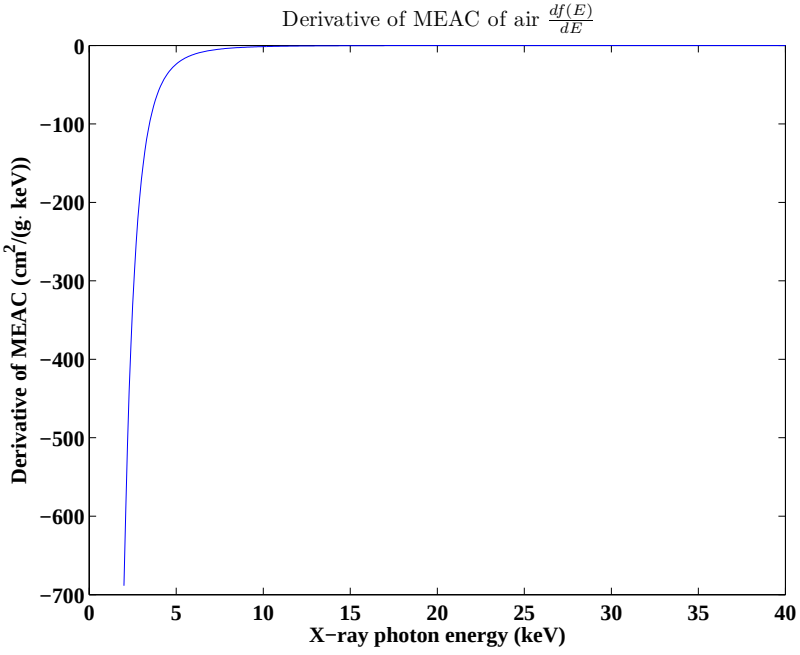

Figure 4.3: Derivative of the MEAC of air.

Based on Eq. (4.12), (4.13), (4.18), and (4.19), the uncertainty that propagates

from B_0, B_1 and $g(C)$ $(C = 1, 2, ..., k)$ into F can be calculated as:

$$\begin{aligned} \widehat{V}ar(\hat{F}) &= \left(\frac{\partial F}{\partial B_1}\right)^2 \cdot \widehat{V}ar(\hat{B}_1) \\ &+ \left(\frac{\partial F}{\partial B_0}\right)^2 \cdot \widehat{V}ar(\hat{B}_0) \\ &+ \sum_{C=1}^{k} \left\{ \left(\frac{\partial F}{\partial g(C)}\right)^2 \cdot \widehat{V}ar(g(C)) \right\}, \end{aligned} \tag{4.22}$$

where

$$\frac{\partial F}{\partial B_1} = \frac{5.4825 \times 10^5}{\sum_{C=1}^{k} g(C) \cdot \Phi_N(C) \cdot (C - B_0)}, \tag{4.23}$$

$$\frac{\partial F}{\partial B_0} = \frac{B_1 \cdot 5.4825 \times 10^5}{\left\{ \sum_{C=1}^{k} g(C) \cdot \Phi_N(C) \cdot (C - B_0) \right\}^2} \cdot \sum_{C=1}^{k} g(C) \cdot \Phi_N(C), \tag{4.24}$$

and

$$\frac{\partial F}{\partial g(C)} = \frac{-B_1 \cdot 5.4825 \times 10^5}{\left\{ \sum_{C=1}^{k} g(C) \cdot \Phi_N(C) \cdot (C - B_0) \right\}^2} \cdot \Phi_N(C) \cdot (C - B_0), \tag{4.25}$$

for each $C = 1, ..., k$.

And the uncertainty in Φ from the energy calibration process is therefore

$$\widehat{V}ar(\hat{\Phi}) = \left(\frac{\partial \Phi}{\partial F}\right)^2 \cdot \widehat{V}ar(\hat{F}) = X^2 \cdot \widehat{V}ar(\hat{F}), \tag{4.26}$$

where X is the measured exposure level at the point of interest.

4.4 The measurement of incident x-ray spectra

Under our experimental settings, x-ray spectra were measured with a spectrometer system which consists of a Cadmium Telluride (CdTe) detector (XR-100T-CdTe,

Amptek Inc., MA) and a multi-channel analyzer (MCA8000, Amptek Inc., MA). The spectrometer uses a wide band-gap, compound CdTe semiconductor as the detector element, with a CdTe crystal size of $3 \times 3 \times 1mm^3$. The internal components of the detector are cooled with a small thermoelectric that provides an approximately -50^oC temperature difference, in an effort to reduce the leakage current and improve the charge transport property [63]. In the energy range from 10 keV to 50 keV, the detector provides nearly 100% detection efficiency [70].

In the spectral measurement process, x-rays were generated from a micro-focus tube (UltraBright, Oxford Instruments, CA) which has a Molybdenum target and a $245\mu m$ thick Beryllium output window. The X-ray spectra were measured at a tube potential of 40 kVp and a tube current of 0.5 mA, with the additional filtration of a $25\mu m$ thick Rhodium filter, for a duration of 400s. The CdTe detector was aligned with the incident beam based on a dual laser alignment approach [42]. The alignment procedure will be discussed in Chapter 5. The experimental configuration is illustrated in Fig. 4.4.

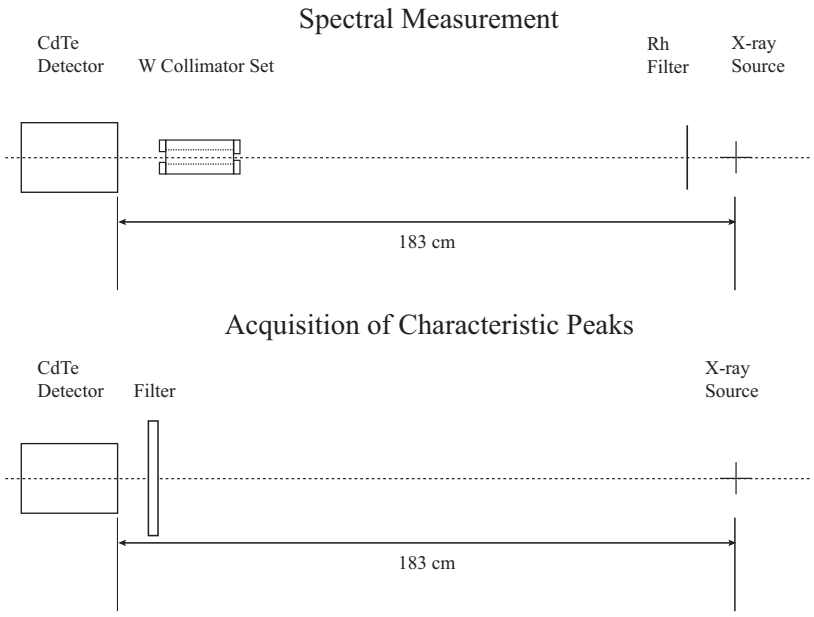

Figure 4.4: The experimental configuration for x-ray spectral measurement. The two tungsten collimators were separated by a brass cylinder with an opening diameter of 2-mm.

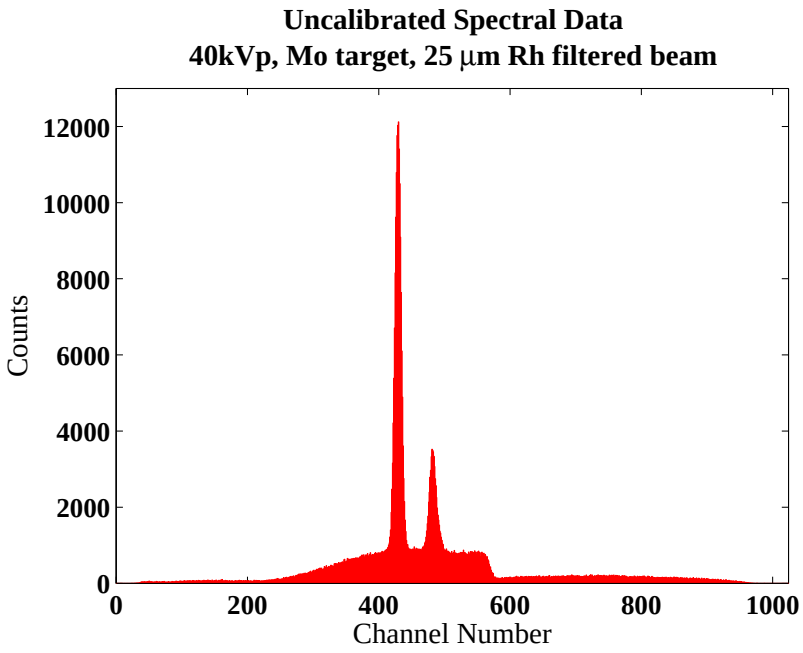

Figure 4.5: The raw spectrum obtained at 40 kVp, 0.5 mA, 400s, with Mo-target and $25\mu m$ Rhodium additional filtration.

4.5 Characteristic peaks for the energy calibration process

Although the calibration line is often determined based on the characteristic peaks from isotopic radiation [54, 59–63], isotopes are not always available for experimental setups. Using the characteristic peaks of the measured x-ray beam as the basis of energy calibration is therefore a practical alternative. However, due to the fact that the number of peaks in a diagnostic x-ray beam is small, significant uncertainty could thus be involved in the calibration process. In order to increase the number of characteristic peaks involved in the energy calibration process, we utilized the fluorescent x-rays resulting from the photoelectric effect between the primary x-ray and different collimator materials, including lead and copper. X-ray at the tube potential of 40kVp X-ray was utilized, and the $25\mu m$ Rhodium filtration was removed from the beam to obtain the K-characteristic peaks of the Molybdenum target. In

order to determine the channel-energy pair for the characteristic peaks of copper ($K_{\alpha 1}$, 8.05 keV and $K_{\beta 1}$, 8.90 keV) and lead ($L_{\alpha 1}$,10.55 keV and $L_{\beta 1}$, 12.61 keV), pure copper and lead foil were placed in front of the CdTe detector, respectively.

Table 4.1 shows the 6 channel-energy pairs used to determine the calibration line for energy calibration. Fig. 4.6, Fig. 4.7, and Fig. 4.8 show the spectra obtained for the Mo characteristic peaks, the Cu characteristic peaks, and the Pb characteristic peaks, respectively.

Table 4.1: The channel-energy pairs used in the energy calibration.

Peak	Channel Number	Energy Level
Cu $K_{\alpha 1}$	199	8.05
Cu $K_{\beta 1}$	221	8.90
Pb $L_{\alpha 1}$	261	10.55
Pb $L_{\beta 1}$	311	12.61
Mo $K_{\alpha 1}$	430	17.48
Mo $K_{\beta 1}$	483	19.61

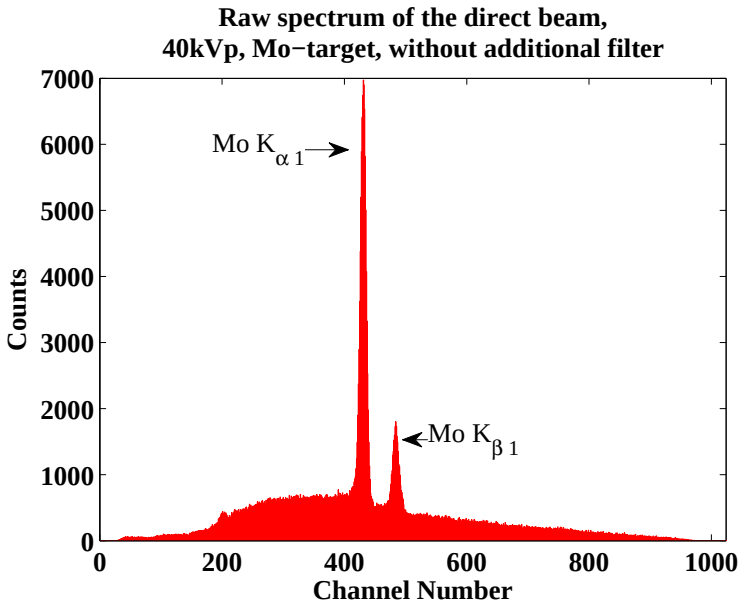

Figure 4.6: Characteristic peaks of Molybdenum.

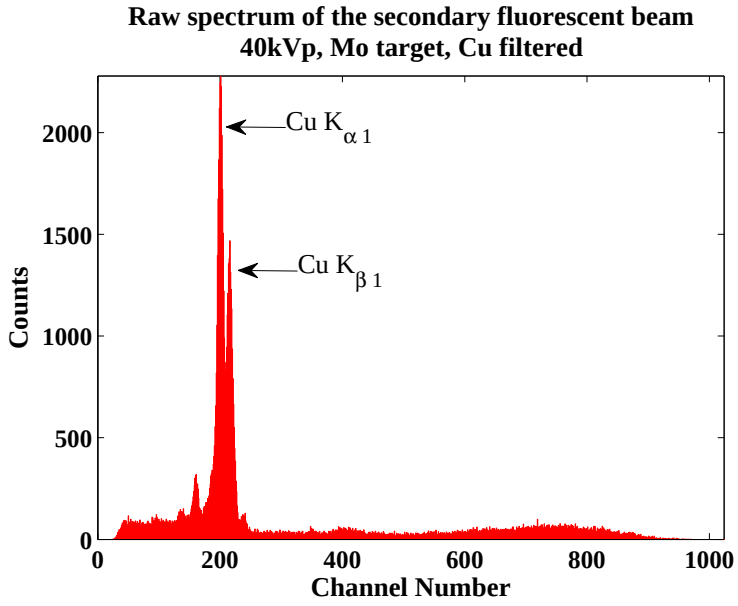

Figure 4.7: Characteristic peaks of copper.

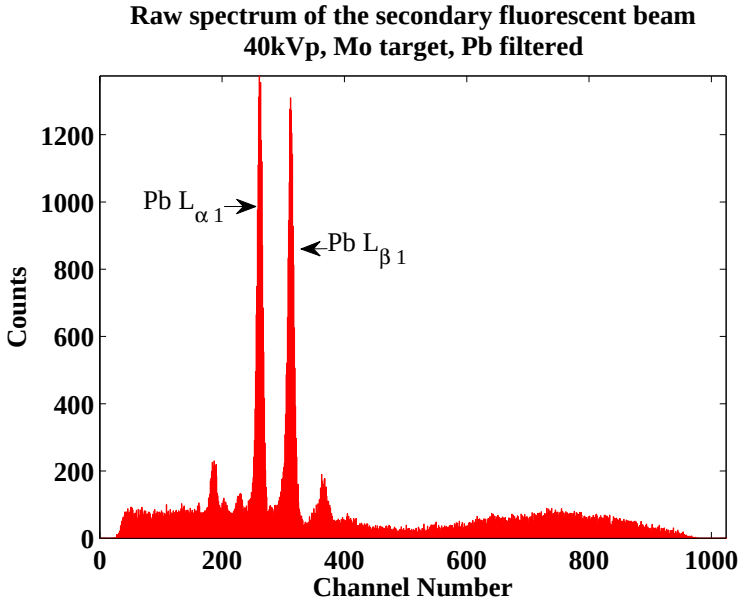

Figure 4.8: Characteristic peaks of lead.

4.6 Statistical results on the energy calibration

Based on the first 3 channel-energy pairs, the first 4 pairs, the first 5 pairs, and all the 6 peaks in Table 4.1, the statistics on the parameters B_0 and B_1 of the calibration line (Eq. (4.9)) can be obtained, and the results are shown in Table 4.2.

Table 4.2: The statistical information of the regression line estimated from different number of channel-energy pairs. 3 pairs: Cu $K_{\alpha 1}$, Cu $K_{\beta 1}$, and Pb $L_{\alpha 1}$. 4 pairs: Cu $K_{\alpha 1}$, Cu $K_{\beta 1}$, Pb $L_{\alpha 1}$, and Pb $L_{\beta 1}$. 5 pairs: Cu $K_{\alpha 1}$, Cu $K_{\beta 1}$, Pb $L_{\alpha 1}$, Pb $L_{\beta 1}$, and Mo $K_{\alpha 1}$. 6 pairs: all the data pairs listed in Table 4.1.

	3 pairs	4 pairs	5 pairs	6 pairs
B_1	24.72	24.48	24.43	24.49
B_0	0.36	2.50	2.96	2.43
$Var\{B_1\}$	0.169	0.033	0.005	0.003
$Var\{B_0\}$	14.37	3.43	0.71	0.48
95% c.i. of B_1	24.72±5.22	24.48 ± 0.78	24.43 ± 0.22	24.49 ± 0.14
95% c.i. of B_0	0.36 ± 48.16	2.50 ± 7.97	2.96 ± 2.68	2.43 ± 1.93

Using the estimated B_0 and B_1 based on all the six channel-energy pairs, the calibration can be applied to the raw spectrum in Fig. 4.5, and the results are shown in Fig. 4.9.

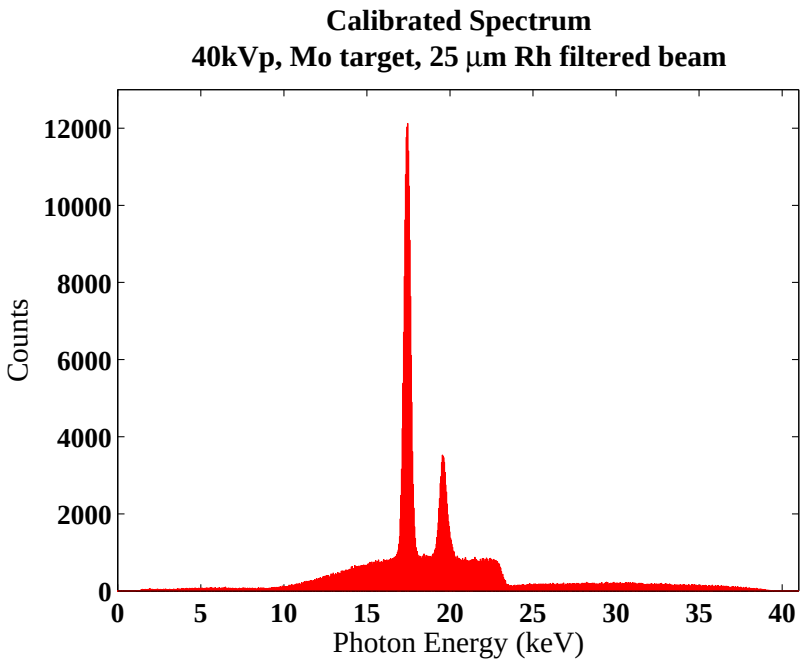

Figure 4.9: The calibrated spectrum obtained at 40 kVp, 0.5 mA, 400s, with Mo-target and 25μm Rhodium additional filtration. The energy calibration is based on all the six channel-energy pairs shown in Table 4.1.

In order to provide an intuitive illustration on the impact of the calibration uncertainty in the spectral measurement and the photon fluence calculation, the raw spectrum in Fig. 4.5 are calibrated using the estimated value, as well as the lower and upper boundary value of the 95% confidence interval of the parameters B_0 and B_1. The statistics on B_0 and B_1 based on 3 channel-energy pairs, 4 pairs, 5 pairs, and all the 6 pairs in Table 4.1 are compared in this manner, and the results are shown in Fig. 4.10, 4.11, 4.12, and 4.13.

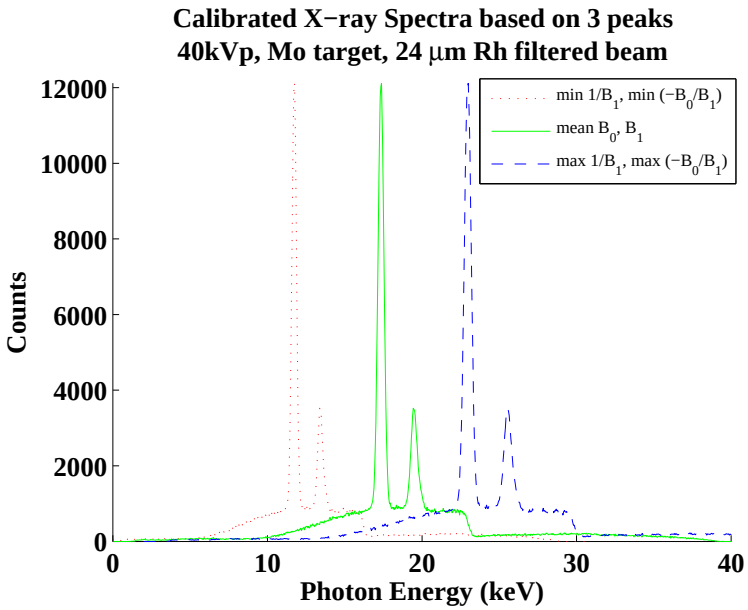

Figure 4.10: The calibrated spectra obtained at 40 kVp, 0.5 mA, 400s, with Mo-target and $25\mu m$ Rhodium additional filtration. The energy calibration is based on the estimated value, as well as the lower and upper boundary value of the 95% confidence interval of the parameters B_0 and B_1. The first 3 channel-energy pairs shown in Table 4.1 are used for the statistics.

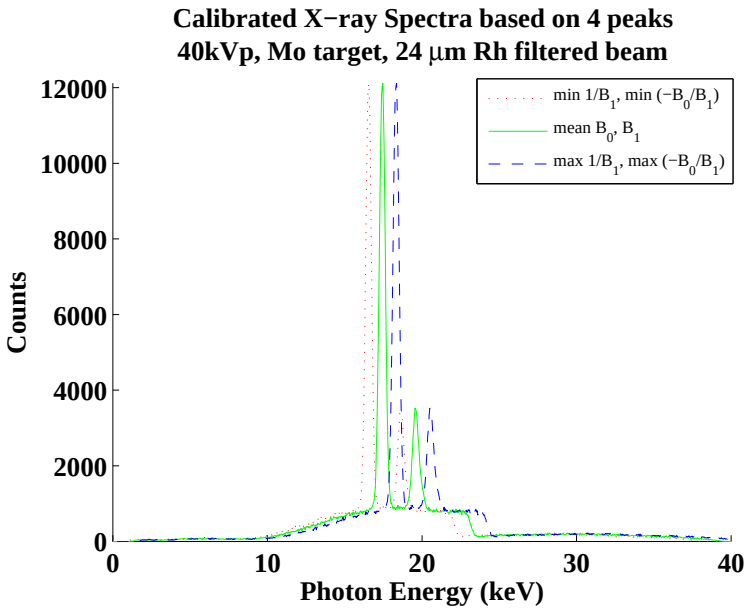

Figure 4.11: The calibrated spectra obtained at 40 kVp, 0.5 mA, 400s, with Mo-target and $25\mu m$ Rhodium additional filtration. The energy calibration is based on the estimated value, as well as the lower and upper boundary value of the 95% confidence interval of the parameters B_0 and B_1. The first 4 channel-energy pairs shown in Table 4.1 are used for the statistics.

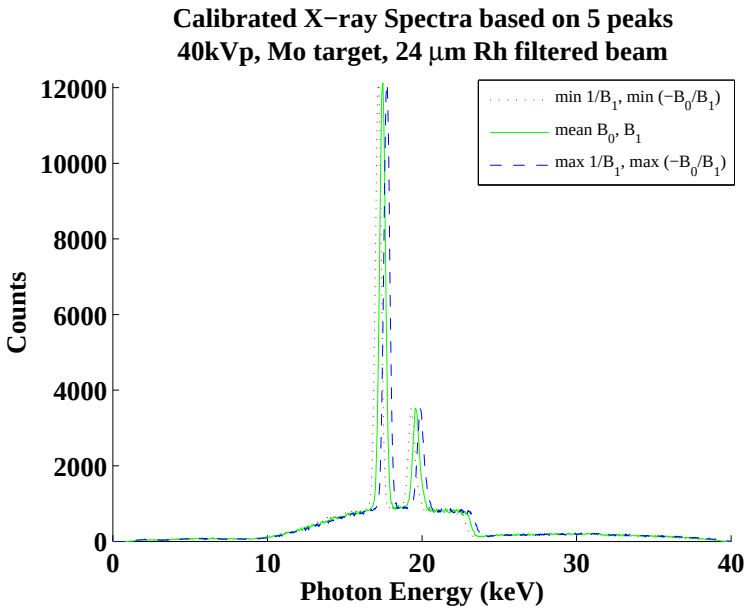

Figure 4.12: The calibrated spectra obtained at 40 kVp, 0.5 mA, 400s, with Mo-target and $25\mu m$ Rhodium additional filtration. The energy calibration is based on the estimated value, as well as the lower and upper boundary value of the 95% confidence interval of the parameters B_0 and B_1. The first 5 channel-energy pairs shown in Table 4.1 are used for the statistics.

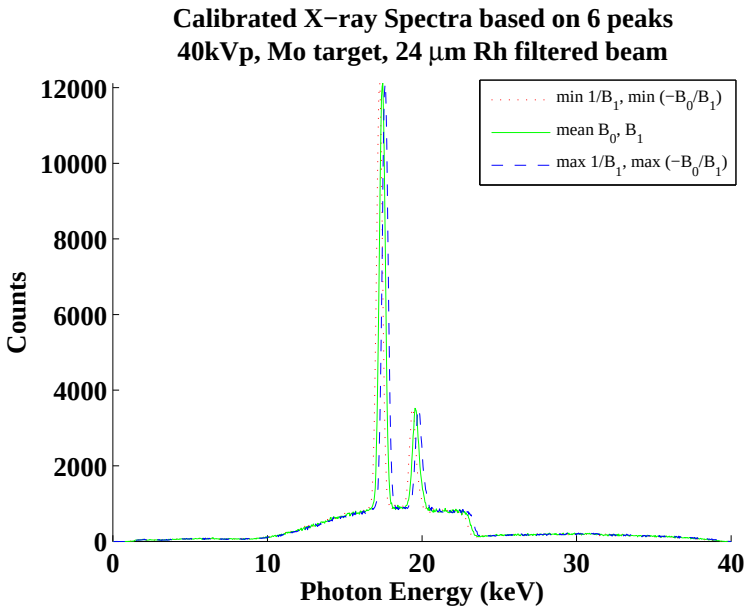

Figure 4.13: The calibrated spectra obtained at 40 kVp, 0.5 mA, 400s, with Mo-target and $25\mu m$ Rhodium additional filtration. The energy calibration is based on the estimated value, as well as the lower and upper boundary value of the 95% confidence interval of the parameters B_0 and B_1. All 6 channel-energy pairs shown in Table 4.1 are used for the statistics.

Based on these different calibration results, the fluence per unit exposure F can be calculated using Eq. (4.22), and the results are shown in Table 4.3.

Table 4.3: The statistical results of the photon fluence per unit exposure F estimated based on different number of channel-energy pairs. 3 pairs: Cu $K_{\alpha 1}$, Cu $K_{\beta 1}$, and Pb $L_{\alpha 1}$. 4 pairs: Cu $K_{\alpha 1}$, Cu $K_{\beta 1}$, Pb $L_{\alpha 1}$, and Pb $L_{\beta 1}$. 5 pairs: Cu $K_{\alpha 1}$, Cu $K_{\beta 1}$, Pb $L_{\alpha 1}$, Pb $L_{\beta 1}$, and Mo $K_{\alpha 1}$. 6 pairs: all the data pairs listed in Table 4.1.

	3 pairs	4 pairs	5 pairs	6 pairs
F_{min} $1/(mm^2 mR)$	18122	35635	38428	38748
$F_{estimated}$ $1/(mm^2 mR)$	39185	39557	39659	39559
F_{max} $1/(mm^2 mR)$	66963	43595	40869	40376

In one of our experiments, the exposure at a SID of 183 cm (6 ft) is measured as 16.28 mR. The estimated photon fluence Φ is shown in Table 4.4. To demonstrate the impact of the calibration uncertainty in the calculated photon fluence, the values in Table 4.4 are plotted in Fig. 4.14.

Table 4.4: The statistical results of the photon fluence Φ estimated based on different number of channel-energy pairs. 3 pairs: Cu $K_{\alpha 1}$, Cu $K_{\beta 1}$, and Pb $L_{\alpha 1}$. 4 pairs: Cu $K_{\alpha 1}$, Cu $K_{\beta 1}$, Pb $L_{\alpha 1}$, and Pb $L_{\beta 1}$. 5 pairs: Cu $K_{\alpha 1}$, Cu $K_{\beta 1}$, Pb $L_{\alpha 1}$, Pb $L_{\beta 1}$, and Mo $K_{\alpha 1}$. 6 pairs: all the data pairs listed in Table 4.1.

	3 pairs	4 pairs	5 pairs	6 pairs
Φ_{min} $1/(mm^2 mR)$	295026	580138	625608	630817
$\Phi_{estimated}$ $1/(mm^2 mR)$	637932	643988	645649	644021
Φ_{max} $1/(mm^2 mR)$	1090158	709727	665347	657321

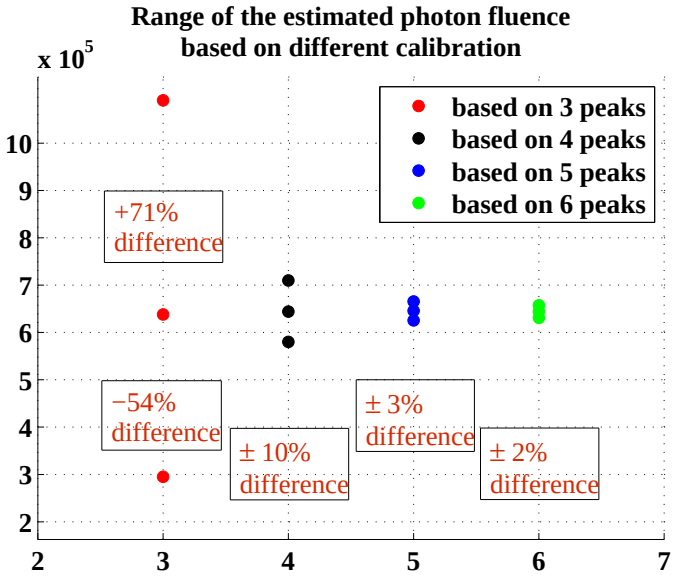

Figure 4.14: Illustration of the statistics of the photon fluence Φ for the 40 kVp, 0.5 mA, Mo-target and 25μm Rhodium filtered beam at the exposure of 16.28 mR. The energy calibration is based on the estimated value, as well as the lower and upper boundary value of the 95% confidence interval of the parameters B_0 and B_1.

4.7 Chapter conclusion

The photon fluence plays an important role in the determination of DQE. Besides that, the determination of the photon fluence and the spectral composition is also significantly important in many areas of diagnostic radiography, such as control of beam quality and study of patient dose. In this chapter, the method to estimate the photon fluence for an incident x-ray beam based on its spectral composition and the exposure level is discussed. After a detailed derivation of the method, the impact of the calibration uncertainty on the calculated photon fluence is analyzed mathematically. Experimental results based on a 40 kVp, 0.5 mA, and 25-μm-Rh-filtered beam from a Mo-target based x-ray tube is used to demonstrate the methods.

Several observations could be reached from the experimental results. Firstly, the level of uncertainty in the energy calibration can be reduced by increasing the number of channel-energy pairs used in the linear regression, as can be seen in Table 4.2. Secondly, the uncertainty in the regression can cause energy shifts in the calibrated spectra, as can be observed in Fig. 4.10, Fig. 4.11, Fig. 4.12, and Fig. 4.13. Thirdly, with the usage of the characteristic peaks from the secondary fluorescent x-ray caused by different filters (Cu and Pb in this study), as well as the characteristic peaks from the primary beam (Mo in this study), more channel-energy pairs can be easily obtained to reduce the calibration uncertainty, as can be seen in Table 4.3 and 4.4. Part of the content of this chapter was published in [52].

CHAPTER 5

A convenient alignment approach for x-ray imaging experiments based on laser positioning devices

5.1 Chapter introduction

The alignment between the radiation source, the subject, and the measuring and detecting devices is critical in x-ray imaging experiments, and has been investigated in subject positioning and portable radiography [71, 72], as well as in the measurements of modulation transfer function (MTF) [73, 74], focal spot size [75, 76], and x-ray spectra [76–79].

Several techniques for alignment using lasers and other methods have been devised and reported in literature, such as the combination of a laser projector and reflectors to indicate the correct relative position between the subject, the detector and the x-ray beam [71–73, 75], the combination of laser positioning and pinhole focal-spot radiography to provide precise alignment [74, 79], the use of a single laser that points to the focal spot position to help the alignment of x-ray spectrometer [78], and the use of multi-pinhole plate and telescope-based observation in determining the collimator position in spectral measurements [76].

In this chapter, a new alignment approach is reported, which differs from the other methods in that it provides two coinciding laser beams pointing toward and away from the x-ray source, instead of using only one laser pointing toward the source. The advantage of this two laser configuration is that it provides a highly accurate method to form a visible indicator of the incident x-ray from both directions. Thus imaging

components such as the pinhole collimators used in the spectral measurements can be aligned very intuitively and precisely through the help of the laser beams.

The alignment process is described in detail after a brief description of the target x-ray imaging system [10, 80–82] on which the alignment approach was implemented. In addition, the adjustment of the coverage of the x-ray beam on the detector is also presented, as it is considered a critical part of the system tuning process because it ensures a relatively uniform x-ray field on the detector.

5.2 Materials and methods

5.2.1 Description of the imaging system

The imaging system utilized in this study employs a micro-focus x-ray source (Ultra-Bright, Oxford Instruments, CA) and a Computed Radiography (CR) system (Regius 190, Konica Minolta, NJ) for image detection. The various imaging and measuring components of the system are mounted on a supporting optical rail on which their positions can be conveniently adjusted.

Standard opto-mechanic components were used to form the holding structures for the measurement devices, lasers, detectors, objects and the x-ray tube, due to their ability to produce flexible, accurate and reproducible alignment and positioning for the imaging components. In addition, linear and rotational stages were also utilized to effectively and precisely control their horizontal, vertical and angular positions.

5.2.2 The alignment procedure based on two laser positioning devices

Precise alignment is essential in certain measurements and imaging tasks, as discussed in Section 5.1, although it often requires arduous efforts and is therefore very time consuming. In order to ease the difficulty and to improve the accuracy of the alignment tasks, two laser pointers were used to establish a visible indicator of the incident

x-ray beam. The laser pointers were mounted at opposite ends of the supporting rail and positioned to face each other, as shown in Fig. 5.1. During the alignment process, the laser facing the x-ray source, hereafter referred to as Laser-1, was first calibrated to ensure that the laser beam constantly pointed towards the output window of the x-ray tube when the position of the laser was adjusted along the optical rail. This verified that the laser beam was parallel to the direction along which the components were positioned, which was the direction of the supporting optical rail in this study. The beam of Laser-1 thus indicated the position of the x-ray source with respect to the supporting rail, and provided a baseline for the other laser to be calibrated.

The laser at the opposite end of the rail, hereafter referred to as Laser-2, was then adjusted so that the beam coincided exactly with the beam from Laser-1. To verify this, two transparency films were placed a distance of approximately 20 cm apart within the path of the two laser beams. The congruence of the laser beams was confirmed when the laser dots on both sides of each transparency film were overlapping. To provide a numeric measure of the coincidence of the laser beams, another transparency film bearing a 10cm-x-10cm grid with line spacing of 1 mm was also utilized. The transparency was fixed to the optical rail by a holder which could travel along the rail. While moving the transparency film along the rail, the position of the laser dots on the grid from both Laser-1 and Laser-2 were recorded individually and both determined to hold a constant position of [4.2mm, 3.5mm]. This correspondence of the laser positions thus verified that the laser beams were coinciding and parallel to the optical rail. Since the direction of the beam from Laser-2 was the same as that of the x-ray from the source, it provided an intuitive illustration of the incident x-ray. This preparation enabled the position of the object, detectors and other devices to be aligned easily and accurately with the help of the two laser beams. It should be noted that although the two lasers employed in this study both generate red-colored lasers, the use of different colored lasers (red and

green for example) may make the alignment even more convenient.

Although Laser-2 is more convenient to use in the alignment process due to the direction of its beam, it must be removed from the path of the x-ray to allow image acquisition and measurements. Laser-1, which is located at the opposite end of the supporting rail from the x-ray source, can maintain its position during the imaging and measurement processes, and thus facilitates reestablishing the alignment of Laser-2. Verifying that the two laser beams are parallel to the supporting optical rail is critical for this alignment process, as the laser beams function as the baseline for mounting and positioning other imaging and measuring components along the rail.

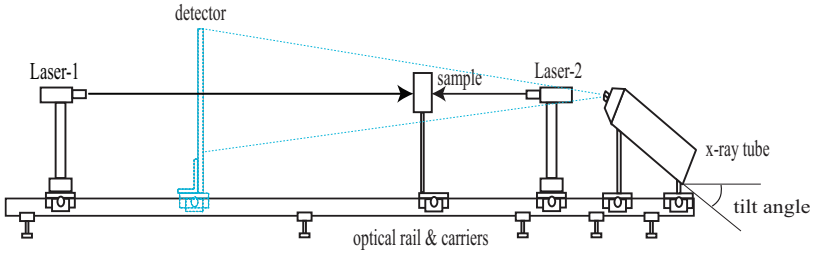

Figure 5.1: Schematic of the alignment process

5.2.3 Laser alignment of collimators in spectral measurements

In spectral measurements, pinhole collimators are commonly used to limit the flux of the incident x-ray arriving on the spectrometers [76, 78, 79]. In the spectral experiments performed in this study, a CdTe detector (XR-100T-CdTe, Amptek Inc., Bedford, MA) was employed. Although the vendor of the spectrometer provided a collimator kit and detailed the implementation of a two-pinhole-collimator approach [78] to aid the collimation process, the precise alignment of the collimators and input window of the CdTe detector with respect to the direction of the incident beam remains a difficult task. This is due to the fact that the pinhole collimators must be aligned concentrically with respect to each other, as well as the direction of the incident beam, in order to reduce the beam filtration resulting from the collimation. Using

our two-laser alignment approach, this problem could be adequately solved. When the coinciding laser beam from both Laser-1 and Laser-2 is established as described in Section 5.2.2, the laser from Laser-2 could be utilized as a visible substitute for the incident x-ray beam in the spectral measurements. Thus when the laser from Laser-2 results in the brightest and roundest dot on the plane of the spectrometer's input window after passing through the collimators, a good alignment is achieved. On the other hand, if the collimators were misaligned, no laser dot could be observed (see Fig. 5.2 for more details).

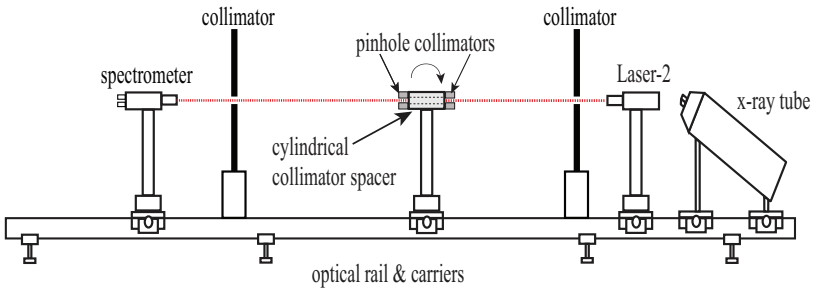

Figure 5.2: The alignment of the collimators and the spectrometer with respect to the direction of the incident x-ray beam using the two-laser alignment approach. The beam from Laser-2 is utilized as the visible indicator of the incident x-ray beam. The pinhole collimators are then aligned concentrically with respect to each other, as well as the direction of the incident beam.

5.2.4 Adjustment of the x-ray beam coverage

In addition to aligning various components with respect to the x-ray source, it is necessary to adjust the placement of the x-ray source with respect to the detector position in order to ensure a relatively uniform x-ray field on the detector, which could help to reduce the background trends and/or artifacts in acquired images. The prototype system employs a free-standing source that features an output window that is aligned at an angle with respect to the electron beam, the design of which has been

reported to be helpful for producing a rounded micro focal spot. However, this design also introduces challenges into the alignment process. The angle between the x-ray tube and the supporting rail must be carefully adjusted in order to obtain relatively uniform beam coverage on the detectors, due to non-uniformities in the output x-ray field, such as the anode heel effect.

A series of images were acquired at different source to image distances (SIDs) for the adjustment of the tube angle. An initial image was acquired at an SID of 12 inches ($\approx$ 30 cm) to illustrate the shape of the entire x-ray field, which is determined by the intrinsic collimation of the micro-focus x-ray source. From this image, a portion of the entire field with uniform pixel values was selected to be shifted to the center of the detector and aligned directly with respect to the pixel array by adjusting the tube. Through this process the detector could be covered by this uniform portion of the field at larger SIDs. During the adjustment, several images at a larger SID (91 cm) were acquired to guide the adjustment of the x-ray tube to achieve a uniform x-ray field. Then images taken at even larger SIDs (122 cm, 127 cm and 132 cm) were obtained to further guide the tube adjustment and to determine the threshold SID, beyond which the entire detector (24 inch by 30 inch) is guaranteed to be covered by the uniform x-ray field. This threshold was determined to be 132 cm in our study, and was thus utilized in our experiments to ensure a uniform x-ray field.

5.3 Results

The accurate alignment of the tungsten pinhole collimators used in the x-ray spectral measurements (2 mm thick, with diameter of 100 μm and 200 μm, "Collimation Kit", Amptek Inc., Bedford, MA) were verified through the use of x-ray images. The collimators were aligned with respect to the incident x-ray beam, separated by a 36 mm long brass collimator spacer with an aperture of 5-mm diameter, as shown in Fig. 5.2. Two images of the pinhole collimators were obtained with magnification

of approximately 5, at 20 kV, 2 mA and 400s. With a good alignment, the pinhole x-ray image obtained was a rounded dot; as the angle of the collimators (Fig. 5.2) was tilted 0.1 degree away from the good position, the pinhole dot shrank and its shape was blurred; as the angle was tilted further (greater than 0.3 degree), the dot disappeared.

To further illustrate the advantage of using the two laser alignment approach, an example application of spectral measurements is provided. X-ray spectra were measured at 40 kV, 0.5 mA, 400s with a Mo-Be target-window combination. The placement of the spectrometer and collimators is shown in Fig. 5.2, and the distance from the source to the spectrometer was approximately 6 ft (183 cm). The influence of misalignment of the pinhole collimators can be observed through the photon rate received by the spectrometer, as well as the shape of the resultant spectra. With the collimators in good alignment with respect to the incident x-ray beam, the photon rate measured by the spectrometer was 1030 photon/s. However, with a misalignment of approximately 0.1, 0.2 and 0.3 degree away from the good alignment position, the photon rate reduced to 947, 222 and 103 photon/s, respectively. This is illustrated in Fig. 5.3, which compares the good alignment spectrum separately with each degree of misalignment. As the tilt angle was increased, the magnitude and shape of the spectrum obtained with misalignment gradually deviated from that acquired with good alignment. The difference in the magnitude is due to the decreasing photon rates in the spectral measurements, and the difference in the shape of the spectra is probably caused by the beam filtration from the collimators, which blocked and filtered the primary x-ray beam rather than only allowing a limited portion of photons in the primary beam to pass through their apertures.

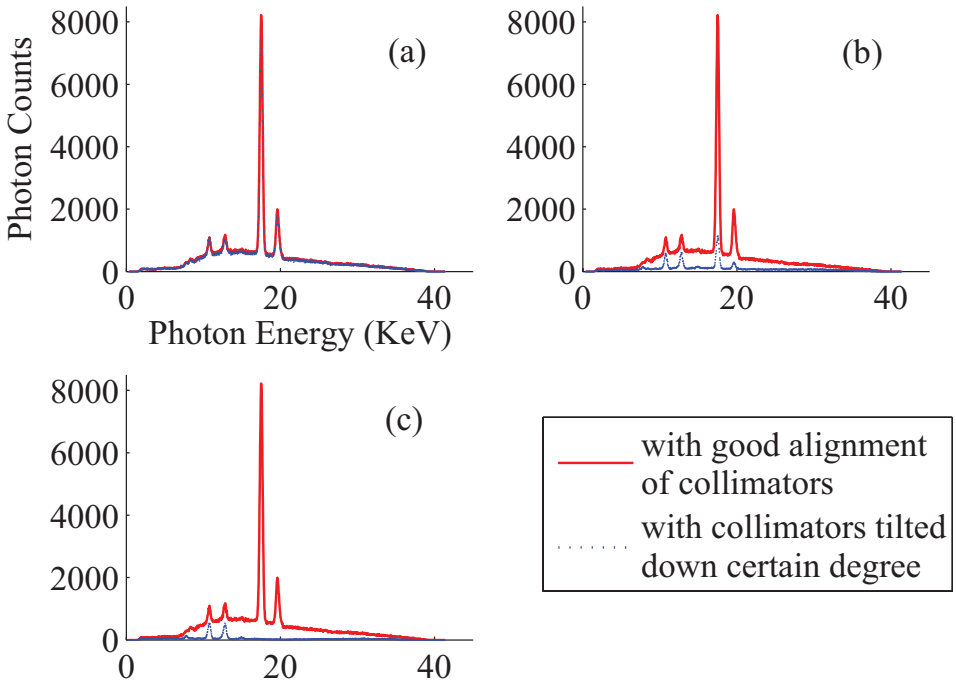

Figure 5.3: X-ray spectrum measured with a CdTe detector at a good alignment position of the two tungsten collimator disks compared separately with the spectrum obtained with a collimator position 0.1 (a), 0.2 (b), and 0.3 (c) degree tilted away from the good alignment position, respectively. The spectra were measured at 40 kV with a Mo-Be target-window combination.

Profiles on both x direction (the short side of the image) and y direction (the long side of the image) of the x-ray field after the adjustment of the tube are shown in Fig. 5.4. The image was taken at 40 kV, 0.5 mA, and 12 s, with an SID of 52 inches (132 cm), which was the threshold SID beyond which the entire detector could be covered by the uniform x-ray field, as mentioned in Section 5.2.4. The profiles were measured as the mean of 1000 rows on the x direction and 1000 columns on the y direction at the center of the image. The maximum and minimum values of the measured profile on x direction are 2581 and 2608, respectively; the maximum and

minimum values of the profile on y direction are 2589 and 2607, respectively.

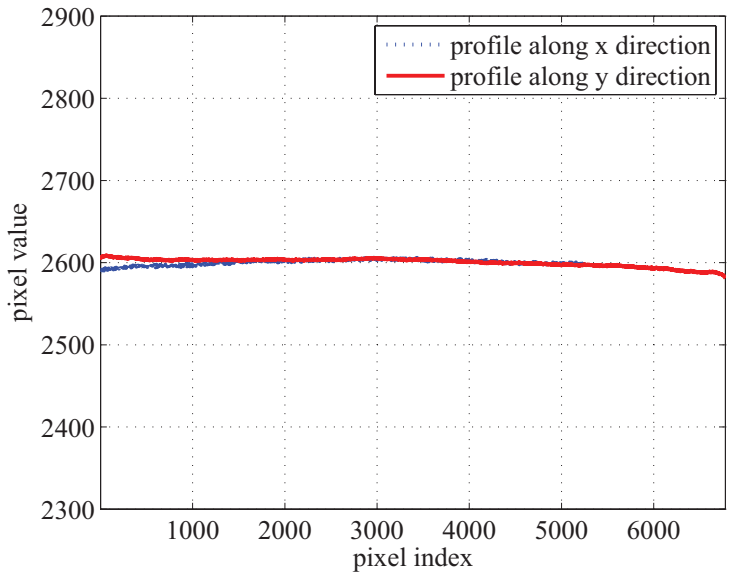

Figure 5.4: Profile of the x-ray field on the detector after the adjustment of the placement of x-ray tube. The image was taken at 40 kV, 0.5 mA, 12 s and with SID of 52 inches (132 cm).

5.4 Chapter conclusion

This paper reports a convenient two-laser alignment approach by which the positioning of the imaging and measuring components with respect to the x-ray beam can be easily achieved. The first laser was positioned a distance from the source with its beam adjusted to constantly point towards the output window of the x-ray tube and parallel to the direction along which the components are placed. Then the second laser was calibrated to ensure that its beam coincided with the beam from the first laser. After that, a visible indicator of the direction of the x-ray beam was established and the imaging components could thus be aligned conveniently and accurately. One of the advantages of the proposed alignment approach was illustrated in x-ray spectral measurements in which the pinhole collimators and the spectrometer could

be conveniently and precisely aligned with respect to the direction of incident x-ray beam based on the laser beam.

The proposed alignment approach could also be adapted to clinical settings under which the x-ray tube beam exit window is not visible, although this would introduce some additional steps for our alignment approach to be applied to clinical systems. For example, as indicated by the literature [74, 79], pinhole focal-spot radiography could be used to determine the position of the focal spot, and the pinhole placed in front of the tube could thus be used as a indicator of the focal spot position. In addition, the optical rail and opto-mechanic components may not be applicable in a clinical setting, although they play an important role as the base for accurate and reproducible alignment in this experimental environment. However, the idea of this precise two-laser alignment approach would still apply in such settings. For example, a device as shown in Fig. 5.5 could be constructed and utilized, which consists of a supporting plane that is perpendicular to the first laser beam and a supporting arm for moving the second laser. The arm would permit the laser to swing back and forth from the alignment position where the two beams are coinciding to an alternate location allowing Laser-1 to point to the focal spot position. For most clinical systems, the x-ray beam is designed so that the central x-ray is perpendicular to the detector, thus the device in Fig. 5.5 would provide an acceptable means for precise alignment utilizing the coincident laser beams.

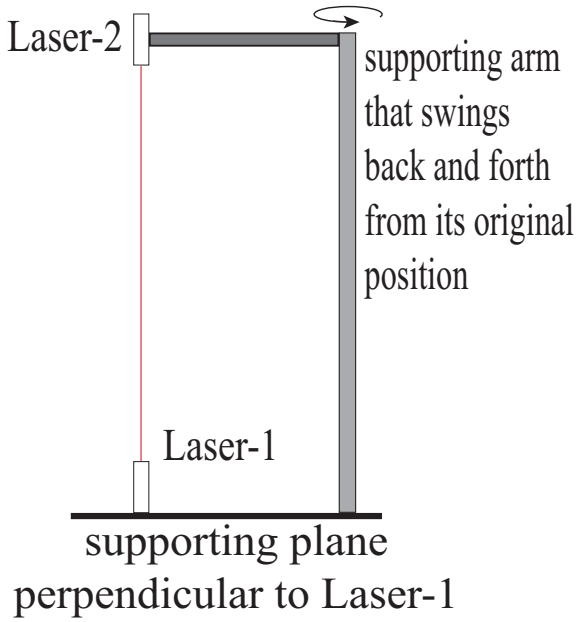

Figure 5.5: Schematic of a device for applying the proposed alignment approach in a clinical setting

In conclusion, the reported alignment process is suitable for facilitating accurate image acquisition and measurement, as it provides a precise and simple method for ensuring the alignment of various components with respect to the direction of incident x-ray beam.

CHAPTER 6

On the measurement of modulation transfer functions

6.1 Chapter introduction

In the previous chapters, the theory of DQE and one of the constituent measurements–photon fluence–are discussed. In this chapter, the measurement of another constituent part of the DQE–Modulation Transfer Function (MTF)–is detailed.

MTF demonstrates the resolving power of an imaging system as a function of spatial frequency, and is a widely-accepted measurement of system performance in the sense of contrast transfer and spatial resolution [8,39,73,83–87], not only in the clinical environment for verification of successful operation, but also in research field for the comparison among different imaging systems and techniques [24, 39, 74, 83, 84, 86–93].

Similar to the Fourier Transform based signal-and-system analysis for electrical systems in the time domain [36, 40], the concepts of impulse response function and transfer function can also be applied to imaging systems. This analysis requires the electrical systems in time domain or spatial domain to be linear and shift-invariant (LSI).

The impulse response function in imaging systems can be either in the form of Point Spread Function ($psf(x, y)$), or in the form of Line Spread Function ($lsf(x, y)$). The system transfer function, as the Fourier Transform of the impulse response function, can be either the function of the spatial frequency (u, v) in 2D frequency domain, or the function of the spatial frequency (f) in 1D frequency domain.

As discussed earlier in Section 1.1.1, 1D continuous MTF is closely related to the line spread function by the fact that MTF is the normalized modulus of the Fourier

Transform of LSF [6, 8, 9]:

$$MTF(f) = \frac{|FT\{lsf(x)\}|}{FT\{lsf(x)\}|_{f=0}}, \tag{6.1}$$

where $FT\{\ \}$ denotes the Fourier Transform, and $|\ \ |$ stands for the modulus operator.

This relationship between the $MTF(f)$ and $lsf(x)$ can be considered as similar to the relationship between the modulus of the system function in frequency domain and the impulse response function in the time domain for general electrical systems.

6.2 Measurement of line spread function

6.2.1 Acquisition of the slit image

To determine the $MTF(f)$ of an x-ray imaging system using the slit method [39], the line spread function (LSF) needs to be measured. A slit camera is often employed to collimate the incident x-ray beam into a sharp line input to the imaging system, and based on the "over sampling" method [39], the slit is positioned at a small angle with respect to one axis of the detector. Then LSF is obtained by scanning the x-ray image of the sharp line in order to find the intensity value for each pixel and the distance from each pixel to the slit line. The resultant LSF is a curve of the intensity of each pixel vs. the distance from each pixel to the slit line, as shown in Fig. 1.4. Fig. 6.1 illustrates the placement of the slit camera: the slit is positioned with a small angle $alpha$ ($\approx 2^o$) to the i axis which is the scanning direction in the algorithm discussed below.

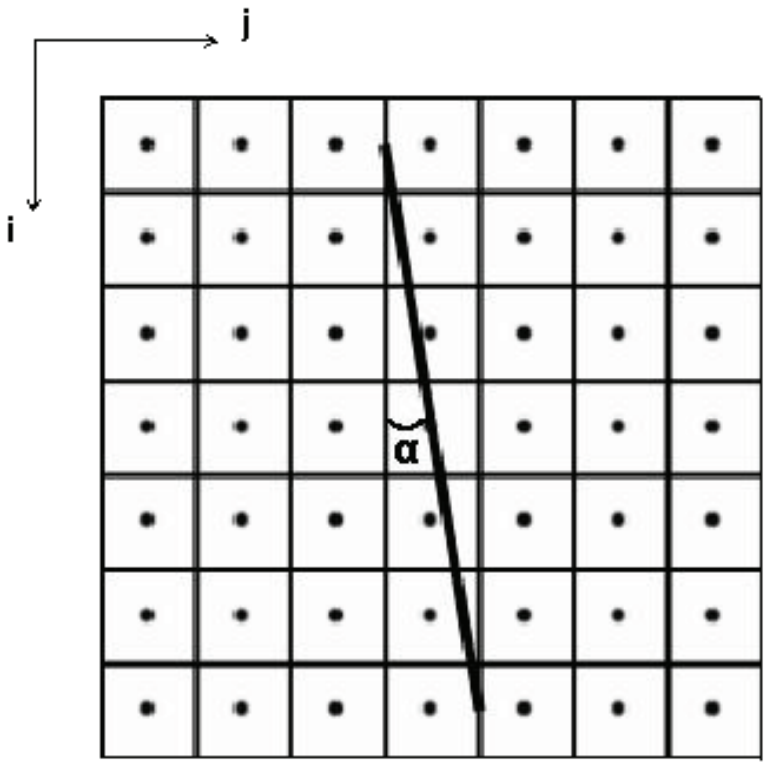

Figure 6.1: Schematic of the region of interest in a slit image that is used in the LSF measurement. The slit camera is placed with an angle α from the positive direction of the i axis.

For the imaging of the slit camera, the exposure level needs to fall within the linear response region of the imaging system, otherwise the requirement that the imaging system should be an LSI system will not be met. The linear response region is the range of exposures in which the output intensity of the system has a linear relationship with the exposure level.

In the following example MTF experiments on a CCD based x-ray imaging system (MX-20, Faxitron X-Ray Corporation, Wheeling, IL), a 10 μm wide slit camera is placed on the detector as described above. The slit image was taken under 26 kVp, 0.3 mA and 5 seconds of exposure time (2.19 mR of entrance exposure), and Fig. 6.2 shows the resultant slit image.

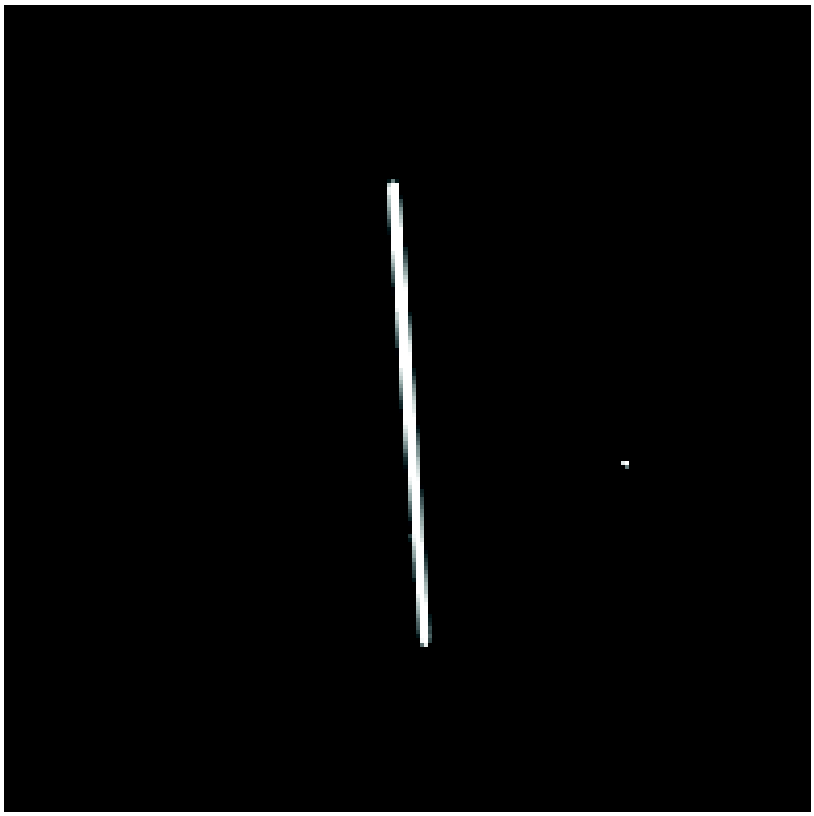

Figure 6.2: X-ray image of a slit camera, taken with the CCD-based x-ray imaging system at 26 kVp, 0.3 mA, 5s.

6.2.2 Determination of the slit line function

After the slit image is obtained, the first thing is to find the line function of the slit on the image:

$$j = a \cdot i + b. \tag{6.2}$$

Linear fitting is often used to determine the parameters in Eq. (6.2) based on the least square error method [66]. The coordinates (i_n, j_n) of pixels with the maximum intensity in each row are first found out, shown in Fig. 6.3. Then these coordinates

are analyzed in the following manner to find the slope a and the intercept b:

$$a = \frac{n\sum_{n=1}^{N} i_n j_n - \left(\sum_{n=1}^{N} i_n\right)\left(\sum_{n=1}^{N} j_n\right)}{n\left(\sum_{n=1}^{N} i_n^2\right) - \left(\sum_{n=1}^{N} i_n\right)^2}, \tag{6.3}$$

$$b = \bar{j} - a\bar{i}, \tag{6.4}$$

where $\bar{i}$ and $\bar{j}$ are the mean values of the coordinates (i_n, j_n), N is the total number of pixels involved in the linear fitting. As can be seen in Fig. 6.1, the tangent value of the angle α equals the slope of the a. Hereafter α, which is the angle from the positive direction of the i axis to the slit line, if referred as the "slit angle".

Fig. 6.3 illustrates the slit line determined from the slit image in Fig. 6.2. The slit angle α was determined as 0.42 degrees.

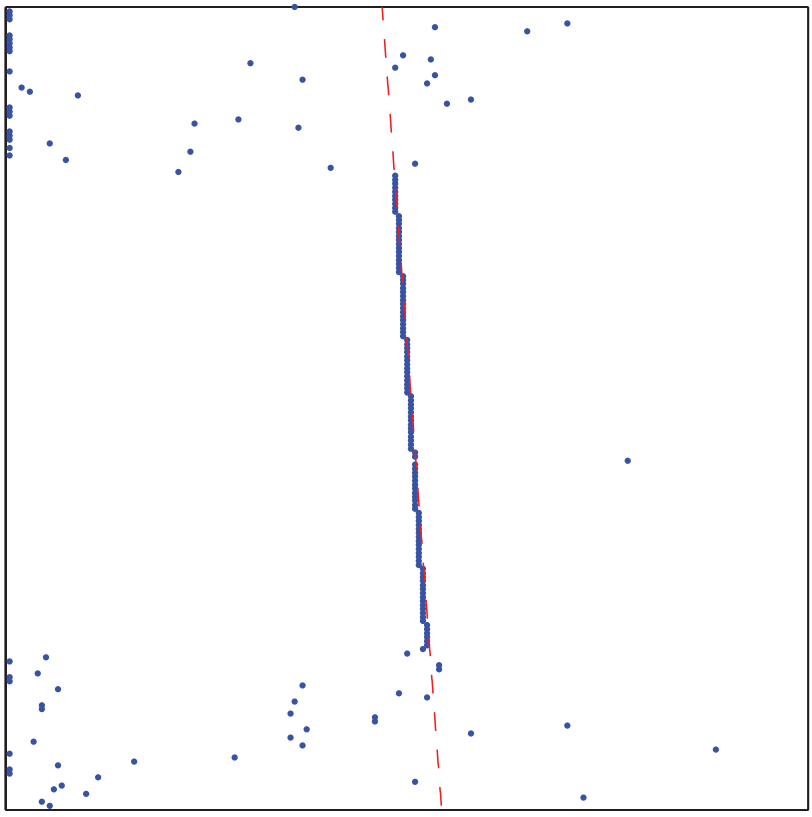

Figure 6.3: Illustration of the slit line determined from the slit image in Fig. 6.2.

6.2.3 Selection of the region of interest

With the knowledge of the position and the orientation of the slit line, we can set a specially selected region containing the slit as the region of interest (ROI) to calculate the LSF. The number of rows in the ROI should be the cotangent value of the slit angle α so that the slit line just passes through one column of pixels, which is shown in Fig. 6.1. In the ideal case, the number of rows in the region of interest equals to $(cotan(\alpha))$, and the number of columns in the region of interest should be large enough to cover the tails of the line spread function. Fig. 6.4 shows an example of the region of interest used in the algorithm. If the cotangent value of the slit angle α is not exactly an integer, then there will be some variation in the effective sampling distance.

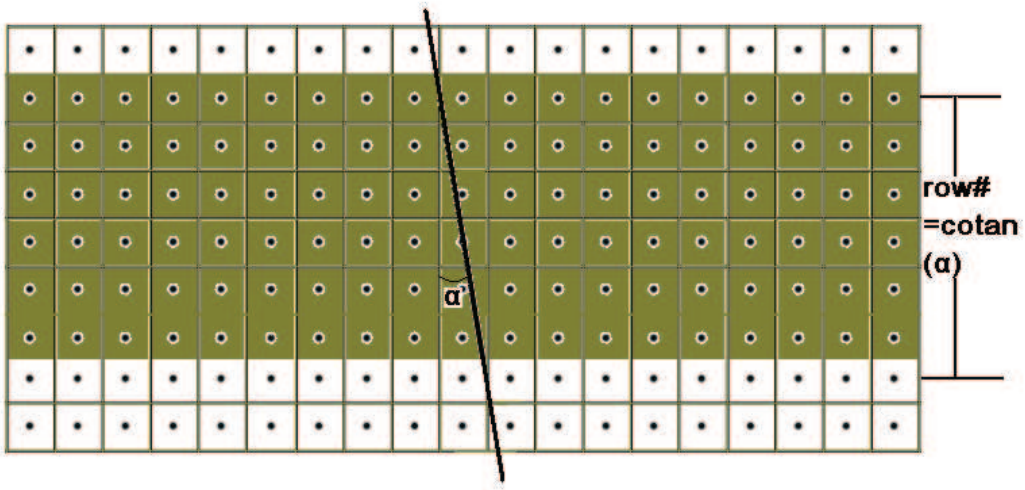

Figure 6.4: Region of Interest in the LSF acquisition algorithm. The shaded area is the Region of Interest.

The reason to choose the number of rows as $cotan(\alpha)$, which is a limited number compared to the real slit length, is that if a larger number of rows is selected, there will be some redundant pixels whose distance from the slit line are the same. This is

shown in Fig. 6.5.

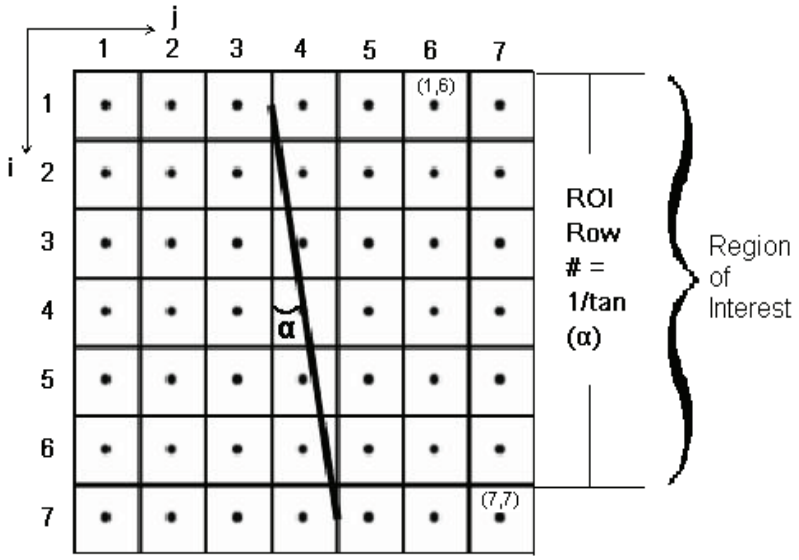

Figure 6.5: Illustration of the reason why the fixed number of rows is selected.

In Fig. 6.5, the ROI covers the 1st to the 6th row, and we can see that if the 7th row is selected, there will be some redundant data. For example, the distance from the pixel (1, 6) to the slit line and the distance from (7, 7) to the slit line are actually the same, which is 2.5 pixel pitches. So the pixel (1, 6) and (7, 7) are redundant in the calculation of LSF that is the curve of the pixel intensity values vs. the distances from the pixels to the slit line.

6.2.4 The scanning procedure

When we scan through the ROI to determine the LSF, some consideration about the direction of scanning should be taken, since it is desirable to have the distance from each pixel to the slit line in an increasing order or a decreasing order. Take the slit in Fig. 6.5 as an example, we apply the scanning from the 6th pixel of the 1st column (6,1) all the way to the 1st pixel in the 1st column (1,1), and then to the 6th pixel of the 2nd column (6,2)... This procedure is illustrated in Fig.6.6. If this scanning strategy is not taken, then a sorting through the scanning result of the LSF data pairs

(distance, intensity) is needed so that the data pairs are sorted into an ascending or descending order according to the distances.

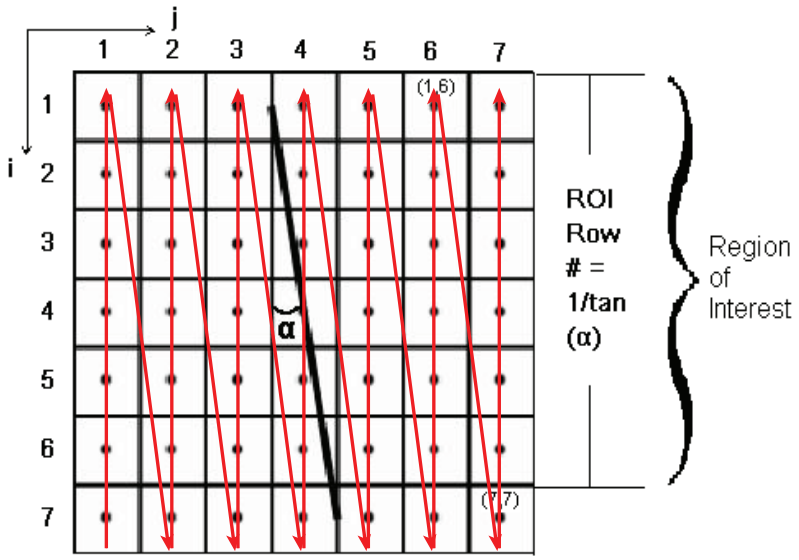

Figure 6.6: Illustration of the scanning procedure for the LSF calculation.

After the scanning procedure, LSF is generated as the pixel values in the ROI vs. the distances from the pixels to the slit line determined in Section 6.2.2. Fig.6.7 shows the LSF that is generated based on the slit image in Fig. 6.2, the curve is normalized to its maximum value.

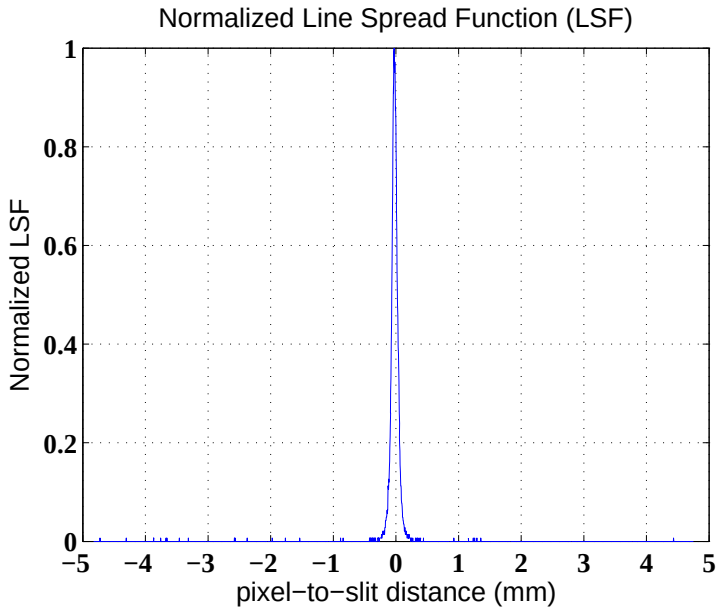

Figure 6.7: Normalized LSF curve. LSF is generated as the pixel values in the region of interest vs. the distances from the pixels to the slit line illustrated in Fig. 6.3.

6.2.5 Relationship between the slit angle α, the effective sampling distance, and the pixel pitch of the imaging system

When we calculate the distance from each pixel in the ROI to the slit line, the impact of the slit angle α on the pixel-to-slit distance should be considered. For example, in Fig.6.8, the pixel-to-slit distance of the pixel C (3, 7) (hereafter referred as CB) can be calculated from the horizontal distance from the pixel C to the slit line (hereafter referred as CA):

$$CA = [j_c - (a \cdot i_c + b)] \cdot \Delta x, \tag{6.5}$$

where a and b are the slope and the intercept of the slit function in Eq. (6.2), Δx is the pixel pitch of the detector.

Then the pixel-to-slit distance of the pixel C is:

$$CB = CA \cdot cos(\alpha) = (j_c - (a \cdot i_c + b)) \cdot \Delta x \cdot \cos(\alpha), \tag{6.6}$$

where α is the slit angle mentioned in Section 6.2.2.

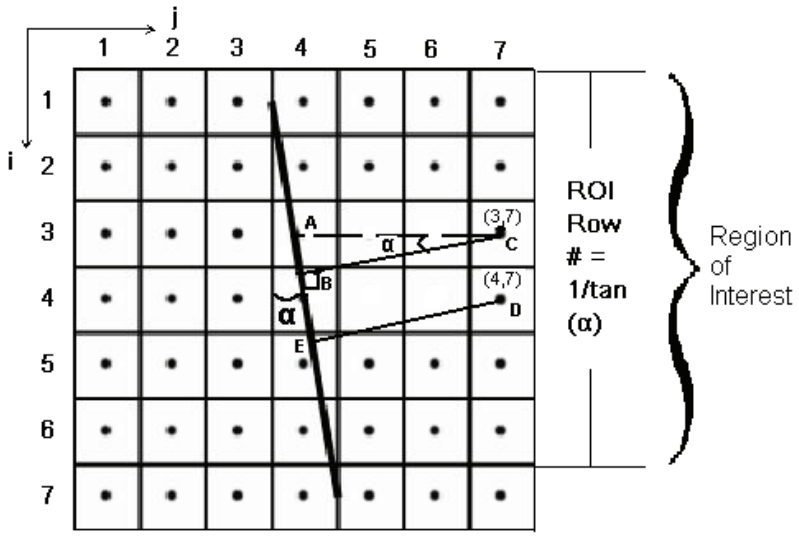

Figure 6.8: Illustration of the pixel-to-slit distance and the effective sampling distance.

The difference between the pixel-to-slit distance of two adjacent pixels in the scanning route (Fig. 6.6), such as (3, 7) and (4, 7), is the "effective sampling distance" in the LSF calculation. We denote the system pixel pitch as Δx, and the effective sampling distance as Δl. The relationship between the effective sampling distance and the system pitch can be derived as follows. In Fig. 6.8, the pixel-to-slit distance of the pixel D is:

$$DE = (j_d - (a \cdot i_d + b)) \cdot \Delta x \cdot \cos(\alpha). \tag{6.7}$$

So the effective sampling distance Δl is:

$$\begin{aligned}
&\Delta l = CB - DE \\
&= (j_c - (a \cdot i_c + b)) \cdot \Delta x \cdot \cos(\alpha) - (j_d - (a \cdot i_d + b)) \cdot \Delta x \cdot \cos(\alpha) \\
&\overset{j_c = j_d}{=} a \cdot (i_d - i_c) \cdot \Delta x \cdot \cos(\alpha) \\
&= \tan(\alpha) \cdot \cos(\alpha) \cdot \Delta x \\
&= \sin(\alpha) \cdot \Delta x.
\end{aligned} \tag{6.8}$$

As shown in Eq. (6.8), the effective sampling distance Δl is much smaller than the

sampling distance of the detector (the pixel pitch), and this enables the measurement of LSF in a much more detailed manner.

6.3 Determination of MTF from LSF

According to Eq. (6.1), the MTF is equal to the normalized modulus of the Fourier transform of the LSF. Therefore the practical algorithm for the calculation of $MTF(f)$ from $lsf(x)$ is:

$$MTF(m) = \frac{abs(fft(lsf(n)))}{max(abs(fft(lsf(n))))}, \tag{6.9}$$

where $fft()$ stands for Fast Fourier Transform; m is the index of the resultant FFT sequence $fft(lsf(n))$; $-N/2+1 \leq m \leq N/2$, and N is the number of data points in $lsf(n)$; $abs()$ takes the complex modulus of the result of the FFT on the LSF data $lsf(n)$; MTF is normalized to the max of the resultant complex modulus of the FFT sequence, which occurs at the zero frequency $m = 0$.

As the result of the above calculation is based on the index m, a conversion is needed to change m into spatial frequency f (with the unit of lp/mm). Since the oversampling method [39] is utilized in the LSF measurement, the effective sampling distance is used in the scanning of the slit image, which means the continuous line spread function is sampled at the effective sampling distance. According to the sampling theory, the frequency interval equals to the reciprocal of the physical length of the input array, which is the product of the sampling distance and the number of samples:

$$\Delta f = \frac{1}{L} = \frac{1}{N \cdot \Delta L}, \tag{6.10}$$

where N is the number of samples in the data sequence; Δl is the sampling distance in the unit of mm; Δf is the frequency interval in the unit of lp/mm.

Therefore the relationship between the index of the result FFT sequence and the

spatial frequency is:

$$\begin{aligned} f &= m \cdot \Delta f \\ &= m \cdot \tfrac{1}{N \cdot \Delta l} \\ &= \tfrac{m}{N/2} \cdot \tfrac{1}{2\Delta l}, \end{aligned} \tag{6.11}$$

where m is the index of the resultant FFT sequence $fft(lsf(n))$; $-N/2+1 \leq m \leq N/2$, and N is the number of data points in $lsf(n)$.

Since the resultant FFT sequence contains both the positive frequency components and the negative frequency components, the index corresponding to the highest frequency is $N/2$. Therefore from Eq. (6.11) the maximum frequency for the result $MTF(f)$ should be

$$f_{max} = \frac{1}{2 \cdot \Delta l}, \tag{6.12}$$

where N is the number of samples in $lsf(n)$, which is also equal to the number of the result FFT sequence; $\frac{1}{2 \cdot \Delta l}$ is often called the Nyquist frequency corresponding to the effective sampling distance Δl.

Eq. (6.12) explains why we set the maximum frequency of the FFT result as the Nyquist frequency, it also indicates that why we use the effective sampling distance instead of the system pixel pitch to calculate the highest frequency of the result $MTF(f)$ in the case of oversampling. From this point we can also find relationship between the new Nyquist frequency ($f'_{Nyquist}$) corresponding to the effective sampling distance and the original Nyquist frequency ($f_{Nyquist}$) corresponding to the system pixel pitch:

$$\begin{aligned} & f'_{Nyquist} \\ &= \tfrac{1}{2 \cdot \Delta l} \\ &= \tfrac{1}{2 \cdot \sin(\alpha) \cdot \Delta x} \\ &= \tfrac{1}{\sin(\alpha)} \cdot f_{Nyquist}, \end{aligned} \tag{6.13}$$

where $f'_{Nyquist}$ is the Nyquist frequency corresponding to the effective sampling distance Δl, and f_{Nyqist} is the original Nyquist frequency corresponding to the pixel

pitch of the imaging system Δx.

We can see that after we calculate the $MTF(f)$ from the LSF obtained using the oversampling algorithm, the highest frequency reaches far beyond the original Nyquist frequency of the imaging system. And therefore we have to truncate the result $MTF(f)$ back into the frequency range $[0, f_{Nyquist}]$. As mentioned in Section 6.2.2, the slit angle α was determined as 0.42 degrees, and the system pixel pitch is 0.048 mm. Then the effective sampling distance is

$$\begin{aligned} \Delta l &= \sin(\alpha) \cdot \Delta x \\ &= 0.0073903 * 0.048 \\ &= 3.5473 * 10^{-3}(\text{mm}). \end{aligned} \tag{6.14}$$

After the LSF was obtained, 2^K of the LSF data points was taken out as the input for the subsequent FFT calculation as described in Eq. (6.9). The data points were selected around the peak point of the LSF sequence. For example, in the LSF shown in Fig. 6.7, 2048 points were selected out of the total 3000 data points around the peak data point whose index is 1504, i.e., the data with the index from (1504-1023) to (1504+1024) were employed. So the result of the FFT also has 2048 data points. After saving only the positive frequency components of the resultant MTF sequence, the indexes were converted to the spatial frequency corresponding to the effective sampling distance using Eq. (6.11). The MTF of 2048 points is shown in Fig. 6.9.

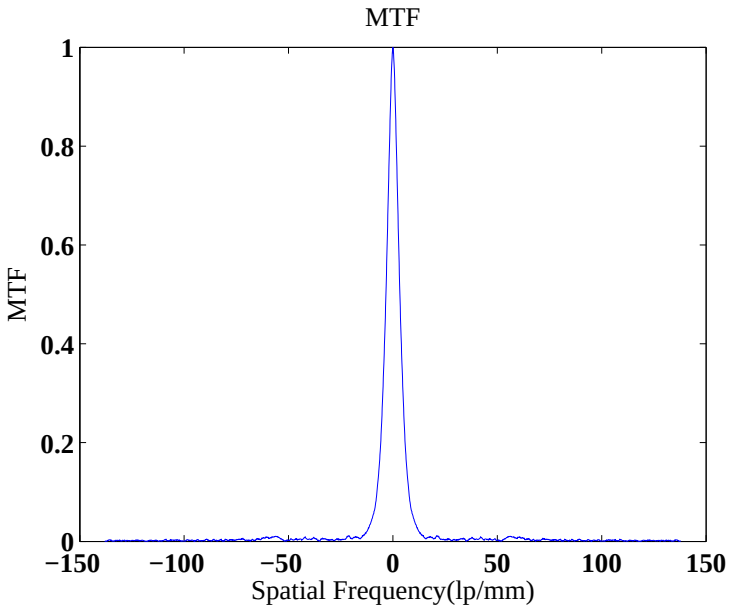

Figure 6.9: MTF curve calculated from 2048 data points taken out of the LSF in Fig. 6.7; the indexes have already been converted into spatial frequencies.

The next step after the acquisition of MTF based on the oversampled LSF is to truncate it bake into the frequency range $[0, f_{Nyquist}]$. In this example experiment, $f_{Nyquist} = 1/(2 * 0.048) \approx 10.417 lp/mm$. As can be seen in Fig. 6.9, the largest index corresponds to $f'_{Nyquist} = 1/(2 * 3.5473 * 10^{-3}) \approx 141 lp/mm$, which is about 13.3 times of the system Nyquist frequency $f_{Nyquist}$.

After truncating the MTF based on the oversampled LSF back in the frequency range $[0, f_{Nyquist}]$, the final MTF result is generated. The resultant MTF curve is shown in Fig.6.10.

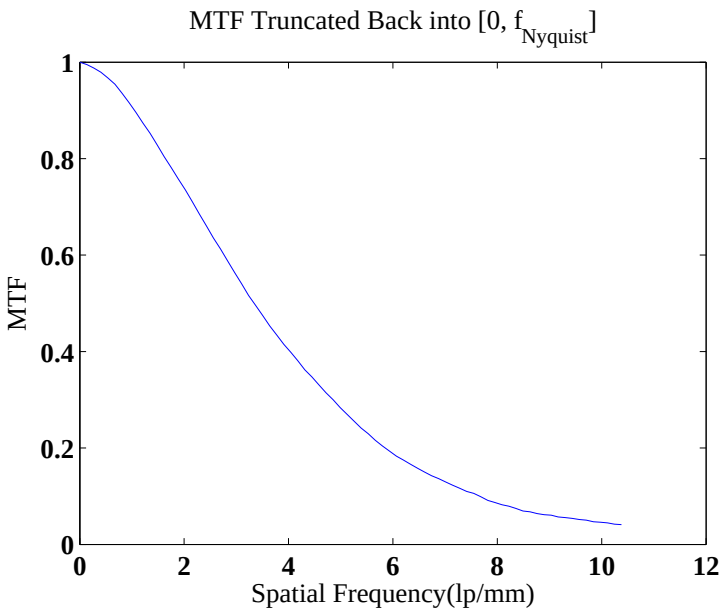

Figure 6.10: MTF truncated back into the frequency range $[0, f_{Nyquist}]$.

6.4 Chapter conclusion

The goal of this chapter is to provide a detailed measurement procedure of another constituent part of DQE–MTF–based on the slit method. As a widely-accepted measurement of system performance in the sense of contrast transfer and spatial resolution, MTF demonstrates the resolving power of an imaging system as a function of spatial frequency.

The measurement is detailed in three major steps: the acquisition of the slit image, scanning of the slit image to generate LSF, and the data processing to calculate MTF. The algorithm is summarized in Fig. 6.11.

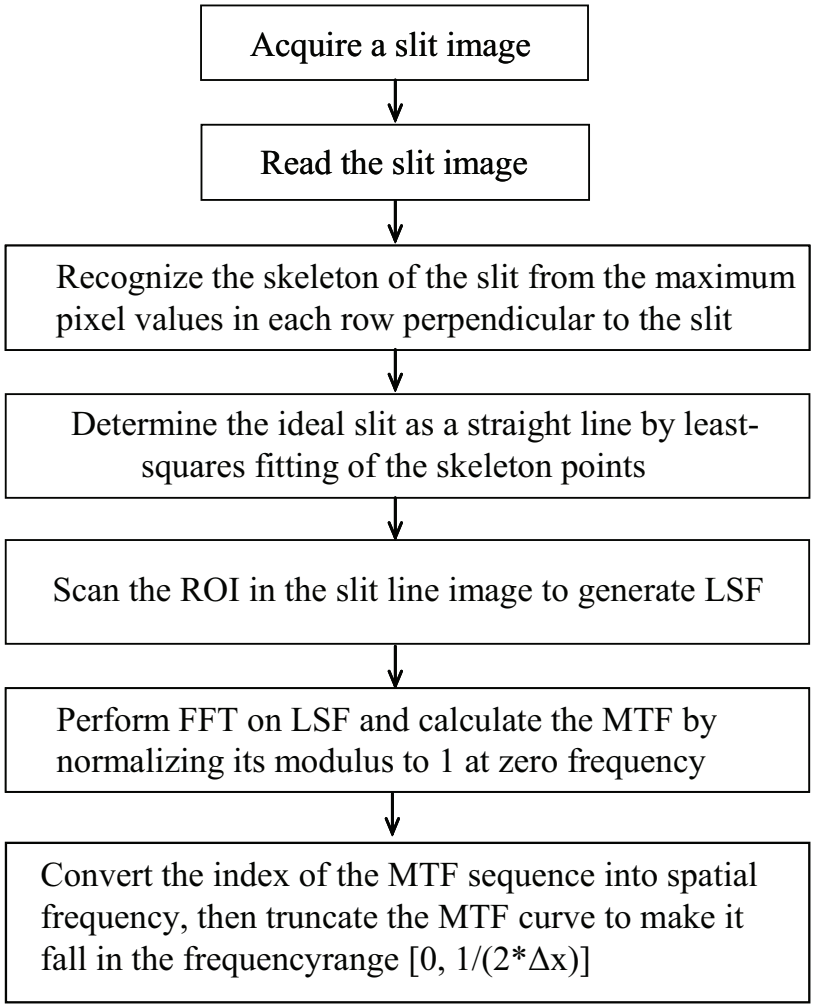

Figure 6.11: Flow chart for the MTF measurement.

CHAPTER 7

The impact of additive noise on the performance of a CCD based x-ray imaging system–an NPS based study

7.1 Chapter Introduction

NPS is a widely accepted system characteristic for quantitative evaluation of image quality and noise performance of an imaging system. A number of NPS measurement methods have been developed particularly for x-ray imaging systems [7,8,12,32,50,94].

For a digital x-ray imaging system, such as the CCD-based system employed in this study, the electrical detector system introduces noise to the x-ray imaging process. While the quantum noise from the fluctuation of incident photons per pixel is integrated within the x-ray signal, the noise from the electrical detector system is added to the signal. Sources of additive noise from the CCD include transfer loss noise, background charge generation noise, amplifier noise, and fast interface state noise [95]. The additive noise of an x-ray system usually increases with the operation time of the detector (exposure time in the case of x-ray imaging), particularly when the system is not cooled. When the exposure time exceeds a certain threshold, the system would no longer be quantum noise limited, which means that the quantum noise is no longer dominant in the overall noise level [15]. The NPS of the system and the quantum noise limit threshold are two important quantities of a system.

In this chapter, the measurement of NPS is firstly introduced, then the NPS of the additive noise of the aforementioned CCD system, particularly the growth trend of the additive noise with exposure time, was investigated. Moreover, DQE of the

system was measured and the quantum noise limit threshold was also determined.

7.2 NPS measurement

As introduced in Chapter 2, Noise Power Spectrum (NPS) is the power spectrum density function of a wide sense stationary random process. As discussed in Section 2.3.3 and 2.3.4, it is customary to assume ergodicity of the output random process [8, 22, 23, 26, 29, 33, 34, 37], and the NPS for the output images is often estimated through the periodogram approach [8, 11, 12, 22, 23, 26, 29, 33, 34, 37]. The traditional periodogram estimator for the 2D output NPS is [12, 29, 34]

$$\widehat{N_p}(u,v) = \frac{\Delta x^2}{MN}|\mathcal{D}\{\Delta P(i,j)\}|^2, \tag{7.1}$$

where M and N are the number of pixels on the two dimensions of the fluctuation image $\Delta P(i,j) = P(i,j) - p$; $\mathcal{D}\{\}$ denotes the 2D Discrete Time Fourier Transform (DTFT); u, v are the spatial frequencies ranging in $[-\frac{1}{2\Delta x}, \frac{1}{2\Delta x}]$.

The computational formula to calculate the 2D output NPS is:

$$\widehat{N_p}(m,n) = \frac{\Delta x^2}{MN}|FFT\{\Delta P(i,j)\}|^2, \tag{7.2}$$

where $FFT\{\}$ denotes the Fast Fourier Transform; where M and N are the number of pixels on the two dimensions of the fluctuation image $\Delta P(i,j) = P(i,j) - p$; $m \in [-\frac{M}{2}+1, \frac{M}{2}]$, $n \in [-\frac{N}{2}+1, \frac{N}{2}]$ are the indexes of the resultant 2D FFT array, and (m,n) need to be mapped to the spatial frequencies (u,v) by:

$$\begin{aligned} u &= m \cdot \tfrac{1}{M \cdot \Delta x}, \\ v &= n \cdot \tfrac{1}{N \cdot \Delta x}. \end{aligned} \tag{7.3}$$

As mentioned in Section 2.3.4, the periodogram estimator $\widehat{N_p}$ is as an asymptot-

ically unbiased estimator [8, 22, 23, 26, 29, 33], which means when the dimensions of the fluctuation image are infinitely large, the ensemble average of the periodogram estimator ($\widehat{N_p}(u,v)$) converge to the true NPS $N_p(u,v)$:

$$\lim_{M,N\to\infty} E\{\widehat{N_p}(u,v)\} = N_p(u,v). \tag{7.4}$$

Although the mean of $\widehat{N_p}(u,v)$ converges to the true output NPS as the size of the image data used in the periodogram estimator increases, the variance of the estimator does not reduce as the size increases [12, 23]. Therefore, ensemble averaging of the estimator $\widehat{N_p}(u,v)$ is necessary to reduce the variance and to improve the quality of the NPS measurements [12, 23]. A common practice to reduce the variance of the periodogram results is to partition a fluctuation image into a number of sub-images, and then average the periodograms calculated from the sub-images to acquire the mean periodogram [12, 16, 22, 23]. If altogether K uniformly exposed x-ray images are taken repeatedly under consistent conditions, and each image is partitioned into $S \times T$ sub-images, then the averaged NPS is:

$$NPS(u,v) = \frac{1}{K \cdot S \cdot T} \sum_{k=1}^{K} \sum_{s=1}^{S} \sum_{t=1}^{T} NPS_{k,s,t}(u,v), \tag{7.5}$$

where $NPS_{k,s,t}$ denotes the NPS estimated from the sub-image on s^{th} row and t^{th} column in the k^{th} image.

As compared to $NPS_{k,s,t}$, the variance of the averaged NPS is reduced by a factor of $K \cdot S \cdot T$. For example, if 50 images are taken under consistent conditions, the ROI of image contains 1024×1024 pixels, and each image is partitioned into $128 \times 128 - pixel$ sub-images, then NPS from altogether $50 \times (1024/128) \times (1024/128) = 320$ sub-images are used for the averaging, and the variance of the averaged NPS is 1/320 of that in the NPS estimated based on a single sub-image.

If the noise pattern of the images is isotropic, then 1D NPS could fully represent

the noise characteristics. In this case, the 1D NPS could be obtained by circularly averaging the 2D NPS [10–12, 27]:

$$NPS(f) = \frac{1}{N_f} \left(\sum_{f \leq \sqrt{u^2+v^2} < f+\Delta f} NPS(u,v) \right), \tag{7.6}$$

where $NPS(u,v)$ and $NPS(f)$ are the 2D NPS and 1D NPS, respectively. N_f is the number of data points in $NPS(u,v)$ within the interval $f \leq \sqrt{u^2+v^2} < f + \Delta f$.

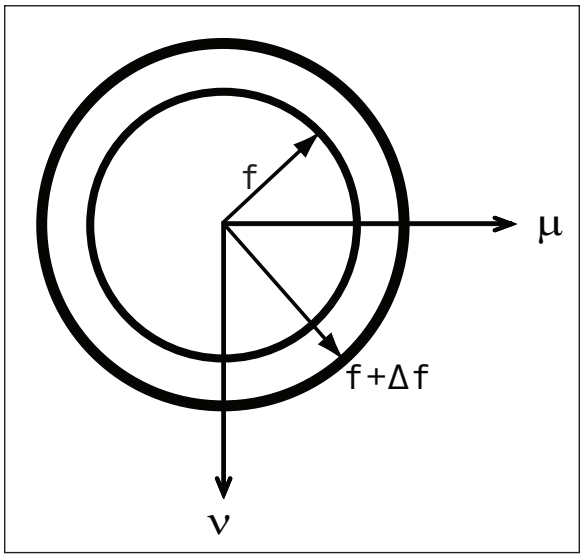

Figure 7.1: Illustration of the circular averaging algorithm used to obtain 1D NPS from 2D NPS

Fig. 7.2 and 7.3 demonstrated the 2D NPS and the corresponding 1D NPS (data published in [11]).

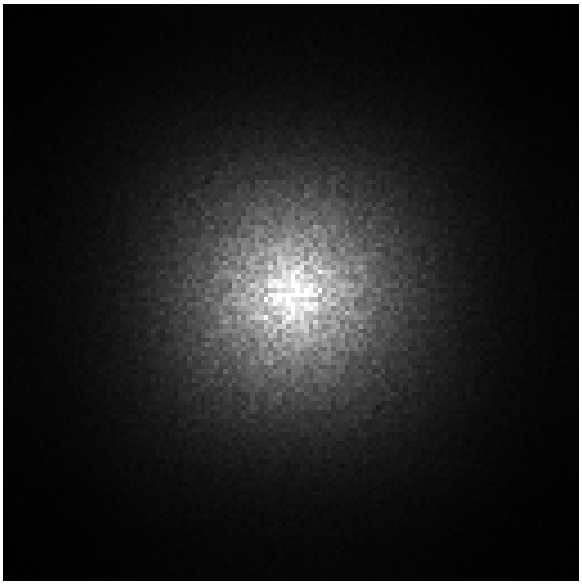

Figure 7.2: 2D NPS obtained with a CCD based x-ray imaging system at 26KV, 0.3mA, 6s

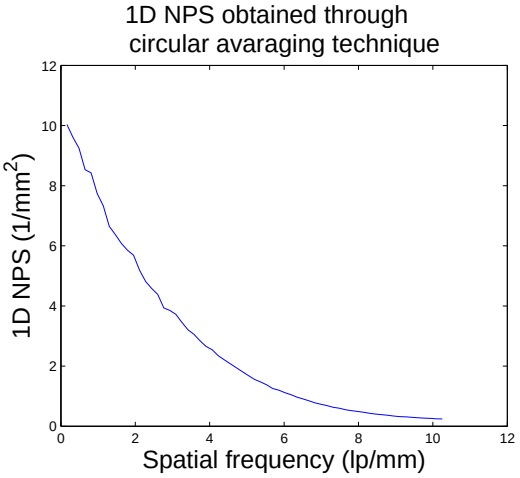

Figure 7.3: 1D NPS obtained from the 2D NPS in Fig. 7.2 through the circular averaging technique

The algorithm of the NPS calculation can be summarized in Fig. 7.4.

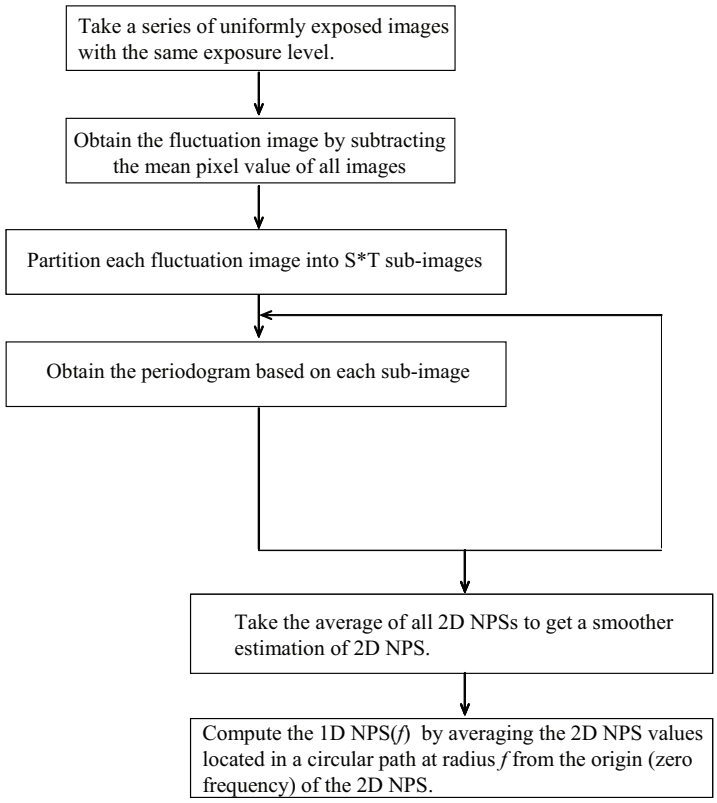

Figure 7.4: Flow chart of the NPS calculation algorithm

7.3 Impact of additive noise on the system performance of an CCD-based x-ray imaging system

7.3.1 Description of the imaging system

The imaging system employed in this study is a unique digital x-ray specimen prototype system that was designed for small animal studies (MX-20, Faxitron X-ray Corporation, IL). This system has an extremely small tungsten-target x-ray source with a $20 - \mu m$ focal spot, and the output window is covered by a 0.25-mm thick beryllium window. The source-to-object distance (SOD) can be adjusted over the range of 57.2 cm to 11.4cm. The detector used in this system consists of two CCD arrays (KAF-1001E, Eastman-Kodak, New York) which are abutted together. Each

CCD has a 24.5 mm x 24.5 mm photo active area with 1024 x 1024 pixels which are $24\mu m \times 24\mu m$ in size. An optical fiber taper is used to couple the CCDs to a Min-R scintillating screen (Eastman-Kodak, New York). The light photons converted by the scintillating screen are conveyed to the CCD detectors via the fiber taper at a demagnification ratio of 2:1. Finally the CCD detectors convert the light photons into 12-bit digital data which are transmitted to and processed by a computer. The CCDs in this system are not cooled, and the advantages of using an un-cooled detector include reduced cost, compactness of the system, and less maintenance for both clinical and experimental environments. The schematic of the imaging system is shown in Fig.7.5.

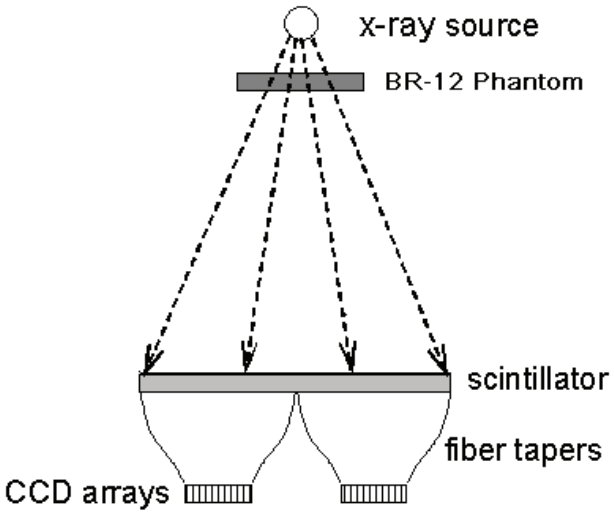

Figure 7.5: Schematic of the digital X-ray imaging system. The BR-12 phantom is placed near the X-ray source. The two CCDs are abutted together and connected to the scintillator through optical fiber tapers.

During the experiments, the x-ray system worked at 0.3 mA, 26 kVp, over various exposure times ranging from 3s, 7s, 9s, 10s, 15s, 20s, 30s, 40s, and 50s. In our experiments, a 3-cm-thick BR-12 phantom (50% water and 50% adipose, Nuclear Associate, New York) was placed on a shelf with an SOD of 11.4 cm in order to

ensure the detector worked in its linear response range for all the exposure times employed in this study.

7.3.2 Assumption of the quantum limited condition in x-ray imaging

For x-ray imaging systems, most noise can be divided into two groups. One is quantum noise which is inherent in the x-ray beam and is caused by the variation of the number of x-ray photons received per pixel. For well-designed x-ray imaging systems, the noise properties of the images should be governed by the x-ray quanta, which means that the noise of imaging system should be dominated by the x-ray quantum noise (often referred as "quantum noise limited") [6, 15]. The other group of noise is the additive noise introduced by the electronic devices in the system; the level of additive noise depends significantly on the operating temperature of the electronic devices. When the sensor of the imaging system is cooled, the thermal noise can be reduced [96]. However, the x-ray imaging system under the current study does not employ a cooling system. Therefore, the temperature-related noise of this system is expected to become unacceptably high with extended exposure time.

7.3.3 Experimental design

It is known that the thermal noise in an electronic device increases with the operating temperature which rises as a result of extended exposure time. Our hypothesis is that when the exposure time of a system is long enough, the thermal noise will increase significantly, eventually making the assumption of x-ray quantum noise limited condition invalid and therefore degrading the DQE of the system. To test this hypothesis, the following experiments were conducted. NPS of the additive noise and DQE were obtained at the exposure time varying from 3s to 50s. The NPS of the additive noise was compared with that of the system noise, i.e., the noise of the entire imaging system, to determine the increase and the impacts of the additive noise.

Selection of the Phantom Thickness and the Linear Response Range of the System

As limited by the MX-20 x-ray imaging system employed in the study, there is only one tube current available (0.3 mA). In order to carry out the experiments designed to evaluate the DQE of the system with extended exposure time, the 3-cm-thick BR-12 phantom was used in order to extend the response range in which the intensity of output images has a linear relationship with the exposure time. The phantom was used because it can attenuate a part of the x-ray beam, reducing the x-ray quanta on the detector, hence requiring a longer exposure time for the CCDs to reach their integration limit. To determine the linear response range, under 26 kVp and 0.3 mA, two series of exposure time were selected for a 2.5-cm phantom and a 3-cm phantom. At different exposure times, uniformly exposed images were taken. A region of interest (ROI) of 512 x 512 pixels was selected at the center of the left CCD area to avoid the edge effect of the detector. Fig. 7.6 shows the two curves of pixel-value vs. exposure time taken with the 2.5-cm thick phantom and the 3-cm thick phantom.

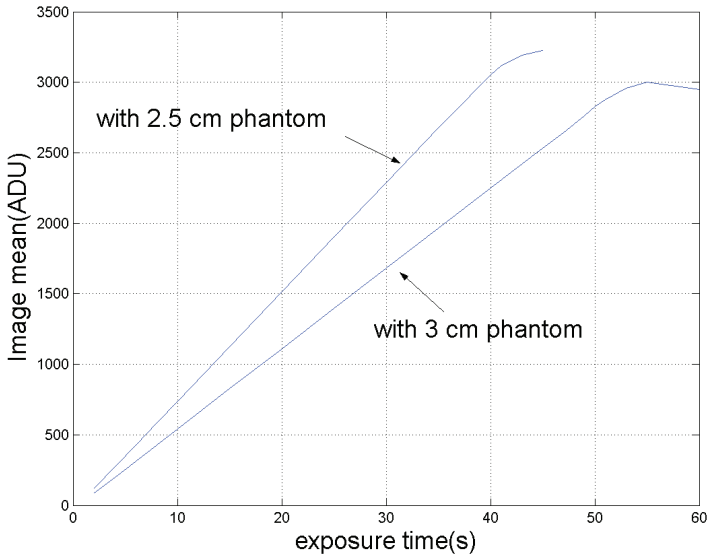

Figure 7.6: Testing the linear response range of the imaging system.

As can be seen in Fig. 7.6, with the 3-cm phantom, the linear response region extends from the very short exposure time (2s) to a long exposure time (50s). With the 2.5-cm phantom, longer exposure time ($> 40s$) makes the system response out of the linear range; with a much thicker phantom, such as a 6-cm phantom, too many x-ray quanta would be attenuated to make the system response at the short exposure time ($2 \sim 4s$) out of the linear range (data not shown). Therefore the 3-cm phantom was utilized in the experiments.

Measurement of the additive noise level

To investigate the level of the additive noise of this x-ray imaging system under prolonged exposures, for each exposure time 50 "additive noise images", which contained no input signal but only additive noise, were acquired. When taking the images, the detector window was covered by 4 1-mm-thick lead sheets in order to prevent the x-ray photons from reaching the detector. Our system calibrations under different conditions showed that there was no x-ray leakages when the lead sheets were used (data not shown). The NPS curves of the "additive noise images" were then obtained.

7.3.4 Experimental results

NPS of the additive noise

The NPS of the additive noise was measured at 26 kVp, 0.3 mA, and with exposure times of 3s, 7s, 9s, 10s, 15s, 20s, 30s, 40s, and 50s. When the exposure time exceeds a certain range, which is 10s in this study, the additive noise increased considerably (Fig. 7.7).

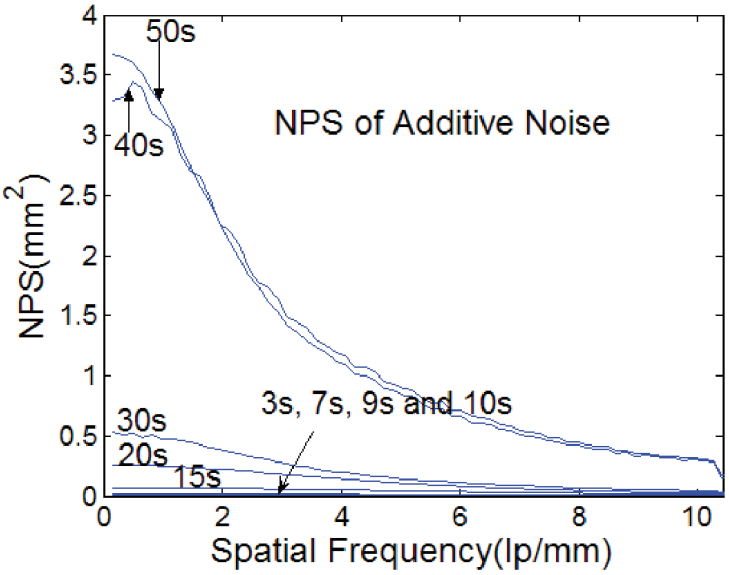

Figure 7.7: NPS(f) for the additive noise at different exposure time at 26 kVp and 0.3 mA, plotted in a linear scale.

To compare the NPS curves of the additive in a more detailed manner, the same data used in Fig. 7.7 was plotted using a base 10 logarithmic scale for the y-axis and a linear scale for the x-axis in Fig. 7.8.

Table 7.1: Comparison of NPS(0) of the additive noise and NPS(0) of the system noise at different exposure time.

Exposure Time (s)	3	7	9	10	15
$NPS_{add}(0)$ (mm^2)	0.0032	0.0088	0.0131	0.0135	0.0663
$NPS_{sys}(0)$ (mm^2)	0.7071	1.8574	2.3541	2.8096	5.4693
$\frac{NPS_{add}(0)}{NPS_{sys}(0)}$ (%)	0.4540	0.4726	0.5547	0.4797	1.2122

Exposure Time (s)	20	30	40	50
$NPS_{add}(0)$ (mm^2)	0.2633	0.5372	3.2858	3.6651
$NPS_{sys}(0)$ (mm^2)	6.1874	9.4831	14.0576	15.6634
$\frac{NPS_{add}(0)}{NPS_{sys}(0)}$ (%)	4.2551	5.6644	23.3740	23.3994

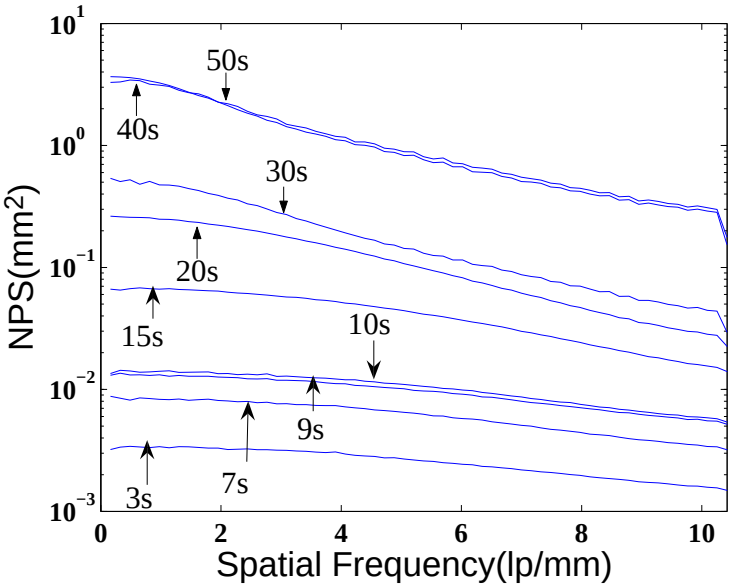

Figure 7.8: NPS(f) for the additive noise at different exposure time at 26 kVp and 0.3 mA. The diagram was plotted using a base 10 logarithmic scale for the y-axis and a linear scale for the x-axis.

NPS at zero frequency at the exposure time of 3s, 7s, 9s, 10s, 15s, 20s, 30s, 40s and 50s are given in Table 7.1. It is shown clearly that within 10s, the values of the zero frequency NPS of the additive noise $NPS_{add}(0)$ are small, but the $NPS_{add}(0)$ increased by a factor of almost 20 from the 10s exposure to the 20s exposure.

Additive noise compared with the system noise

NPS of the entire system, "system noise", were obtained from the output images. The NPS of the system at different exposure times are given in Fig. 7.9, Fig. 7.10, and Fig. 7.11, along with the NPS of the additive noise for comparison. As can be seen, when the exposure time exceeds 10s the additive noise is no longer negligible when compared with the system noise.

In Fig. 7.11, the shape of the NPS curve of the system noise at 50s becomes somewhat different than those in Fig. 7.9 and Fig. 7.10. And this trend can also be noticed in the NPS of the system noise at 20, 30s, and 40s, as shown in Fig. 7.10. A "shoulder" forms gradually in the NPS curves of the system noise from 20s to 50s. Although the detailed reason is not clear, it is apparent that when the exposure time is beyond this range, the system performance becomes degraded.

The ratio of NPS of additive noise to the NPS of the system noise at zero frequency, $NPS_{add}(0)/NPS_{sys}(0)$, is given in Table 7.1. The ratio increased from 0.48% to 4.26% between 10s and 20s. Beyond 20s the additive noise increases rapidly and the system becomes no longer x-ray quantum limited.

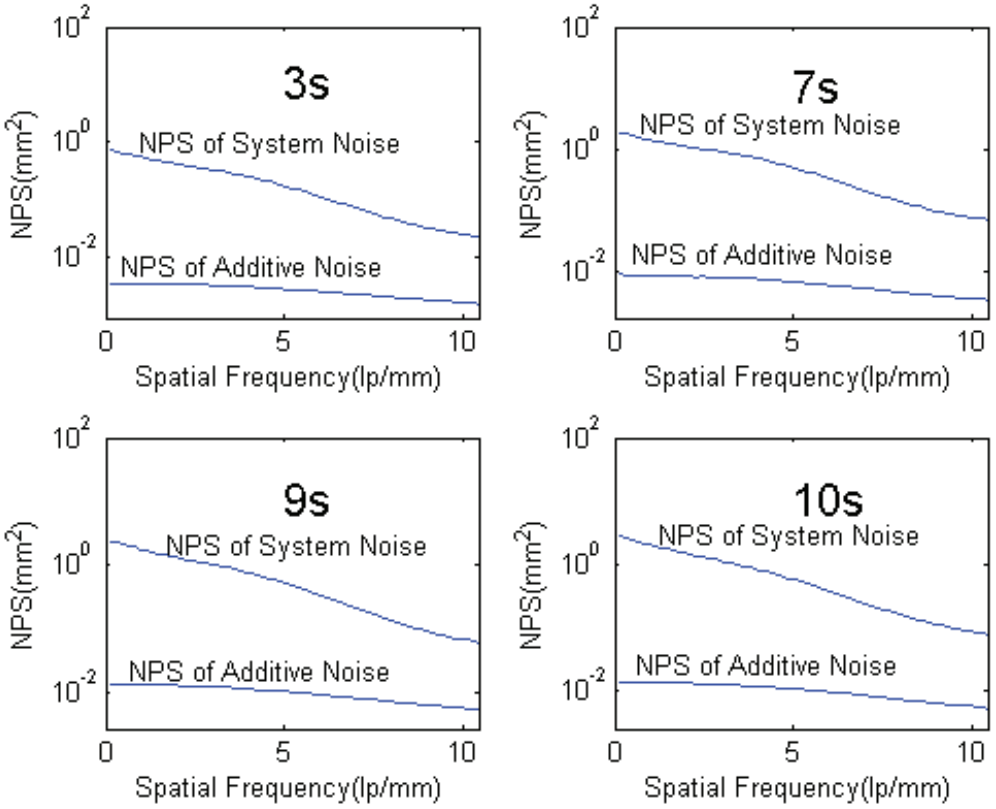

Figure 7.9: NPS of the system noise compared with NPS of additive noise at the exposure time of 3s, 7s, 9s and 10s.

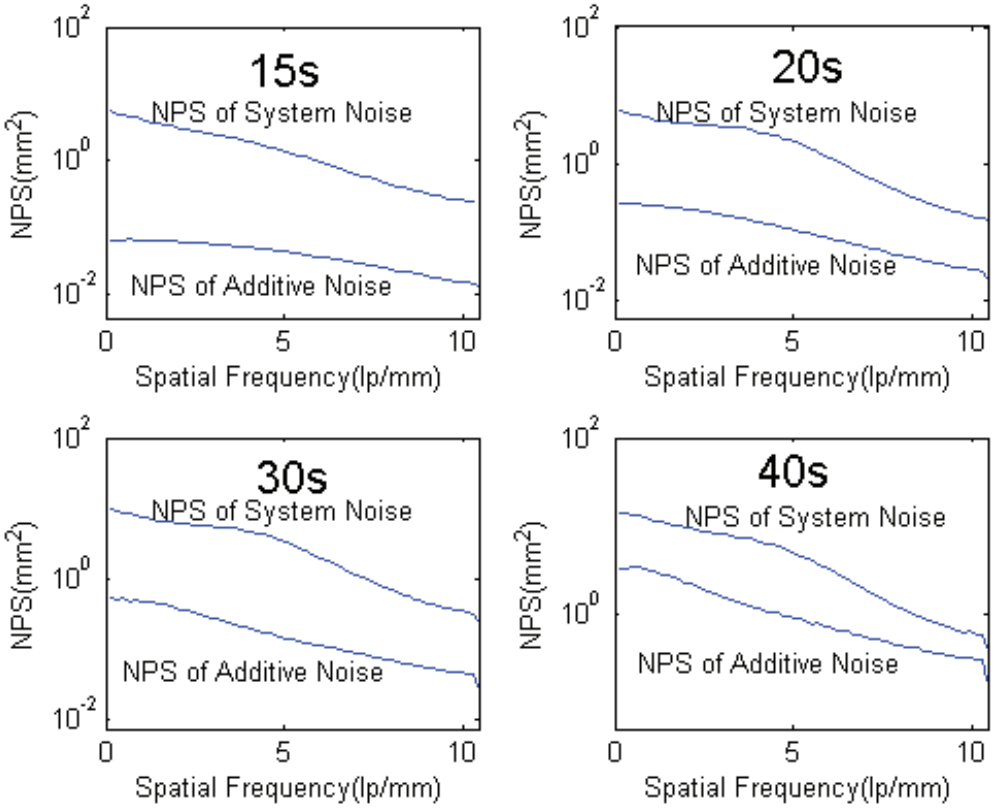

Figure 7.10: NPS of the system noise compared with NPS of additive noise at the exposure time of 15s, 20s, 30s, 40s.

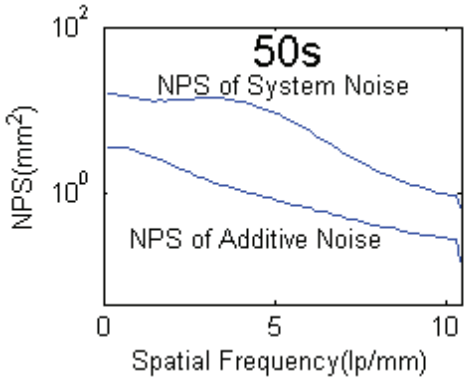

Figure 7.11: NPS of the system noise compared with NPS of additive noise at the exposure time of 50s.

Degraded DQE under Extended Exposure Due to the Rapid Increase of the Additive Noise

In this study, DQE was determined according to Eq. 1.9: $MTF(f)$ in was obtained using the slit camera method introduced in Chapter 6; $NPS(f)$ is acquired using the procedures described in Section 7.2; $S(0)$ was obtained through the spatial average in the region of interest through a series of uniformly exposed images; Φ was calculated by multiplying the radiation dose with the averaged photon fluence per unit radiation. The radiation dose was measured by placing the dose meter (Rad Check Plus Model 06-526, Nuclear Associates) in the center of the beam on the detector plane, and the measured results were calibrated according to the inverse square law. Photon fluence per unit radiation was measured as 4.7904x104 photon/ (mm2-mR) using the method detailed in Chapter 4.

The DQE curves at the exposure time of 3s, 7s, 9s, 10s, 15s, 20s, 30s, 40s and 50s with 26 kVp, 0.3 mA, 3-cm BR-12 filtered beam, are given in Fig. 7.12 and Fig. 7.13. It is also observed in Fig. 7.12 and Fig. 7.13 that there is a significant drop from the DQE at 10s to the DQE at 20s, which is in agreement with the increase in the additive noise from 10s to 20s.

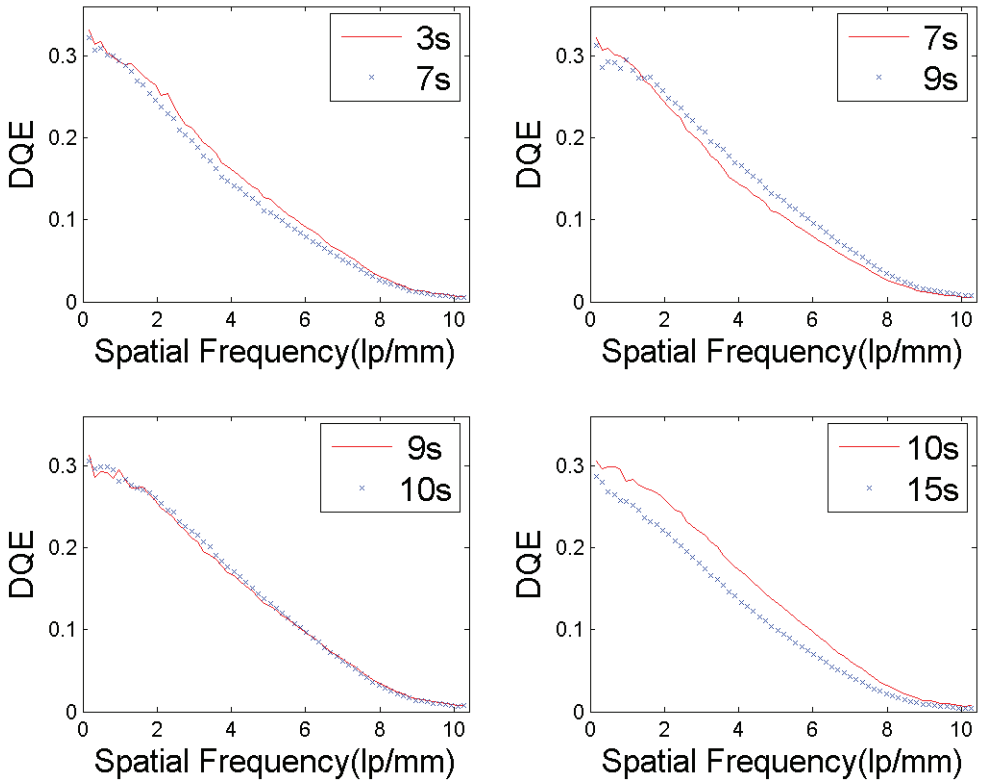

Figure 7.12: Detailed comparisons between DQE curves at the exposure time of 3s, 7s, 9s, 10s and 15s.

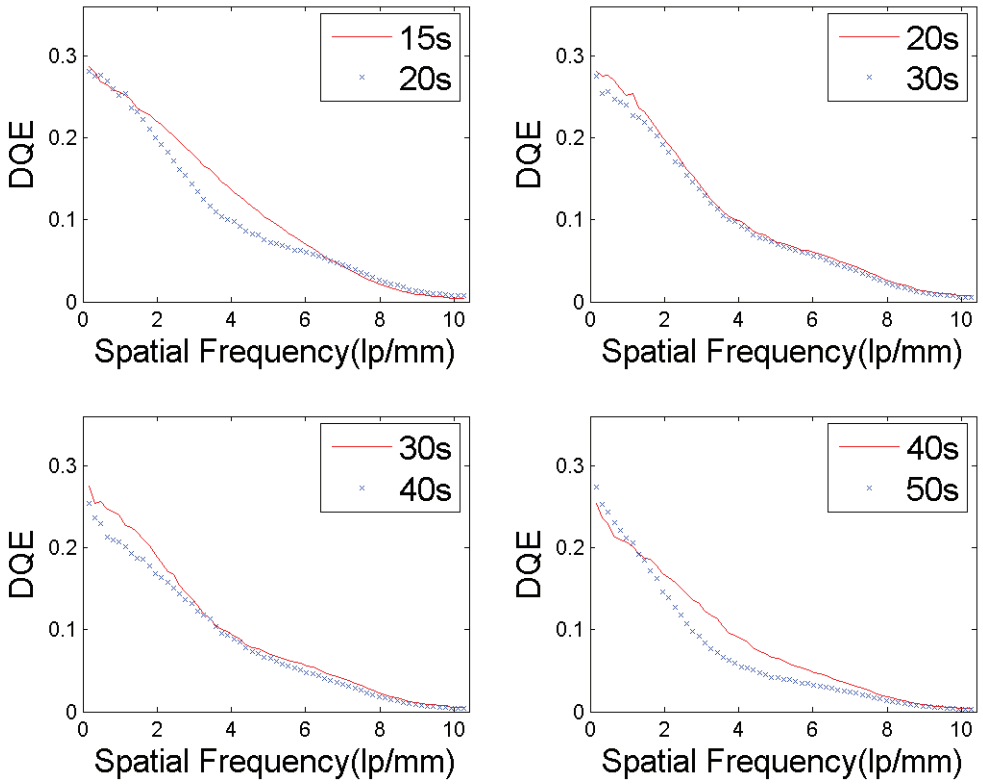

Figure 7.13: Detailed comparisons between DQE curves at the exposure time of 15s, 20s, 30s, 40s and 50s.

7.3.5 Discussion

The impact of additive noise and system noise on the performance of an x-ray imaging system for small animal studies was investigated in this study. The noise power spectra of the additive noise increased with the operating time of the system, due to the noise introduced by the electronic devices in the system, as shown by the NPS curves in Fig. 7.7 and Fig. 7.8. For both the system noise and the additive noise, the NPS at zero frequency is of particular interest because of its largest magnitude; the system performance at lower frequency range is important for evaluating design tradeoffs for electronic X-ray imaging systems [15]. The NPS(0) of different operating times are shown in Table 7.1. The results show that when the operating time exceeds

10 s, the additive noise increases significantly.

Under normal operating conditions, the additive noise should be negligible when compared with the quantum noise which should be the dominant part of the entire system noise according to the X-ray quantum limitation assumption. The comparisons between additive noise and system noise are given in Fig. 7.9, 7.10, and 7.11. Indeed, when the operating time is less than 10 s, the additive noise is rather small (approximately 0.5% at 10s); but when the time is extended beyond 10 s, the contribution from the additive noise becomes significant (approximately 5% at 20 s, 6% at 30 s, 23% at 40 s and 50 s).

The DQE curves obtained at different exposure times fall into two distinctive groups. When the exposure time is less than 10 s, the values of the DQE curves are fairly consistent; the DQE values drop rapidly when the exposure time exceeds a certain point, 10 s in this study, as shown in Fig. 7.12 and Fig. 7.13. When the additive noise is much smaller than the quantum noise, the DQE of the X-ray imaging system is approximately equal to its highest obtainable value (0.26) under current configuration. However, when the additive noise becomes comparable to the quantum noise, which also means that the additive noise is comparable to the system noise, DQE decreases and the system performance was degraded. The DQE curves obtained in our study clearly demonstrated this phenomenon.

7.4 Chapter conclusion

The measurement techniques of NPS are introduced at the beginning of this chapter. The acquisition of NPS involves partitioning the output images into sub-blocks, averaging the NPS calculated from sub-blocks, and generating 1D NPS from 2D NPS, as discussed in Section 7.2. After the description of the general NPS methodology, a NPS-based study on the influence of additive noise on the performance of a CCD-based x-ray imaging system is reported to demonstrate the NPS measurements. The

study investigated the increase of the additive noise, the rise of its proportion in the entire system noise with extended exposure time, and their impact on the system performance. Within a certain range of the exposure time (2 to 10s in this investigation), the additive noise is low and negligible, but when the exposure time exceeds the range (approximately 10s in this study), the additive noise increases rapidly, which causes the x-ray imaging system to be no longer x-ray quantum limited and degrades the system performance. Part of the content of this chapter was published in [11].

CHAPTER 8

DQE analysis on a dual detector phase x-ray imaging system

8.1 Chapter introduction

In the previous chapters the theory of DQE and the measurement techniques of photon fluence, MTF, and NPS have been discussed. An NPS-based investigation about the impact of the additive noise on the performance of a CCD-based x-ray imaging system is also included in the Chapter 7, as an example of the application of the DQE methodology. In this chapter, a DQE analysis that was used to validate the system design of a prototype imaging system is reported, as another example application of the methodology.

This study presents the characterization results of a newly developed dual detector in-line phase x-ray imaging prototype. Phase contrast x-ray imaging and quantitative x-ray phase imaging have drawn increasing popularity in recent years due to their demonstrated improved image quality and extraordinary potential in clinical applications [4, 97–101]. Several studies have been carried out to demonstrate the clinical feasibility of phase imaging [102–106]. Based on a comprehensive theory for clinical x-ray phase imaging [105, 107–109], a dual detector approach has been investigated [80–82]. In this approach, two detectors are aligned with a micro focus x-ray source: detector1 is placed in contact with the object, with a distance R1 from the x-ray source; detector2 is positioned with a distance R2 from detector1 (See figure8.1). During a single x-ray exposure, an attenuation image of the object is acquired on detector1 and a phase contrast image on detector2. The two images are then processed to retrieve a quantitative phase map of the object [80–82].

A prototype was assembled and tested for the parameters such as the logarithm linearity of the detectors and the transmittance of the detector1 under different x-ray techniques [80, 82]. The purpose of this study is to objectively characterize the system based on the DQE methodology: comparisons of MTF, NPS and DQE for both detectors were conducted when they worked in the dual detection mode in which two images are acquired simultaneously at a single exposure.

8.2 Materials and methods

8.2.1 System configuration and experimental setup

The prototype system consists of a micro-focus x-ray source and two computed radiography (CR) detectors. The source, detectors and other imaging and measuring components are mounted on a horizontally placed optical rail, and the positions of the detectors and other components could be adjusted conveniently.

The x-ray source has a Mo-Be target output window combination, and it operates at 20-60kVp with an output power of 10-60W. The focus spot size is around 12-15 μm at 10W and grows to 35-40 μm at 60W [101]. The imaging size and pixel pitch of the CR detectors are $18cm \times 24cm$ and 43.75 μm, respectively. A detailed description of the prototype could be found in [80].

During the MTF, NPS and DQE measurements, the distance from source to detector1 (R1) was fixed at 0.91m (36inch), the distance from detector1 to detector2 (R2) varied among 0.61m (24inch), 0.91m (36inch), 1.22m (48inch), 1.52m (60inch) and 1.83m (72inch), resulting in a magnification factor from 1.67 to 3.0.

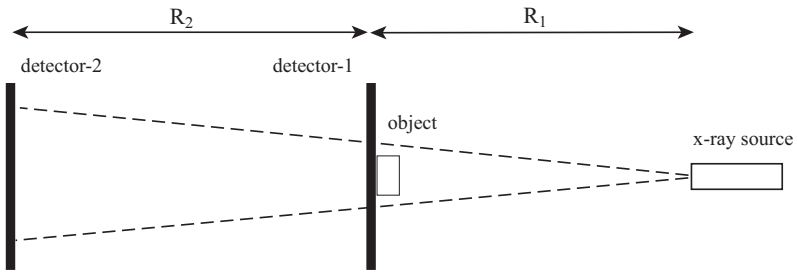

Figure 8.1: The schematic of the dual detector x-ray imaging system. The attenuation-based image is formed on detector1, which is placed in contact with the object. A phase-contrast image is acquired at detector2 which is R2 away from the object. With these two images, phase map of the object may be retrieved.

8.2.2 Exposure, logarithm linearity and data linearization

The mean pixel value (PV) of the output CR images has a logarithm linear relationship with the incident x-ray exposure level:

$$PV = a \cdot log_{10}(Exposure) + b, \tag{8.1}$$

where PV is the mean pixel value.

With the knowledge of the parameter a in equation 8.1, data conversion can be conducted to obtain a linear relationship between the output pixel values and the input exposure level [10, 13, 57]

$$PV'(i,j) = N \cdot 10^{\frac{PV(i,j)-M}{a}}, \tag{8.2}$$

where $PV'(i,j)$ is the resultant pixel value at (i,j), and it is linear to the amount of exposure. M and N are the maximum values of the PV and PV', respectively. For the specific settings in our study, M and N are both set as 4095 because of the 12-bit digitization of the CR system.

The data conversion process is not only of critical importance for phase map

reconstruction [80], but also necessary for MTF, NPS and DQE measurements because all of them assume the system to have a linear input-output relationship [10, 13, 57].

Since the parameters of the logarithm linear relationship depends on the tube voltage and beam spectra [80], measurements of the incident exposure levels and the corresponding mean pixel values were necessary for determining the parameters for each detector and for each beam filtration setting.

Exposure levels were measured with a dosimeter system (Radcal 9095 system, Radcal Corp., Monrovia, CA). An ion chamber (Radcal 10x9-180) was placed with the same distance from the source as the target detector was placed with. For each imaging condition and for each detector, the exposure level was measured 20 times and then averaged to reduce the statistical uncertainty of the measurement. The exposure levels were measured with constant exposure time but different SID for detector2, and with constant SID but different exposure time for detector1.

Table 8.1: Exposure on detector1 with 4 cm thick BR-12 phantom filtered beam at different exposure times. Exposures were taken at 40kVp and 0.5mA, with R1 = 36inch.

exp time (s)	10	15	20	25	30	35
exposure (mR)	3.0	6.5	10.0	13.6	17.1	20.6

Table 8.2: Exposure on detector2 with 4 cm thick BR-12 phantom filtered beam at different SIDs (SID = R1+R2 for detector2). Exposures were taken at 40kVp, 0.5mA, 25s, with R1 fixed at 36inch.

SID (inch)	60	72	84	96	108
exposure (μR)	1591.1	1096.6	798.4	602.7	471.4

The mean pixel values (PV) were obtained by averaging the mean PVs from the central 2048px-by-2048px ROIs of 5 repeatedly acquired images. They were then

plotted against $log_{10}(Exposure)$ and fitted linearly to obtain the parameters in equation 8.1.

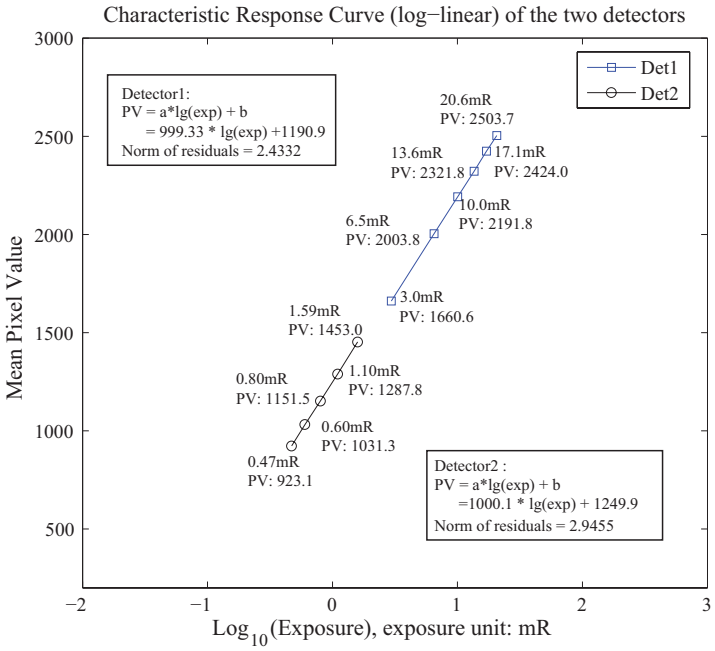

Figure 8.2: Logarithm linear relationship between the incident exposure level and mean pixel values for detector1 and detector2 with the 40kVp, 0.5mA, and 4-cm-thick BR-12 phantom filtered beam.

8.2.3 MTF analysis

MTF were measured under 40kVp and 0.5mA with a 4-cm-thick BR-12 phantom placed right in front of the output window of the tube for both detector1 and detector2, in an effort to examine the blurring effect and the difference in beam quality introduced by detector1 on the image quality of detector2. The beam quality was the same as in the NPS and DQE measurements, and the reason to choose this beam quality will be discussed in Section 8.2.4. $R1$ and $R2$ were all fixed to 36inch (0.91m) during the experiments, resulting in a magnification factor ($M = R1/(R1 + R2)$) of 2, which is a frequently used magnification setting for our phase contrast and phase imaging experiments.

The slit method [16, 39] was employed for the MTF measurement, with the help of a $10\mu m$ wide slit camera (IIE GmbH, Aachen, Germany). The slit camera was placed in contact with each of the CR detectors under evaluation, and was oriented in a near-vertical/subscan or a near-horizontal/scan direction in order to measure the MTF on the horizontal/scan (laser scan) or vertical/subscan (plate scan) direction of the CR system [10, 16]. A lead sheet was placed around the slit to reduce the background level on the resultant images. Before calculation of the MTF, the images were converted

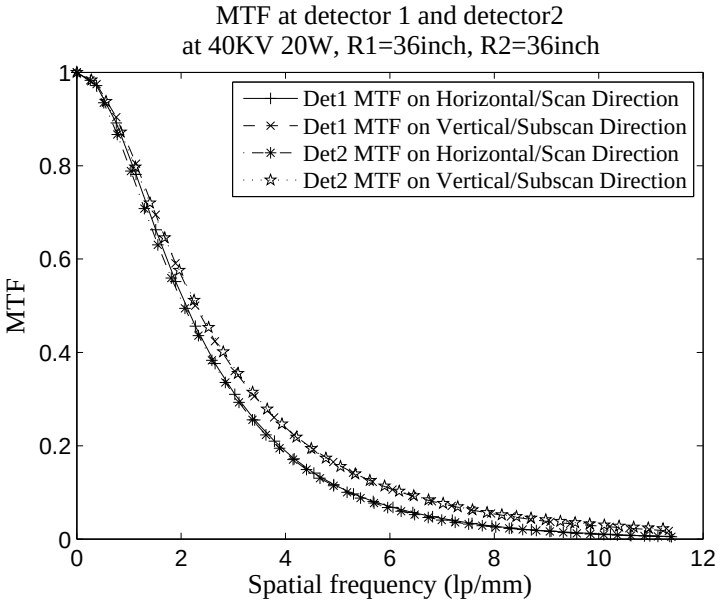

Figure 8.3: System MTF at detector1 and detector2 at configurations of 40kVp, 0.5mA, and 4-cm-thick BR-12 filtered beam

8.2.4 NPS analysis

During the measurements of NPS, exposures of 40kVp, 12.5mAs, and with additional filtration of 4-cm-thick BR-12 phantom were employed for both detector1 and detector2. This combination of the tube potential and beam filtration was chosen for two reasons. Firstly, hardened x-ray could improve the transmittance of detector1 [80], so that detector2 could still receive enough radiation while the entrance exposure

on detector1 was not excessively high. For example, with $R1 = R2 = 36\ inch$, $Exp_{det1} = 13.6mR$, and $Exp_{det2} = 1.1mR$. Secondly, the BR-12 phantom was used to simulate the beam filtration in clinical applications such as mammography. Five NPS measurements were conducted for detector2 with the five aforementioned R2 settings (24, 36, 48, 60 and 72inch), and one NPS measurement was performed for detector1 with R1 = 36inch.

In order to obtain reproducible positioning of the target CR plate between exposures, a specially designed holding device consisting of a supporting bench plate and two one-axis micro-positioning stages was utilized. And it could control the position of the CR detector with a precision of 10 microns on both horizontal and vertical directions. The center of the CR detector was aligned with the center of the x-ray beam, through the help of two laser pointers. In order to reduce back scatter, a 1.6mm-thick lead sheet was spread between the bench plate and the CR plate.

The central portion of 2048 by 2048 pixels on each image was chosen as the region of interest (ROI) for NPS calculations, in order to avoid non-uniformities near the margin area of the CR plates. This ROI was then divided into 256 sub-images of 128 by 128 pixels for the calculation of 2D NPS of each image through [12, 16]:

$$NPS_d(u,v) = \frac{\Delta x^2}{N_x N_y} \left\langle |FT(u,v)|^2 \right\rangle \tag{8.3}$$

where N_x and N_y are the number of pixels on each dimension respectively in the sub-image, which equal to 128 in this study, Δx is the pixel pitch (0.048 mm), and $\left\langle |FT(u,v)|^2 \right\rangle$ is the ensemble average of the squares of the Fourier amplitudes from all the sub-images. Before calculation, the 2048px-by-2048px ROIs were corrected against background trends and fixed pattern noise by flat fielding and background subtraction [44], and for each imaging condition 20 flat images were averaged to obtain the flat-field image.

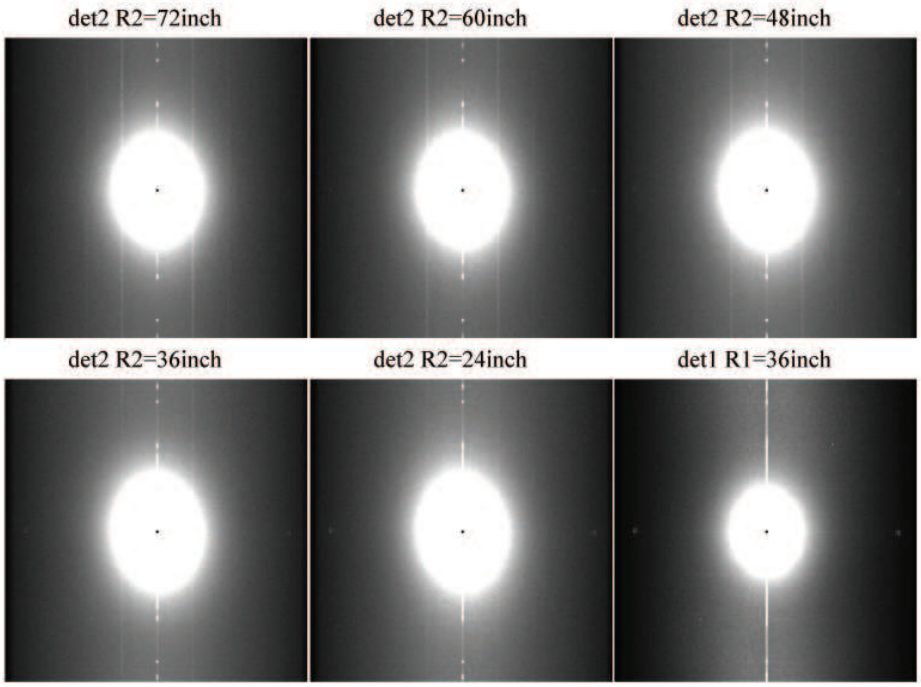

Figure 8.4: 2D NPS of detector1 and detector2 obtained at 40kVp, 12.5mAs, with R1=36inch and R2=24, 36, 48, 60 and 72inch. The beam was filtered by a 4-cm-thick BR-12 phantom. The same contrast enhancement technique with same parameters was applied to the 2D NPS images to improve the visibility.

Furthermore, twenty images were obtained for each exposure setting, and NPS results calculated from each image were then averaged to get the final NPS result for the corresponding exposure settings. Therefore altogether $256 \times 20 = 5120$ ensembles of 2D NPS were averaged for each exposure setting, in an effort to reduce the statistical variance of the NPS results. 1D NPS on scan and subscan directions of the CR system were obtained by averaging the 2D NPS data points on thick slices which are parallel and immediately adjacent to the axes [12, 13, 16, 32, 43].

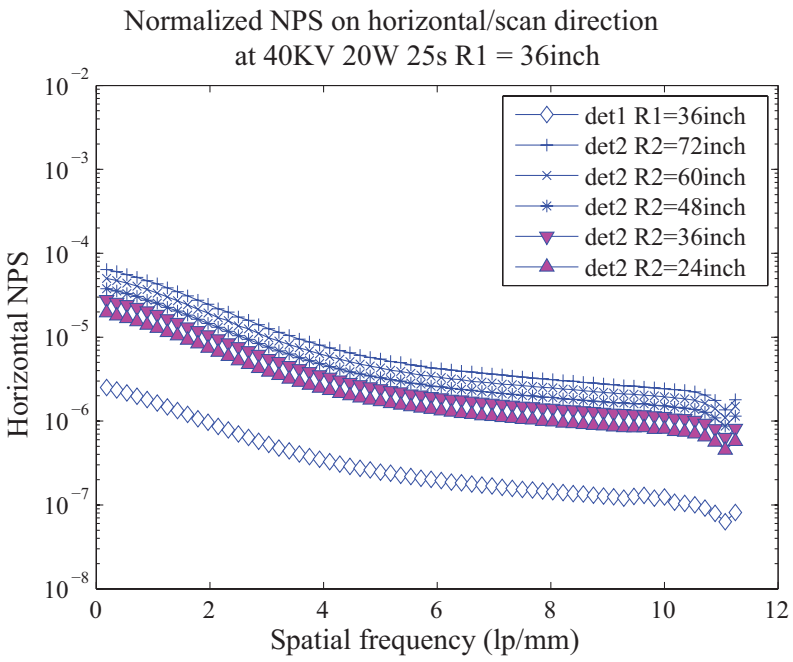

Figure 8.5: Normalized NPS of detector1 and detector2 on scan direction. The measurements were taken with the 40kVp, 12.5mAs, and 4-cm-thick BR-12 phantom filtered beam. R1=36inch and R2=24, 36, 48, 60 and 72inch. Each NPS curve was normalized by the square of the corresponding large area signal (mean pixel value of the images).

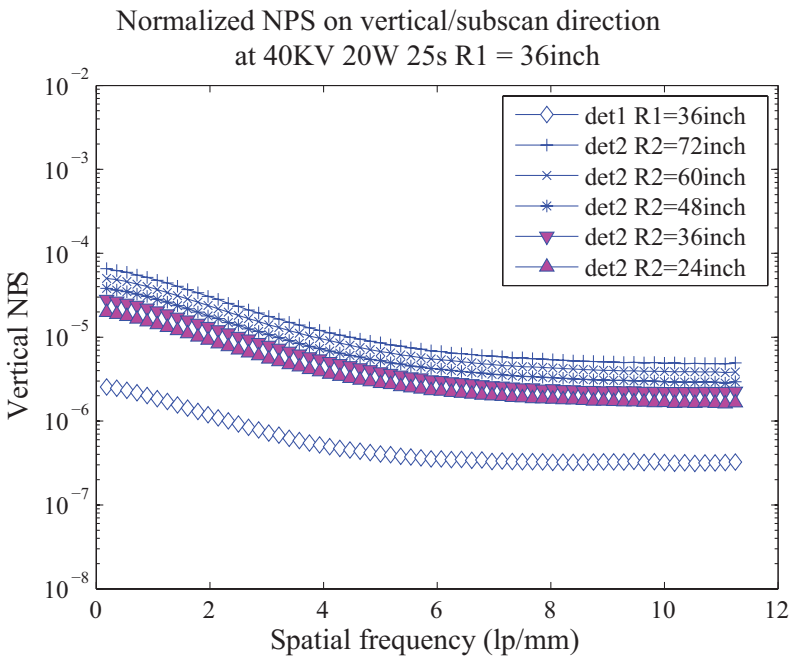

Figure 8.6: Normalized NPS of detector1 and detector2 on subscan direction. The measurements were taken with the 40kVp, 12.5mAs, and 4-cm-thick BR-12 phantom filtered beam. R1=36inch and R2=24, 36, 48, 60 and 72inch. Each NPS curve was normalized by the square of the corresponding large area signal (mean pixel value of the images).

8.2.5 Incident spectra and photon fluence per unit exposure

In order to examine beam filtration effect of detector1, the incident spectra on detector1 and detector2 were measured and compared with the aid of a spectrometer (Amptek Inc., MA). The photon fluence per unit exposure on detector1 and detector2 were then calculated based on the measured x-ray spectra for further DQE calculations [32, 43]. The photon fluence per unit radiation was measured as 56747 $photon/(mm^2 \cdot mR)$ for detector1, and 63203 $photon/(mm^2 \cdot mR)$ for detector2. This number is higher for detector2 because the beam incident on detector2 is harder than that on detector1, due to the additional filtration introduced by detector1.

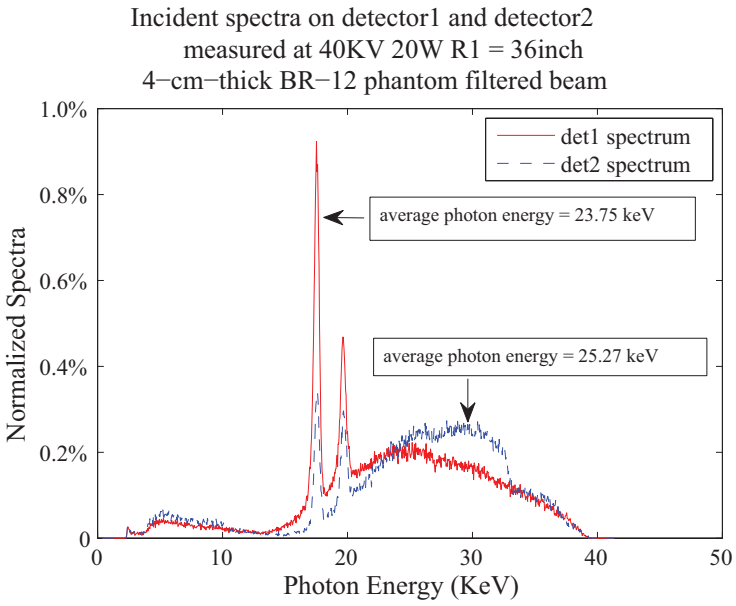

Figure 8.7: Incident spectra on detector1 and detector2 with the 40kVp, 0.5mA, and 4-cm-thick BR-12 phantom filtered beam. Each spectrum was normalized by their total number of counts.

8.2.6 DQE Analysis

Based on the results of MTF, NPS, and exposure and incident x-ray spectra, DQE was determined by [8, 11, 15, 16]:

$$DQE(f) = \frac{S(0)^2 \cdot MTF(f)^2}{NPS(f) \cdot q}, \tag{8.4}$$

where S(0) is the large area signal, and it is the mean pixel value of the output images in the NPS measurement. MTF(f) and NPS(f) are the modulation transfer function and noise power spectrum, respectively. q is the number of x-ray quanta per mm^2 at the detector input, which was calculated by multiplying the exposure with the photon fluence per unit exposure.

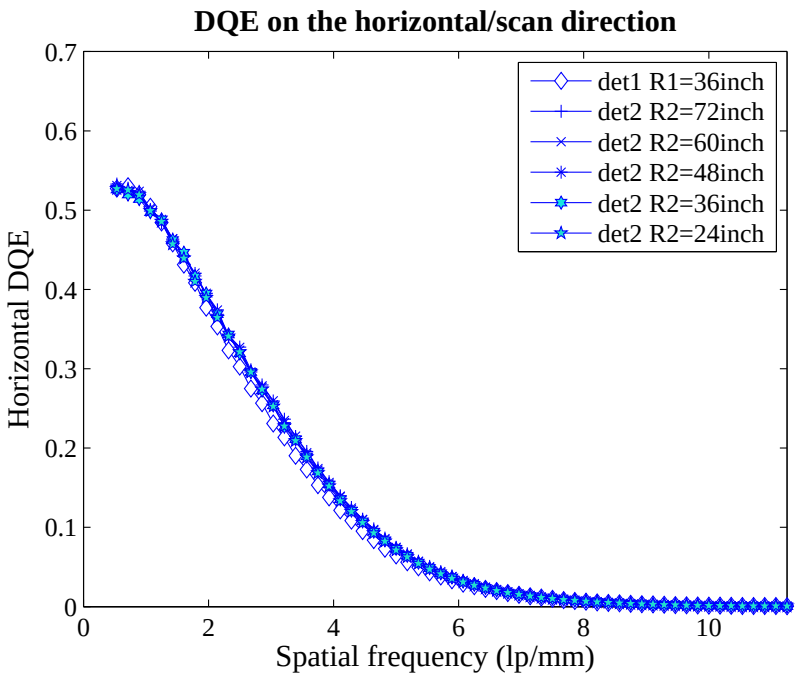

Figure 8.8: DQE on scan direction for detector1 and detector2 at 40kVp 12.5mAs with R1=36inch and R2=24, 36, 48, 60 and 72inch. The beam was filtered by a 4-cm-thick BR-12 phantom.

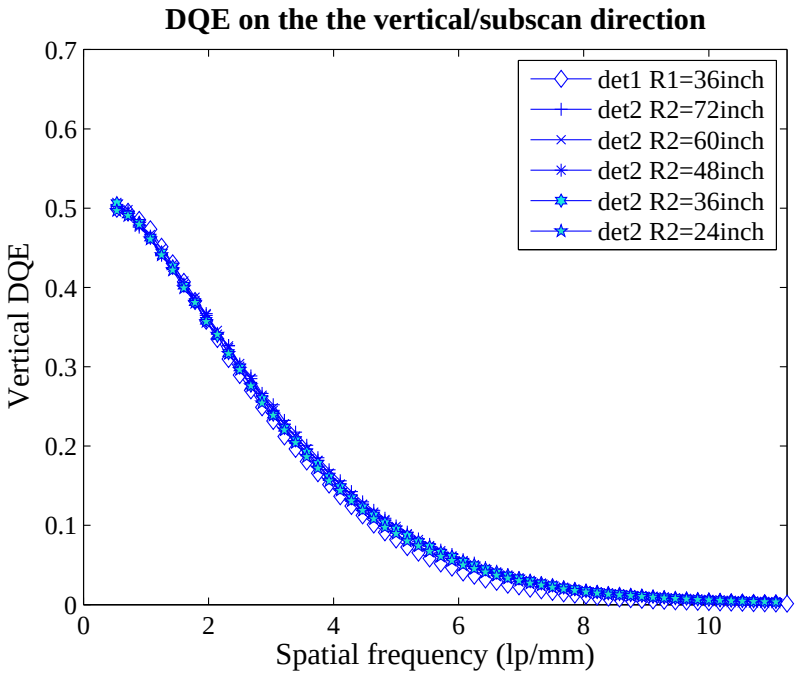

Figure 8.9: DQE on the sub scan direction for detector1 and detector2 at 40kVp, 12.5mAs, with R1=36inch and R2=24, 36, 48, 60 and 72inch. The beam was filtered by a 4-cm-thick BR-12 phantom.

8.3 Results and discussions

Table 8.1 and Table 8.2 show the entrance exposure levels on detector1 and detector2 with the 40kVp, 4-cm-thick BR-12 filtered beam. Each data point in table 8.1 and table 8.2 was the mean of 20 measurements. The sample standard deviations of the measurements are all below 1% of the corresponding exposures, and therefore the relative standard deviations for all the mean exposures are below 0.05%. The exposure measurements were then used to determine the logarithm linearity parameters, as shown in figure 8.2. The measured data in Table 8.2 do not perfectly match the calculated exposure value according to the inverse square law, and this is probably due to the variation of measurements at low exposure level.

The transmittance of detector1 was determined as approximately 32% based on

the entrance exposures on the two detectors:

$$transmittance = exp_2 \cdot M^2/exp_1 = 1.1 \times 2^2/13.6 \approx 0.32 \tag{8.5}$$

where $M = (R1 + R2)/R1$ is the magnification factor, exp_1 and exp_2 are the entrance exposure levels on detector1 and detector2, respectively. The exposure levels used in this calculation was acquired at R1=R2=36inch. Similar result can be obtained using other R1 and R2 settings.

The logarithm linearity curves of the CR detectors at the 40kVp, 4-cm-thick BR-12 phantom filtered beam are shown in figure 8.2. As can be observed, the two curves demonstrated high similarity. However, it should be noted that the logarithm linearity at other beam filtration and kVp settings can be significantly different those in figure 8.2. For example, for a 40kVp x-ray beam without added filtration, the logarithm linearity is: $PV = 1180.5lg(exp) + 216.91$. The similarity between the logarithm linearity for detector1 and detector2 in figure 8.2 shows that the two detectors worked in a consistent manner, which could be attributed to the similar incident spectral shapes (in figure 8.7), as a result of the beam hardening introduced by the BR-12 phantom before the beam reached the two detectors.

The MTFs of detector1 and detector2 at 40kVp, 0.5mA, 4-cm-thick BR-12 filtered beam and with R1=R2=36inch are presented in figure 8.3. For both detectors, the MTF curves on scan (horizontal) direction are lower than those on subscan (vertical) direction. The difference between MTFs on the two directions is probably due to the slight difference between the sampling distances on the two directions. Similar observations were also found in previous studies [11, 16]. One can see that the MTFs of the two detectors on both directions are almost identical (with difference less than 0.01). The MTF of detector2 with other R2 settings were not measured, since we considered that different SIDs under our experimental settings do not cause much

difference in the MTFs of the detector2, which was based on our previous experimental results of detector2's MTF at different SIDs under 40kVp 0.25mA with R1=24inch and R2=24, 36, 42 and 60inch.

Fig. 8.5 and 8.6 manifested the normalized NPS curves ($NPS/(LAS)^2$) on scan (horizontal) direction and subscan (vertical) direction. LAS stands for large area signal, which is calculated as the mean pixel value of the images. The noise power spectra were obtained with the 40kVp, 12.5mAs, 4-cm-thick BR-12 phantom filtered beam. R1 was fixed as 36inch, while R2 changed from 24inch to 72inch. Since the entrance exposure levels were different for the above conditions, the normalized NPS varied in their scales. The NPS curves on subscan direction showed a bigger tail at high frequencies than the NPS curves on scan direction: for instance, the normalized NPS of detector2 on scan direction with R2=24inch reaches 1.0×10^{-5} at 1.5 lp/mm, compared to 1.8 lp/mm for the NPS on subscan direction; at 10 lp/mm, the normalized NPS on the scan direction has a value of 8.05×10^{-7}, while the one on the subscan direction has a value of 1.67×10^{-6}. As can be seen from the 2D NPS images (figure 8.4), the background near the vertical axis is brighter than that near the horizontal axis. And the asymmetric shape of the 2D NPS results coincides with the asymmetric MTFs of the CR detectors. The artifacts observed on the horizontal and vertical axes correspond to the stripes-like structural noise of the CR detectors. Two bright lines were found parallel to the vertical axis on the 2D NPS of detector2 but not on detector1. This phenomenon might be explained as the structural noise represented by the bright lines was present on the 2D NPS of both detectors but they were drowned out by the much brighter background on the 2D NPS of detector1.

Fig. 8.7 shows the incident x-ray spectra obtained for both detector1 and detector2 with the 40kVp, 4-cm-thick BR-12 filtered beam. The effect of beam hardening of detector1 can be seen directly by comparing the two spectra. The average x-ray photon energy was 23.75 keV on detector1 and was increased to 25.27 keV on

detector2.

DQE curves of detector2 obtained with different R2 settings almost overlapped together in figure 8.8 and 8.9. The high level of agreement among these DQE measurements indicates that the performance of detector2, in respect of the efficiency of x-ray photon utilization, is stable with the five different R2 settings and the corresponding exposure levels. All of the DQE curves had a top value ranging from 50 $\sim$ 53% at very low frequency (0.5 lp/mm), and dropped to 10% at about 5 lp/mm. The consistency of the DQE curves again indicates similar and well behaved imaging performance of both detectors in respect of the efficiencies of x-ray photon utilization.

8.4 Chapter conclusion

In this chapter, the imaging characteristics of a uniquely designed dual detector phase imaging prototype was investigated, as an example application of the DQE methodology.

The selection of CR for detector1 is critical in the design of the prototype system, and it allows the x-ray photons exiting from detector1 to be recorded by detector2 [80–82]. With this design, both attenuation-based and phase-contrast-based images can be acquired simultaneously at a single exposure. As compared with taking multiple separate exposures for attenuation and phase contrast images, this dual detection technique could potentially reduce patient dose and avoid motion blurs and other errors that may be introduced by multiple exposures. One of the key considerations in this dual detector configuration is to make sure the entrance exposure on both detectors are large enough to ensure that both detectors operate in x-ray quantum noise limited condition and with equivalent imaging performance. Therefore, measurements including the entrance exposure level, logarithm linearity, MTF, NPS, incident spectra, and DQE were conducted and compared for both detectors when they worked in the dual detection mode. Through experimental trials, a 40kVp,

12.5mAs, and 4-cm-thick BR-12 filtered beam settings was determined to be satisfactory, under which the detector1's transmittance was about 32%, resulting in an exposure levels of 13.6mR on detector1 and exposures from 0.5mR to 1.6 mR on detector2 for the five different R2 settings.

The characteristic responses of the two detectors are highly agreed, showing that they worked in a similar manner. Furthermore, the MTF of the two detectors showed only slight difference of about $0.01 \sim 0.02$, implying that the blurring introduced by detector1 did not weaken the resolving power of detector2 significantly. The DQE values for the two detectors at very low frequency (≈ 0.5 lp/mm) are all above 50%, showing a highly efficient utilization of x-ray photons in the imaging processes. The DQE curves on detector2 with the five R2 settings almost coincide exactly, which means that an elongated R2 and the resultant reduced exposure levels did not degrade the imaging performance significantly under the experimental settings. The DQE curves of detector1 also demonstrated appreciable agreement with those of detector2, which indicates similar system performance of both detectors and implies both detectors operating in quantum noise limited condition. And the settings of kVp, mA, exposure time, and beam filtration utilized in this study can be employed as a guideline for future experimental designs of quantitative phase imaging based on the dual detector system.

In summary, the experiments and measurements in this study validated the design of the dual detector system for x-ray phase imaging, which has potential for improving the accuracy of diagnostics at clinically acceptable radiation dose. Part of the content of this chapter was published in [41] and [82].

CHAPTER 9

Summary

The primary objective of the research of this dissertation is to investigate the theory, the measurement techniques and the applications of Detective Quantum Efficiency (DQE) for digital x-ray imaging systems. DQE is widely accepted as the "golden rule" for objectively evaluating the performances of x-ray based medical imaging systems. DQE combines several important image-quality-related measurements such as contrast, resolution, and noise, and measures the efficiency of the utilization x-ray photons in the imaging process.

In order to clarify several confusing aspects of the current DQE methodology as stated in Chapter 1, the theory of DQE is re-derived in Chapter 2, based on the conditions of digital x-ray imaging. As compared with the traditional DQE theory that is originally established on a continuous and analogue foundation, the newly derived DQE theory is established on the theories of digital signal processing and discrete stochastic processes.

In Chapter 2, the theory of DQE for linear digital x-ray imaging systems was derived based on 2D DTFT. The imaging system is considered as a black box with signal power spectrum and noise power spectrum both the input end and the output end. By applying the theory of power spectrum density analysis for linear systems, DQE could be expressed as the ratio between the input signal-to-noise spectrum and the output signal-to-noise spectrum. As compared with the traditional interpretation of DQE as the ratio between the output SNR spectrum and the input SNR (a scalar), this newly derived DQE is more theoretically solid. Through the derivation, the issue

of frequency resolution in the DQE measurements can be explained clearly, as shown in Chapter 2. Given a limited amount of image data, there is a trade-off between the statistical variance of the NPS and DQE resultant spectra and the frequency resolution of the spectra: if a small cutting window is used to obtain the ROI for the NPS calculation, more NPS spectra can be averaged to reduce statistical variance in the final NPS, but at the cost of lower frequency resolution of the NPS curve. Zero-padding can be utilized to increase the frequency sampling rate, and therefore improves the frequency resolution. If the spectra are smooth in nature, it is preferable to use a smaller sub-image size with zero-padding to obtain high frequency resolution as well as small statistical variance in the spectra. At the end of Chapter 2, the assumptions and conditions employed in this derivation of the DQE theory were emphasized, and several methodological suggestions were made in an effort to guide the implementation of the DQE measurements.

After the introduction of the general DQE theory in Chapter 2, several aspects of the DQE measurement are discussed respectively in the following chapters. The measurement techniques of DQE in magnification radiography are introduced in Chapter 3, the estimation of x-ray photon fluence and the x-ray spectral measurements are discussed in Chapter 4. An error analysis on the propagation of the calibration uncertainty in x-ray spectral measurements and photon fluence estimation is also investigated in Chapter 4, in an effort to improve the accuracy of the photon fluence measurements. Moreover, an innovative alignment procedure designed to reduce the measurement error in the spectral measurement and imaging experiments is introduced in Chapter 5. Measurement techniques for MTF and NPS are detailed in Chapter 6, and in the first part of Chapter 7, respectively.

Two example studies based on the DQE methodology are included after the discussions on the measurement techniques. In Chapter 7, the influence of additive noise on the performance of a CCD-based x-ray imaging system is investigated based

on NPS and DQE measurements. The NPS of the additive noise of this system, particularly the growth trend of the additive noise with exposure time, was investigated. Moreover, DQE of the system was measured and the threshold exposure time beyond which the quantum noise limited condition is violated was also determined. In Chapter 8, the characterization results of a newly developed dual detector in-line phase x-ray imaging prototype is presented. Comparisons of MTF, NPS and DQE for both detectors were conducted when they worked in the dual detection mode in which two images are acquired simultaneously at a single exposure. The resultant MTF and DQE curves of the two detectors are in good agreement, showing that the two detectors have similar imaging performance under the imaging conditions of the study. The study answered the key question that if both detectors could operate with equivalent imaging performance, and validated the design of the dual detection configuration for the phase x-ray imaging.

The next steps in the research of the DQE methodology may involve two different aspects. The first aspect is to apply uncertainty analysis to the measurement of MTF and NPS, and to establish a complete uncertainty measurement for the DQE spectra, by combing them with the uncertainty analysis on the photon fluence measurements. The challenges in this aspect lie in the fact that the uncertainty for spectra that are generated following complex procedures is very difficult to analyze theoretically and numerically, and that there is no such standard to follow. The second aspect is to apply the DQE concept and method to x-ray phase imaging. The challenges on this direction is that the imaging mechanism of phase x-ray imaging is completely different from attenuation-based x-ray imaging, and the underlying assumptions and theoretical foundations for applying the DQE in this application need to be carefully investigated.

Bibliography

[1] D. G. Darambara, A. Taibi, R. D. Speller, and M. Gambaccini, "Contrast-detail evaluation of a full-field digital mammography system," *IEEE Transactions on Nuclear Science*, vol. 47, no. 3, pp. 870–876, 2000.

[2] M. Sandborg and G. A. Carlsson, "Influence of X-ray energy spectrum, contrasting detail and detector on the signal-to-noise ratio (SNR) and detective quantum efficiency (DQE) in projection radiography," *Physics in Medicine and Biology*, vol. 37, pp. 1245–1263, June 1992.

[3] B. Hasegawa, *The Physics of Medical X-Ray Imaging.* Madison, Wisconsin: Medical Physics Publishing Company, 1990.

[4] M. Donovan, D. Zhang, W. R. Chen, and H. Liu, "The characterization of a phase contrast x-ray imaging prototype," in *Complex Dynamics and Fluctuations in Biomedical Photonics IV*, V. V. Tuchin, Ed., vol. 6436. SPIE, 2007, p. 643608.

[5] R. E. Hendrick, L. Bassett, M. A. Botsco, P. F. Butler, G. D. Dodd, S. Feig, J. Gray, A. Haus, M. A. Harvey, R. Heinlein, R. Holland, E. L. K. Jr., R. McLelland, J. McCrohan, R. Rossi, and D. C. Sullivan, *Mammography Quality Control Manual*, revised ed. American College of Radiography, 1994, pp. 43–51.

[6] J.T.Bushberg, J.A.Seibert, E. Jr., and J.M.Boone, *The Essential Physics of Medical Imaging*, 2nd ed. Philadephia: Lippincott Williams and Wilkins, 2002, pp. 31–60, 255–291.

[7] A. Macovski, *Medical imaging systems.* Englewood Cliffs, N.J.: Prentice-Hall, Inc., 1983, pp. 8–21, 36–59, 63–73, 75–102.

[8] J. C. Dainty and R. Shaw, *Image Science.* New York: Academic Press, 1974, pp. 1–32, 152–188, 190–229, 232–273, 276–317.

[9] R. N. Bracewell, *Fourier Analysis and Imaging.* New York: Kluwer Academic/Plenum Publishers, 2003, pp. 150, 195, 280, 560–620.

[10] D. Zhang, J. Rong, R. Chu, X. Z. Wu, and H. Liu, "Imaging characteristics of a high resolution computed radiography system," *Journal of X-Ray Science and Technology*, vol. 14, no. 4, pp. 273–282, 2006.

[11] D. Zhang, J. Rong, W. R. Chen, F. Gao, K. X. Xu, X. Z. Wu, and H. Liu, "Impact of additive noise on system performance of a digital x-ray imaging system," *IEEE Transactions on Biomedical Engineering*, vol. 54, no. 1, pp. 69–73, 2007.

[12] H. Y. Jiang, W. R. Chen, and H. Liu, "Techniques to improve the accuracy and to reduce the variance in noise power spectrum measurement," *IEEE Transactions on Biomedical Engineering*, vol. 49, no. 11, pp. 1270–1278, 2002.

[13] M. J. Flynn and E. Samei, "Experimental comparison of noise and resolution for 2k and 4k storage phosphor radiography systems," *Medical Physics*, vol. 26, no. 8, pp. 1612–1623, 1999.

[14] M. B. Williams, P. A. Mangiafico, and P. U. Simoni, "Noise power spectra of images from digital mammography detectors," *Medical Physics*, vol. 26, no. 7, pp. 1279–1293, 1999.

[15] H. Liu, L. Fajardo, and B. Penny, "Signal-to-noise ratio and detective quantum efficiency analysis of optically coupled CCD mammography imaging systems," *Academic Radiology*, vol. 3, no. 10, pp. 799–805, 1996.

[16] J. T. Dobbins, D. L. Ergun, L. Rutz, D. A. Hinshaw, H. Blume, and D. C. Clark, "DQE(f) of four generations of computed radiography acquisition devices," *Medical Physics*, vol. 22, no. 10, pp. 1581–1593, 1995.

[17] R. M. Nishikawa and M. J. Yaffe, "Signal-to-noise properties of mammographic film–screen systems," *Medical Physics*, vol. 12, no. 1, pp. 32–39, 1985.

[18] A. D. A. Maidment and M. J. Yaffe, "Analysis of the spatial-frequency-dependent DQE of optically coupled digital mammography detectors," *Medical Physics*, vol. 21, no. 6, pp. 721–729, 1994.

[19] R. M. Nishikawa and M. J. Yaffe, "Model of the spatial-frequency-dependent detective quantum efficiency of phosphor screens," *Medical Physics*, vol. 17, no. 5, pp. 894–904, 1990.

[20] J. M. Sandrik and R. F. Wagner, "Absolute measures of physical image quality: Measurement and application to radiographic magnification," *Medical Physics*, vol. 9, no. 4, pp. 540–549, 1982.

[21] J. Marple S. Lawrence, *Digital Spectral Analysis*. Englewood Cliffs, NJ: Prentice Hall, 1987, pp. 432–461.

[22] M. B. Priestley, *Spectral Analysis and Time Series*. London,UK: Elsevier Academic Press, 1983, pp. 100–179, 184–285, 389–449, 502–612, 654–726.

[23] K. S. Shanmugan and A. M. Breipohl, *Random Signals: Detection, Estimation and Data Analysis*. Ontario, Canada: John Wiley & Sons, 1988, pp. 110–204, 216–244, 560–615.

[24] J. T. D. III, "Effects of undersampling on the proper interpretation of modulation transfer function, noise power spectra, and noise equivalent quanta of digital imaging systems," *Medical Physics*, vol. 22, no. 2, pp. 171–181, 1995.

[25] S. M. Kay, *Modern Spectral Estimation: Theory and Application.* Englewood Cliffs, NJ: Prentice Hall, 1988, pp. 51–60, 479–526.

[26] A. Papoulis, *Probability, random variables, and stochastic processes*, 4th ed. New Delhi: Tata McGraw-Hill Publishing Company Limited, 2002, pp. 371–434, 499–521, 523–576.

[27] D. Zhang, J. Rong, C. R., W. R. Chen, and L. Liu, "DQE measurements in magnification x-ray imaging," *Journal of X-Ray Science and Technology*, vol. 14, no. 2, pp. 141–150, 2006.

[28] R. M. Nishikawa, G. E. Mawdsley, A. Fenster, and M. J. Yaffe, "Scanned-projection digital mammography," *Medical Physics*, vol. 14, no. 5, pp. 717–727, 1987.

[29] R. Shaw, "Review: Evaluating the efficiency of imaging processes," *Reports of Progress in Physics*, vol. 41, pp. 1103–1155, July 1978.

[30] C. E. Dick and J. W. Motz, "Image information transfer properties of x-ray fluorescent screens," *Medical Physics*, vol. 8, no. 3, pp. 337–346, 1981.

[31] P. R. Granfors and R. Aufrichtig, "Performance of a 41 x 41-cm amorphous silicon flat panel x-ray detector for radiographic imaging applications," *Medical Physics*, vol. 27, no. 6, pp. 1324–1331, 2000.

[32] W. Hillen, U. Schiebel, and T. Zaengel, "Imaging performance of a digital storage phosphor system," *Medical Physics*, vol. 14, no. 5, pp. 744–751, 1987.

[33] N. Mohanty, *Random Signals estimation and identification.* New York: Van Nostrand Reinhold Company Limited, 1986, pp. 109–197, 319–396.

[34] I. A. Cunningham and R. Shaw, "Signal-to-noise optimization of medical imaging systems," *J. Opt. Soc. Am. A*, vol. 16, no. 3, pp. 621–632, 1999.

[35] IEC, *Medical electrical equipment - Characteristics of digital X-ray imaging devices - Part 1: Determination of the detective quantum efficiency*, IEC 62220-1 ed. Geneva, Switzerland: International Electrotechnical Commission, 2003.

[36] S. K. Mitra, *Digital Signal Processing: A Computer-Based Approach*, 2nd ed. New York: McGraw-Hill Companies, Inc., 2001, pp. 117–140, 300–305, 758–779.

[37] R. Shaw, "The equivalent quantum efficiency of the photographic process," *Journal of Photographic Science*, vol. 11, pp. 199–204, 1963.

[38] R. C. Jones, "On the quantum efficiency of photographic negatives," *Photographic Science and Engineering*, vol. 2, no. 2, pp. 57–65, 1958.

[39] H. Fujita, D. Y. Tsai, T. Itoh, K. Doi, J. Morishita, K. Ueda, and A. Ohtsuka, "A simple method for determining the modulation transfer-function in digital radiography," *IEEE Transactions on Medical Imaging*, vol. 11, no. 1, pp. 34–39, 1992.

[40] S. K. Mitra, A. S. Willsky, and S. H. Nawab, *Signal and Systems*, 2nd ed. N.J.: Pearson Education Inc., 2002.

[41] D. Zhang, H. Liu, and X. Wu, "DQE analysis on a dual detector phase x-ray imaging system," *Physics in Medicine and Biology*, vol. 53, no. 18, pp. 5165–5176, 2008.

[42] D. Zhang, M. Donovan, X. Wu, and H. Liu, "A convenient alignment approach for x-ray imaging experiments based on laser positioning devices," *Medical Physics*, vol. 35, no. 11, pp. 4907–4910, 2008.

[43] S. Vedantham, A. Karellas, S. Suryanarayanan, D. Albagli, S. Han, E. J. Tkaczyk, C. E. Landberg, B. Opsahl-Ong, P. R. Granfors, I. Levis, C. J. D'Orsi, and R. E. Hendrick, "Full breast digital mammography with an amorphous silicon-based flat panel detector: Physical characteristics of a clinical prototype," *Medical Physics*, vol. 27, no. 3, pp. 558–567, 2000.

[44] A. Karellas, L. J. Harris, H. Liu, M. A. Davis, and C. J. D'Orsi, "Charge-coupled device detector: Performance considerations and potential for small-field mammographic imaging applications," *Medical Physics*, vol. 19, no. 4, pp. 1015–1023, 1992.

[45] A. E. Burgess and K. Humphrey, "Visual-perception limits in angiography," *Optical Engineering*, vol. 17, no. 4, pp. 400–406, 1978.

[46] E. P. Muntz, "On the comparison of actual and calculated improvements in the imaging of calcifications using magnification mammography," *Medical Physics*, vol. 8, no. 4, pp. 496–501, 1981.

[47] C. C. Shaw, X. Liu, M. R. Lemacks, J. X. Rong, and G. J. Whitman, "Optimization of MTF and DQE in magnification radiography: a theoretical analysis," J. T. D. III and J. M. Boone, Eds., vol. 3977, no. 1. SPIE, 2000, pp. 466–475.

[48] J. C. Dainty and R. Shaw, *Image Science*. New York: Academic Press, 1974.

[49] R. F. Wagner and D. G. Brown, "Unified SNR analysis of medical imaging systems," *Physics in Medicine and Biology*, vol. 30, pp. 489–518, June 1985.

[50] H. H. Barrett and W. Swindell, Eds., *Radiological Imaging: The Theory of Image Formation, Detection, and Processing*. New York: Academic Press, 1981, vol. 1.

[51] J. M. Boone and J. A. Seibert, "An accurate method for computer-generating tungsten anode x-ray spectra from 30 to 140 kv," *Medical Physics*, vol. 24, no. 11, pp. 1661–1670, 1997.

[52] D. Zhang, X. Wu, M. Wong, Y. Ni, J. Rong, W. R. Chen, and H. Liu, "Error analysis in the measurement of x-ray photon fluence: an analysis on the uncertainty from energy calibration," V. V. Tuchin, L. V. Wang, and D. D. Duncan, Eds., vol. 7176, no. 1. SPIE, 2009, p. 71760I.

[53] H. Johns and J. Cunningham, *The Physics of Radiology*. Thomas, Springfield, IL,, 1974.

[54] T. R. Fewell and R. E. Shuping, "Photon energy distribution of some typical diagnostic x-ray beams," *Medical Physics*, vol. 4, no. 3, pp. 187–197, 1977.

[55] J. M. Boone, T. R. Fewell, and R. J. Jennings, "Molybdenum, rhodium, and tungsten anode spectral models using interpolating polynomials with application to mammography," *Medical Physics*, vol. 24, no. 12, pp. 1863–1874, 1997.

[56] J. M. Boone, "Spectral modeling and compilation of quantum fluence in radiography and mammography," J. T. D. III and J. M. Boone, Eds., vol. 3336, no. 1. SPIE, 1998, pp. 592–601.

[57] E. Samei and M. J. Flynn, "An experimental comparison of detector performance for computed radiography systems," *Medical Physics*, vol. 29, no. 4, pp. 447–459, 2002.

[58] D. M. Tucker, G. T. Barnes, and D. P. Chakraborty, "Semiempirical model for generating tungsten target x-ray spectra," *Medical Physics*, vol. 18, no. 2, pp. 211–218, 1991.

[59] T. R. Fewell and R. E. Shuping, *Handbook of Mammographic X-ray Spectra*. Rockville, MD: HEW Publication (FDA) 79-8071, 1978.

[60] S. Miyajima and K. Imagawa, "CdZnTe detector in mammographic x-ray spectroscopy," *Physics in Medicine and Biology*, vol. 47, no. 22, pp. 3959–3972, 2002.

[61] S. Miyajima, K. Imagawa, and M. Matsumoto, "Cdznte detector in diagnostic x-ray spectroscopy," *Medical Physics*, vol. 29, no. 7, pp. 1421–1429, 2002.

[62] R. Redus, J. Pantazis, T. Pantazis, A. Huber, and B. Cross, "Characterization of CdTe detectors for quantitative x-ray spectroscopy," *IEEE Transactions on Nuclear Science*, in press.

[63] S. Miyajima, "Thin CdTe detector in diagnostic x-ray spectroscopy," *Medical Physics*, vol. 30, no. 5, pp. 771–777, 2003.

[64] J.T.Bushberg, J.A.Seibert, E. Jr., and J.M.Boone, *The Essential Physics of Medical Imaging*, 2nd ed. Philadephia: Lippincott Williams and Wilkins, 2002, pp. 52–54.

[65] H. Mark and J. Workman, *Statistics in Spectroscopy*, 2nd ed. San Diego: Academic Press, 2003, pp. 271–312.

[66] R. J. Larsen and M. L. Marx, *An Introduction to Mathematical Statistics and Its Applications*, 4th ed. Pearson Prentice Hall, NJ, 1994, pp. 481–492, 646–725.

[67] I. Miller and M. Miller, *John E. Freund's Mathematical Statistics with Applications*. Prentice Hall, 2004, ch. 14, pp. 439–450.

[68] ISO, *Guide to the expression of uncertainty in measurement*, 1st ed. Geneva: International Organization for Standardization (ISO), 1993.

[69] ANSI/ASME, *Test Uncertainty. ANSI/ASME PTC 19.1-1998*. New York: ASME, 1998.

[70] R. Redus, *Efficiency of Amptek XR-100T-CdTe and -CZT Detectors (Application Note ANCZT-1 Rev. 2)*, Amptek Inc., 14 DeAngelo Dr., Bedford MA 01730, December 2002.

[71] I. A. Brezovich and S. Jordan, "A device for precision positioning and alignment of room lasers to diminish their contribution to patient setup errors," *Journal of Applied Clinical Medical Physics*, vol. 8, no. 4, pp. 45–53, 2007.

[72] H. MacMahon, N. Yasillo, and M. Carlin, "Laser alignment system for high-quality portable radiography," *Radiographics*, vol. 12, no. 1, pp. 111–120, 1992.

[73] E. Samei, M. J. Flynn, and D. A. Reimann, "A method for measuring the presampled MTF of digital radiographic systems using an edge test device," *Medical Physics*, vol. 25, no. 1, pp. 102–113, 1998.

[74] R. T. Droege, "A megavoltage MTF measurement technique for metal screen-film detectors," *Medical Physics*, vol. 6, no. 4, pp. 272–279, 1979.

[75] H. Kubota, Y. Ozaki, M. Matsumoto, and H. Kanamori, "Determination of x-ray tube focal spot position," *Medical Physics*, vol. 20, no. 4, pp. 1029–1031, 1993.

[76] K. Nishizawa, H. Maekoshi, Y. Kamiya, Y. Kobayashi, K. Ohara, and S. Sakuma, "Alignment of x-ray tube focal spots for spectral measurement," *Medical Physics*, vol. 9, no. 2, pp. 284–287, 1982.

[77] E. R. Epp and H. Weiss, "Experimental study of the photon energy spectrum of primary diagnostic x-rays," *Physics in Medicine and Biology*, vol. 11, no. 2, pp. 225–238, 1966.

[78] U. Bottigli, B. Golosio, G. L. Masala, P. Oliva, S. Stumbo, P. Delogu, M. E. Fantacci, L. Abbene, F. Fauci, and G. Raso, "Comparison of two portable solid state detectors with an improved collimation and alignment device for mammographic x-ray spectroscopy," *Medical Physics*, vol. 33, no. 9, pp. 3469–3477, 2006.

[79] S. Miyajima, K. Imagawa, and M. Matsumoto, "An alignment method for mammographic X-ray spectroscopy under clinical conditions," *Br J Radiol*, vol. 75, no. 897, pp. 763–766, 2002.

[80] F. B. Meng, A. M. Yan, G. Zhou, X. Z. Wu, and H. Liu, "Development of a dual-detector x-ray imaging system for phase retrieval study," *Nuclear Instruments & Methods in Physics Research Section B-Beam Interactions with Materials and Atoms*, vol. 254, no. 2, pp. 300–306, 2007.

[81] X. Wu and H. Liu, "A dual detector approach for x-ray attenuation and phase imaging," *Journal of X-Ray Science and Technology*, vol. 12, no. 1, pp. 35–42, 2004.

[82] H. Liu, D. Zhang, and X. Wu, "Development of a dual detector phase x-ray imaging system: design considerations," *IEEE Southwest Symposium on Image Analysis and Interpretation, 2008. SSIAI 2008*, pp. 193–196, March 2008.

[83] M. L. Giger and K. Doi, "Investigation of basic imaging properties in digital radiography. i. modulation transfer function," *Medical Physics*, vol. 11, no. 3, pp. 287–295, 1984.

[84] I. A. Cunningham and B. K. Reid, "Signal and noise in modulation transfer function determinations using the slit, wire, and edge techniques," *Medical Physics*, vol. 19, no. 4, pp. 1037–1044, 1992.

[85] J. M. Boone and J. A. Seibert, "An analytical edge spread function model for computer fitting and subsequent calculation of the LSF and MTF," *Medical Physics*, vol. 21, no. 10, pp. 1541–1545, 1994.

[86] H. Illers, E. Buhr, S. Gunther-Kohfahl, and U. Neitzel, "Measurement of the modulation transfer function of digital X-ray detectors with an opaque edge-test device," *Radiation Protection Dosimetry*, vol. 114, no. 1-3, pp. 214–219, 2005.

[87] E. Samei, N. T. Ranger, J. T. Dobbins, and I. Y. Chen, "Intercomparison of methods for image quality characterization. i. modulation transfer function," *Medical Physics*, vol. 33, no. 5, pp. 1454–1465, 2006.

[88] I. A. Cunningham and A. Fenster, "A method for modulation transfer function determination from edge profiles with correction for finite-element differentiation," *Medical Physics*, vol. 14, no. 4, pp. 533–537, 1987.

[89] J. Yorkston, L. E. Antonuk, N. Seraji, W. Huang, J. H. Siewerdsen, and Y. El-Mohri, "Evaluation of the MTF for a-Si:H imaging arrays," R. Shaw, Ed., vol. 2163, no. 1. SPIE, 1994, pp. 141–149.

[90] D. A. Reimann, H. A. Jacobs, and E. Samei, "Use of wiener filtering in the measurement of the two-dimensional modulation transfer function," J. T. D. III and J. M. Boone, Eds., vol. 3977, no. 1. SPIE, 2000, pp. 670–680.

[91] O. Yadid-Pecht, "Geometrical modulation transfer function for different pixel active area shapes," *Optical Engineering*, vol. 39, no. 4, pp. 859–865, 2000.

[92] K. A. Fetterly, N. J. Hangiandreou, B. A. Schueler, and E. R. Ritenour, "Measurement of the presampled two-dimensional modulation transfer function of digital imaging systems," *Medical Physics*, vol. 29, no. 5, pp. 913–921, 2002.

[93] M. Donovan, D. Zhang, and H. Liu, "Step by step analysis toward optimal MTF algorithm using an edge test device," *Journal of X-ray Science and Technology*, vol. 17, no. 1, p. accepted, March 2009.

[94] R. H. Menk, W. Thomlinson, N. Gmur, Z. Zhong, D. Chapman, F. Arfelli, W. R. Dix, W. Graeff, M. Lohmann, G. Illing, L. Schildwachter, B. Reime, W. Kupper, C. Hamm, J. C. Giacomini, H. J. Gordon, E. Rubenstein, J. Dervan, H. J. Besch, and A. H. Walenta, "The concept of spatial frequency depending DQE and its application to a comparison of two detectors used in transvenous coronary angiography," *Nuclear Instruments and Methods in Physics Research Section A: Accelerators, Spectrometers, Detectors and Associated Equipment*, vol. 398, no. 2-3, pp. 351 – 367, 1997.

[95] J. Carnes and W. Kosonocky, "Noise sources in charge-coupled devices," *RCA Review*, pp. 327–343, June 1972.

[96] J. R. Janesick, *Scientific Charge-coupled Devices*, ser. SPIE Press Monograph. Bellingham,WA: SPIE Press, 2001, vol. PM83, pp. 605–719.

[97] A. Snigirev, I. Snigireva, V. Kohn, S. Kuznetsov, and I. Schelokov, "On the possibilities of x-ray phase contrast microimaging by coherent high-energy synchrotron radiation," *Review of Scientific Instruments*, vol. 66, no. 12, pp. 5486–5492, 1995.

[98] F. Arfelli, V. Bonvicini, A. Bravin, G. Cantatore, E. Castelli, L. Dalla Palma, M. Di Michiel, M. Fabrizioli, R. Longo, R. H. Menk, A. Olivo, S. Pani, D. Pontoni, P. Poropat, M. Prest, A. Rashevsky, M. Ratti, L. Rigon, G. Tromba, A. Vacchi, E. Vallazza, and F. Zanconati, "Mammography with synchrotron radiation: Phase-detection techniques," *Radiology*, vol. 215, no. 1, pp. 286–293, 2000.

[99] S. W. Wilkins, T. E. Gureyev, D. Gao, A. Pogany, and A. W. Stevenson, "Phase-contrast imaging using polychromatic hard x-rays," *Nature*, vol. 384, no. 6607, pp. 335–338, 1996.

[100] A. Pogany, D. Gao, and S. W. Wilkins, "Contrast and resolution in imaging with a microfocus x-ray source," *Review of Scientific Instruments*, vol. 68, no. 7, pp. 2774–2782, 1997.

[101] Y. Y. Zhou, H. K. Pew, J. Rong, W. R. Chen, L. Fajardo, X. Wu, and H. Liu, "Phantom imaging with a prototype phase contrast radiography system," in *Saratov Fall Meeting 2005: Optical Technologies in Biophysics and Medicine VII*, V. V. Tuchin, Ed., vol. 6163, no. 1. SPIE, 2006, p. 61630E.

[102] C. J. Kotre and I. P. Birch, "Phase contrast enhancement of x-ray mammography: a design study," *Physics in Medicine and Biology*, vol. 44, no. 11, pp. 2853–2866, 1999.

[103] E. F. Donnelly, R. R. Price, and D. R. Pickens, "Quantification of the effect of system and object parameters on edge enhancement in phase-contrast radiography," *Medical Physics*, vol. 30, no. 11, pp. 2888–2896, 2003.

[104] Y. I. Nesterets, S. W. Wilkins, T. E. Gureyev, A. Pogany, and A. W. Stevenson, "On the optimization of experimental parameters for x-ray in-line phase-contrast imaging," *Review of Scientific Instruments*, vol. 76, no. 9, p. 093706, 2005.

[105] X. Wu and H. Liu, "Clinical implementation of x-ray phase-contrast imaging: Theoretical foundations and design considerations," *Medical Physics*, vol. 30, no. 8, pp. 2169–2179, 2003.

[106] A. Olivo and R. Speller, "Modelling of a novel x-ray phase contrast imaging technique based on coded apertures," *Physics in Medicine and Biology*, vol. 52, no. 22, pp. 6555–6573, 2007.

[107] X. Wu and H. Liu, "A general theoretical formalism for x-ray phase contrast imaging," *Journal of X-Ray Science and Technology*, vol. 11, no. 1, pp. 33–42, 2003.

[108] E. F. Donnelly, R. R. Price, and D. R. Pickens, "Dual focal-spot imaging for phase extraction in phase-contrast radiography," *Medical Physics*, vol. 30, no. 9, pp. 2292–2296, 2003.

[109] X. Wu and H. Liu, "Phase-space formulation for phase-contrast x-ray imaging," *Appl. Opt.*, vol. 44, no. 28, pp. 5847–5854, 2005.